# Functional tip-sample interactions in STM

Gobeil, J.

**DOI**
10.4233/uuid:1ff19056-6af0-4b96-b278-84907c20ec77

**Publication date**
2023

**Document Version**
Final published version

**Citation (APA)**
Gobeil, J. (2023). *Functional tip-sample interactions in STM*. [Dissertation (TU Delft), Delft University of Technology]. https://doi.org/10.4233/uuid:1ff19056-6af0-4b96-b278-84907c20ec77

# FUNCTIONAL TIP-SAMPLE INTERACTION IN STM

# FUNCTIONAL TIP-SAMPLE INTERACTION IN STM

## Dissertation

for the purpose of obtaining the degree of doctor
at Delft University of Technology,
by the authority of the Rector Magnificus Prof. dr. ir. T.H.J.J. van der Hagen
chair of the Board for Doctorates
to be defended publicly on
Monday 11 December 2023 at 17:30 o'clock

by


**Jeremie GOBEIL**

Master of Science in Physics, University du Québec à Trois-Rivières, Trois-Rivières, Canada,

born in Chicoutimi, Canada.

This dissertation has been approved by the promotors.

Prof. dr. A.F. Otte
Prof. dr. ir. H.S.J. van der Zant

Composition of the doctoral committee:

| | |
|---|---|
| Rector Magnificus | chairperson |
| Prof. dr. A.F. Otte | Delft University of Technology, promotor |
| Prof. dr. ir. H.S.J. van der Zant | Delft University of Technology, promotor |

*Independent members:*

| | |
|---|---|
| Prof. dr. S. Gröblacher | Delft University of Technology |
| Dr. A. R. Akhmerov | Delft University of Technology |
| Prof. dr. P.M. Koenraad | Eindhoven University of Technology, Netherlands |
| Prof. dr. M. Ternes | RWTH Aachen University, Germany |
| Prof. dr. Y.V. Nazarov | Delft University of Technology, reserve member |


*Keywords:* Scanning tunnelling microscopy, Tip functionalisation , Image potential states, Field emission resonance, Quantum magnetism, Frustrated magnetism

*Printed by:* Gildeprint

*Front & Back:* Abstract illustration of a tip-sample interaction



Casimir PhD Series, Delft-Leiden 2023-40

ISBN 978-94-6366-790-6

An electronic version of this dissertation is available at
http://repository.tudelft.nl/.

# CONTENTS

# SUMMARY

A scanning tunnelling microscope (STM) is a powerful tool that allows "seeing" or "touching" individual atoms of a surface or adsorbed on a surface. This feat is made possible by the precise positioning of a sharp conducting probe, a.k.a. the tip, close enough to a conducting sample that the electron can jump between them. This is made possible by a phenomenon called quantum tunnelling and presented in more detail in Chapter 2.

Often, in STM experiments, the tip is hopefully external to the observation, like microscopes and telescopes have no impact on the object emitting the light they receive. However, for the STM, this approximation is only sometimes valid, and the effect of the nearby tip often needs to be considered in the observation modelling. This thesis aimed to not only consider the effect of the tip but also to make it an active part of the experiments. This is accomplished in multiple ways: as an atom manipulator (chapters 5 and 6), as a local magnetic field source (chapter 5), or as a confining potential (chapter 6).

After a brief introduction in Chapter 1, the thesis presents in Chapter 2 the background theory and experimental considerations needed for the following chapters. The chapter begins by explaining the quantum tunnelling phenomenon and some experimental techniques used in the thesis, like differential conductance and spin-polarised electron tunnelling. This chapter also introduces the two STMs present in our lab and used for the thesis. The chapter concludes by presenting a historical and theoretical overview of the image potential state, which is central to the experiment in Chapter 6.

Following this mise-en-bouche, Chapter 3 develops two models used for numerical calculation and interpretation of the experimental observations. The first model introduces the Spin Hamiltonian and the rate equation. These two allow us to reproduce the measurements on a single or multiple interacting magnetic adatoms with good fidelity. The second model merges the multiple potentials produced by the tip and sample. The global potential allows us to correctly predict the energy of the image potential states observed in Chapter 6.

Chapter 4 presents the novel $Cu_2N$ over $Cu_3Au$ substrate used in the following chapter. This substrate combines the well-known properties of CuN over Cu without being constrained by the lattice mismatch limiting the island size. This allows larger structures to be assembled on the substrate without compromising the ease of atom manipulation. This substrate forms the base on which are assembled the instrinically frustrated atomic spin loops presented in Chapter 5. Those loops are studied notably by using the tip on which a magnetic cluster is attached to create a local magnetic field. This local field allows us to locally bias the global and probe the behaviour of the loop under new conditions, revealing properties that could not be observed before.

In the last chapter, Chapter 6, the STM is used to probe higher energy resonance, the field-emission resonance (FER). The FERs are the manifestation of local states existing above certain surfaces called image potential states (IPS). In our STM setup, the IPSs are not only constrained by the potential created by the tip and its position but also by square areas of bare copper surrounded by insulating chloride. These squares create a potential that laterally confines the electrons that exhibit particle-in-a-box-like behaviours. Changing the distance between the sample and the tip changes the shape of the tip potential and gives us a new adjustable parameter, helping the understanding of the observations.

# SAMENVATTING

Een scanning tunnelling microscope (STM) is een krachtig instrument waarmee individuele atomen aan een oppervlak of geadsorbeerd op een oppervlak kunnen worden "gezienöf äangeraakt". Deze prestatie wordt mogelijk gemaakt door een scherpe geleidende naald, ook wel de tip genoemd, zo dicht bij een geleidend substraat te plaatsen dat een elektron van de een naar de ander kan springen. Dit wordt mogelijk gemaakt door een fenomeen dat quantum tunneling wordt genoemd en in meer detail wordt beschreven in hoofdstuk 2.

Idealiter is de naald bij STM-experimenten extern aan de waarneming, zoals microscopen en telescopen geen invloed hebben op het object dat het licht uitzendt dat ze ontvangen. Voor de STM is deze benadering echter slechts soms geldig en moet het effect van de nabije tip vaak worden meegenomen in het modelleren van de observatie. Deze dissertatie is erop gericht om niet alleen rekening te houden met het effect van de tip, maar om het ook een actief onderdeel van de experimenten te maken. Dit wordt op verschillende manieren bereikt: als een atoommanipulator (hoofdstuk 5 en 6), als een lokale magnetische veldbron (hoofdstuk 5), of als een opsluitende potentiaal (hoofdstuk 6).

Na een korte introductie in hoofdstuk 1, presenteert het proefschrift in hoofdstuk 2 de achtergrondtheorie en experimentele overwegingen die nodig zijn voor de volgende hoofdstukken. Het hoofdstuk begint met het uitleggen van het kwantumtunnelfenomeen en enkele experimentele technieken die in het proefschrift gebruikt worden, zoals differentiële geleiding en spin-gepolariseerde elektronentunneling. Dit hoofdstuk introduceert ook de twee STM's die in ons lab aanwezig zijn en gebruikt worden voor dit proefschrift. Het hoofdstuk sluit af met een historisch en theoretisch overzicht van de beeldpotentiaaltoestand, die centraal staat in het experiment in hoofdstuk 6.

Na deze mise-en-bouche ontwikkelt hoofdstuk 3 twee modellen die gebruikt worden voor de numerieke berekening en interpretatie van de experimentele waarnemingen. Het eerste model introduceert de spin Hamiltoniaan en de snelheidsvergelijking. Deze twee stellen ons in staat om de metingen aan een enkel of meerdere wisselwerkende magnetische atomen met goede getrouwheid te reproduceren. Het tweede model voegt de meervoudige potentialen samen die door de tip en het substraat worden geproduceerd. De globale potentiaal stelt ons in staat om de energie van de beeldpotentiaaltoestanden waargenomen in hoofdstuk 6 correct te voorspellen.

Hoofdstuk 4 presenteert het nieuwe $Cu_2N$ op $Cu_3Au$ substraat dat in het volgende hoofdstuk wordt gebruikt. Dit substraat combineert de bekende eigenschappen van Cu2N over Cu zonder beperkt te worden door de roosterafwijking die de eilandgrootte beperkt. Hierdoor kunnen grotere structuren worden geassembleerd op het substraat

zonder afbreuk te doen aan het gemak van atoommanipulatie. Dit substraat vormt de basis waarop de instrinsiek magnetisch gefrustreerde atomaire spinlussen uit hoofdstuk 5 worden geassembleerd. Deze lussen worden met name bestudeerd door de tip waarop een magnetisch cluster is bevestigd te gebruiken om een lokaal magnetisch veld te creëren. Dit lokale veld stelt ons in staat om de globaal lokaal te beïnvloeden en het gedrag van de lus onder nieuwe omstandigheden te onderzoeken, waardoor eigenschappen aan het licht komen die voorheen niet waargenomen konden worden.

In het laatste hoofdstuk, hoofdstuk 6, wordt de STM gebruikt om hogere energie resonanties te onderzoeken, de field-emission resonance (FER). De FER's zijn de manifestatie van lokale toestanden die boven bepaalde oppervlakken bestaan, image potential states (IPS) genoemd. In onze STM-opstelling worden de IPS niet alleen beperkt door de potentiaal die gecreëerd wordt door de tip en zijn positie, maar ook door vierkante gebieden van zuiver koper omgeven door isolerend chloride. Deze vierkanten creëren een potentiaal die zijdelings de elektronen insluit die deeltje-in-een-doos gedrag vertonen. Het veranderen van de afstand tussen het substraat en de tip verandert de vorm van de potentiaal van de tip en geeft ons een nieuwe instelbare parameter die helpt bij het begrijpen van de waarnemingen.

# 1

# INTRODUCTION

*In this thesis, using scanning tunnelling microscopes we manipulate atoms deposed on surfaces to create and observe quantum states – frustrated magnetic states existing in specifically engineered atoms loop; and electronic states trapped vertically by image potential states and vertically by square holes in an insulating layer of chlorine. In addition, the growth of CuN islands over $Cu_3Au$ surface is presented. This constitutes a novel substrate allowing large insulating islands suitable for atomic manipulation and assembling large magnetic structures, like the magnetically frustrated spin loop. We take special attention to the role of the STM probe tip in these experimental contexts. The tip is employed as a tool for manipulating surface atoms; an adjustable component enabling modification of the local magnetic field and distribution of spin states; and a confining potential altering the conditions for electron trapping above the surface.*

1

Observing, understanding, and changing the matter at increasingly smaller scales has been a long-standing pursuit in science[1, 2]. Whether for creating electronic components on a silicon chip[3], building quantum computers[4] or developing more efficient solar panels[5, 6], understanding the behaviour of those systems at their smallest composing block, the molecules and atoms, is fundamental to pushing them further.

However, most instruments and experiments can only address large ensembles of atoms and molecules, and observed behaviour will be an average over many atoms. Observing individual atoms and molecules is challenging, but something that is now done routinely in many using scanning tunnelling microscope (STM)[7, 8]. STM is a powerful tool for observing and manipulating matter at the atomic scale[9, 10]. The possibility to observe, experiment and manipulate individual atoms at the atomic scale opens unprecedented opportunities for fundamental research and potential technological applications.

The fundamental concept distinguishing the STM from other scanning probe microscopes is the quantum tunnelling current created by the proximity of its conducting probe to the sample surface[11]. The presence of this probe, or tip, is often neglected in the observation analysis and experimental design. In this thesis, the tip will play an active role in multiple aspects of the experiments. Depending on the context, it will be a tool used to move the surface's atoms via vertical and horizontal manipulations; an adjustable component of the experimental, allowing the modification of the local magnetic field and changing the distribution of the spin states; or a confining potential, changing the condition in which electrons are trapped electrons above a surface.

## THESIS OUTLINE

The next chapter introduces the basic theory of quantum tunnelling, its application to the STM, and the basic experimental techniques used in the thesis. Basic concepts common to many STM experiments are discussed, like topographic maps of a surface, differential conductance (dI/dV), lock-in measurements, inelastic electron tunnelling spectroscopy, spin-polarised electron tunnelling, and the experimental techniques of atom manipulation with an STM. This introduction of the fundamentals of STM is followed by a brief description of the two STMs available in the labs that were used to perform the experiments, a JT-STM by SPECS$^{TM}$ and a USM 1300S by UNISOKU$^{TM}$. This chapter concludes with a historical and theoretical presentation of the image potential states (IPS) and their manifestation with an STM, the field emission resonance (FER). The IPS exist above certain surfaces and can trap electrons in short-lived states observable with an STM in a high-voltage regime — above the work function of the surface. In this regime, the working principle differs from the usual STM usage as the current is generated by field emission instead of quantum tunnelling.

This discussion on STM is followed in Chapter 3 by an exploration of the numerical methods and models used to simulate the frustrated spin loop and the image potential states. The Spin Hamiltonian model is introduced, including the Zeeman effect, magnetic anisotropy, and the Heisenberg coupling. The Spin Hamiltonian will be the reference model for evaluating the spin states. The utilisation of the rate equation and Pauli

Master Equation formalism is used to calculate the transitions between the quantum states and how they manifest in the resulting quantum dynamics in Chapter 5. Finally, this chapter presents an approach to evaluate the wavefunction existing in arbitrary potentials by solving the Schrödinger equation using a variational principle. This will be applied to the calculation of image potential states, allowing the modelling of the complex potential created by the chlorine vacancy patches and the tip in Chapter 6.

In Chapter 4, atom manipulation, quantum states, and magnetism are left temporarily behind to present the experimental realisation of large insulating nitride islands grown on $Cu_3Au$. By using a $Cu_3Au$ substrate, the nitride islands can grow larger, unhindered by the lattice mismatch compared with the commonly used Cu substrate. We notably explore the effect of the temperate on the island's growth process. The resulting surface was used as the base canvas for the experimental realisation of a magnetically frustrated spin-loop presented in Chapter 5.

Chapter 5 discusses the realisation and observation of state switching in engineered intrinsically frustrated spin loops assembled by vertical manipulation on $Cu_2N$ islands on $Cu_3N$. The justification for the design of the magnetic frustration loop is explained, including a theoretical analysis of the resulting structure and quantum states. The assembling process is shown, and the experimental observation of the spin states is presented. These observations are obtained using a spin-polarised tip and include spontaneous state switchings. It shows how the presence of the tip can influence the distribution and frequency of the switches and how the tip can be used to force changes in the ground state of the loop. The chapter is concluded by a numerical analysis trying to explain the experimental observation, notably the unsymmetric behaviour of the loop.

The last chapter, chapter 6, presents the realisation and analysis of particle-in-a-box electronic states created by image potential states locally confined by chlorine nitride. Chlorine atoms evaporated on a Cu(111) surface create a chlorine monolayer. If undersaturated, some holes or chlorine vacancies will exist. Chlorine vacancies were moved using horizontal manipulations and bunched together to create patches of copper surrounded by insulating chlorine atoms. The resulting configuration forms a potential confining the field emission resonances laterally and creating paticle-in-a-box electron states. The tip acts on the vertical confinement and modifies the energy of the resonances. Numerical calculations bring a deeper understanding of the conditions creating the observed states.

## REFERENCES

[1] R. P. Feynman, *There's Plenty of Room at the Bottom,* Engineering and Science **23**, 22 (1960).

[2] M. C. Roco and W. Bainbridge, *Societal implications of nanoscience and nanotechnology: Maximizinghuman benefit,* J Nanopart Res **7**, 1 (2005).

[3] S. M. Sze and M. K. Lee, *Semiconductor Devices, Physics and Technology*, 3rd ed. (Wiley, Hoboken, N.J, 2012).

[4] M. A. Nielsen and I. L. Chuang, *Quantum Computation and Quantum Information*, 10th ed. (Cambridge University Press, Cambridge ; New York, 2010).

[5] P. V. Kamat, *Quantum Dot Solar Cells. Semiconductor Nanocrystals as Light Harvesters*, J. Phys. Chem. C **112**, 18737 (2008).

[6] A. J. Nozik, *Nanoscience and Nanostructures for Photovoltaics and Solar Fuels*, Nano Lett. **10**, 2735 (2010).

[7] G. Binnig and H. Rohrer, *Scanning tunneling microscopy*, Surface Science **126**, 236 (1983).

[8] J. A. Stroscio and D. M. Eigler, *Atomic and Molecular Manipulation with the Scanning Tunneling Microscope*, Science **254**, 1319 (1991).

[9] J. Tersoff and D. R. Hamann, *Theory and Application for the Scanning Tunneling Microscope*, Phys. Rev. Lett. **50**, 1998 (1983).

[10] D. M. Eigler and E. K. Schweizer, *Positioning single atoms with a scanning tunnelling microscope*, Nature **344**, 524 (1990).

[11] J. Tersoff and D. R. Hamann, *Theory of the scanning tunneling microscope*, Phys. Rev. B **31**, 805 (1985).

# 2

# STM THEORY AND EXPERIMENTAL METHODOLOGY

*In this chapter, we briefly describe the physics behind a Scanning Tunnelling Microscope (STM) and the basic experimental methods used in STM experiments and relevant for the following chapters. The experimental methods presented include topographic scans, lock-in measurements, inelastic electron tunnelling spectroscopy and spin-polarised electron tunnelling, and the description of the two scanning tunnelling microscopes (STM) in our labs. A presentation of the image potential state and field emission resonance concludes the chapter.*

## 2.1. SCANNING TUNNELLING MICROSCOPY

Gerd Binnig and Heinrich Rohrer developed the Scanning Tunnelling Microscope (STM) in 1981 at the IBM Zürich[1, 2] research laboratories. They received the Nobel Prize in Physics for this invention in 1986. The apparatus measures small currents created by the quantum tunnelling of electrons between a sharp conducting electrode, often called 'tip', and a sample. For the current to be measurable, the distance between the tip and the sample needs to be small, in the order of a nanometer, and a difference in electric potential must exist between the tip and the sample. Piezoelectric actuators control the tip's precise positioning over the surface and are usually regulated via a feedback loop linking the current and the separation of the tip and sample. The exponential dependence of the current on the distance to the sample and the precise positioning of the tip give enough resolution that, in certain conditions, even a single atom can be distinguished.

Essentially, an STM "only" measures the electric current flowing between a tip and a sample. What makes an STM interesting is how this current is generated and controlled. Unlike usual electric circuits, the circuit is never fully closed as the tip and sample are not

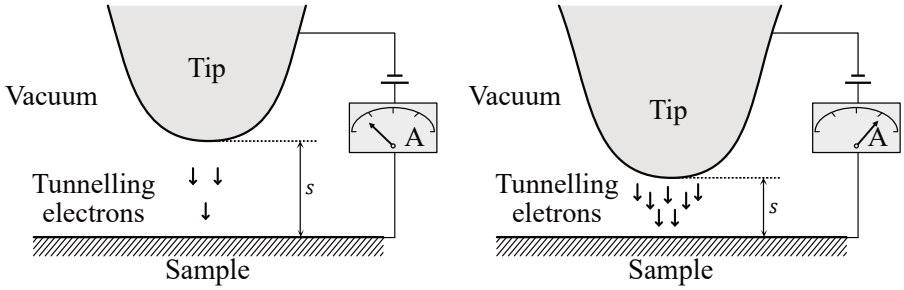


**Figure 2.1: Simple STM schematic**. An STM function on the principle of quantum tunnelling of electrons. When the distance *s* is small enough, in the order of a nanometer, a small current will be generated when a potential difference is applied between the tip and the sample. This intensity of the current will change with the distance between the tip and the sample.

in contact during the measurements; a gap always exists. The circuit gap often consists of vacuum, but could also be filled by gases or liquids[3–6]. If we follow the classical law of electromagnetism, as stated by Maxwell, when a constant potential is applied, no current should flow through this open circuit. However, quantum mechanics allows the tunnelling of electrons between the tip and the sample. Quantum tunnelling will be discussed in more detail shortly. When a constant difference of electric potential exists between the tip and the sample, and the distance between the two is in the order of a nanometer, a weak but measurable net current will flow through the gap. The intensity of this current depends exponentially on the size of the gap and allows the fine control and positioning of the tip via piezoelectric actuators. A schematic illustration of the working principle of an STM is shown in Figure 2.1.

The STM opens the door to many experiments probing physics and chemistry at a previously inaccessible scale. In the years following its invention, and up to the present day, physicists design new experiments and explore new physics by observing different samples[7–10]; manipulating the atoms of various samples[11–14]; using the precise positioning [15–19]; adjusting the nature of the tip [20–25]; the modulation of the electric potential[17, 26–31]; or of the magnetic field [32–36].

The following section will introduce the basic theory, terminology and experimental techniques used in this thesis. We will briefly introduce the physics behind the quantum tunnelling phenomenon and the basic experimental techniques used in the thesis, like topographic scanning, inelastic electron tunnelling spectroscopy, differential conductance, spin-polarised STM and atom manipulation.

### 2.1.1. QUANTUM TUNNELLING

At its core, an STM harnesses the quantum nature of the small-scale world by utilising the quantum tunnelling effect to create a current. Quantum tunnelling arises from the laws of quantum mechanics and states that a particle can cross through a potential wall, albeit with a small probability, even if the energy of that particle is not high enough to

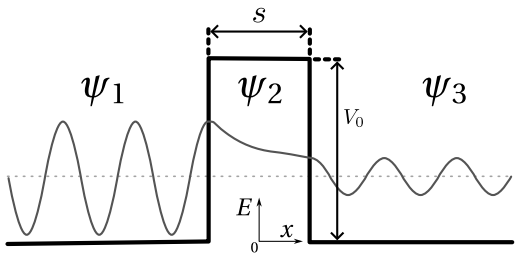


**Figure 2.2: Schema of a flux of particles through a square potential**. A flux of particles from the left ($\psi_1$) encounters a potential wall ($\psi_2$) of length $s$. The energy of the particles is not sufficient to overcome the wall. The Schrödinger equation allows a solution where the is a non-zero probability that the particle can be observed at the region on the right ($\psi_3$).

pass over that wall classically. It will be like placing a ball somewhere inside a bowl and later finding it outside without external intervention. Classically, wherever you place the ball, it would not have enough energy to go higher than its initial height, and so above the side of the bowl. However, in the quantum world, it is possible. In fact, as long as the side of the bowl is not infinite in height, there is a finite probability that this will happen at any moment.

To understand quantum tunnelling, we can start by considering the uncertainty principle applied to the complementary variables that are time and energy[37]. This leads to the relation

$$\Delta t \Delta E \geq \frac{\hbar}{2}. \tag{2.1}$$

This equation states that considering a short timescale, the particle's energy becomes less certain and can reach an energy high enough to overcome the barrier, albeit for a short time. The higher the energy, the shorter the time, and the less probable to observe the particle beyond the barrier. This equation is similarly interpreted for the appearance and disappearance on a short timescale of virtual particles in the quantum vacuum. Although, this interpretation of Equation 2.1 is not universally accepted[38].

A more usual approach to interpreting quantum tunnelling is to use the wave component of the wave-particle duality of the matter. This approach requires that we define a potential, express the situation using the Schrödinger equation and solve the resulting problem. This is a standard exercise part of most undergraduate quantum physics course curricula. An analytic solution exists for some simple situations. The reader can refer to undergraduate physics textbooks for more details[39, 40].

A simple model to describe quantum tunnelling, or an STM junction, is a one-dimensional system where particles travel from the left toward a finite potential wall of height $V_0$ and width $s$. This system is illustrated in Figure 2.2. The solution to the Schrödinger equation

for this system for the three regions will be (without the time-dependent part):

$$\psi(x) = \begin{cases} \psi_1(x) = A_1 e^{ikx} + B_1 e^{-ikx} & \text{if } x < -s/2, \\ \psi_2(x) = A_2 e^{\kappa x} + B_2 e^{-\kappa x} & \text{if } -s/2 < x < s/2, \\ \psi_3(x) = A_3 e^{ikx} + B_3 e^{-ikx} & \text{if } x > s/2. \end{cases} \tag{2.2}$$

with

$$k = \sqrt{\frac{2mE}{\hbar^2}}, \qquad \kappa = \sqrt{\frac{2m(V_0 - E)}{\hbar^2}}. \tag{2.3}$$

The $A_i$ factors are associated with particles travelling from left to right (increasing $x$) and the $B_i$ from right to left (decreasing $x$). With that information, we can conclude that $B_3 = 0$ as no particles are coming from the right. We can express the fraction of transmitted particles as $T = \left|\frac{A_3}{A_1}\right|^2$.

This set of equations can be solved for the $A_i$ and $B_i$ by imposing the continuity of $\psi(x)$ and $\psi'(x)$ at $x = \pm s/2$. This allows us to write the faction of transmitted flux as

$$T = \left|\frac{A_3}{A_1}\right|^2 = \frac{16k^2\kappa^2 e^{2s\kappa}}{\left(e^{2s\kappa} - 1\right)^2\left(k^2 - \kappa^2\right)^2 + 4\left(k\kappa\left(e^{2s\kappa} + 1\right)\right)^2}. \tag{2.4}$$

We can simplify Equation 2.4 by considering the case where $s$ or $V_0$ are large enough so that $e^{2s\kappa} \gg 1$. In that case, we can write $T$ as

$$T \approx 16\left(\frac{k\kappa}{k^2 + \kappa^2}\right)^2 e^{-2s\kappa} = 16\left(\frac{E}{V_0} - \frac{E^2}{V_0^2}\right) e^{-2s\sqrt{2m(V_0 - E)/\hbar^2}} \tag{2.5}$$

We can see from Equation 2.5 that the flux of particles on the right side of the potential wall goes to zero only when $V_0 \to \infty$ or $s \to \infty$, and that in all real scenarios, the probability is finite. This is a remarkable observation concerning our physical world: there is always a finite probability that some particles will go through a barrier. However, we can also observe that this finite value grows exponentially small as function of barrier width and can easily reach negligible values.

For reference, a flux of $E = 1$ eV electrons travelling toward a potential of $V_0 = 1.1$ eV and length $s = 1$ nm will have a probability to cross it of $T \approx 0.052$. If the gap length is increased to $s = 10$ nm, this value drops to $T \approx 1.12 \cdot 10^{-14}$. Those conditions are similar to what can be used in an STM experiment. We can see that the current flowing through an STM junction decreases rapidly and, as a consequence, will only be detectable when the tip is sufficiently close to the sample. The current will drop exponentially fast as the tip moves away from the surface. The distance where a current can be measured is somewhere between the length of a chemical bond ($\sim 100 - 200$ pm) and a few nm. Achieving such precise positioning requires advanced mechanical isolation and actuators.

To observe a net current in an STM, in addition to letting only a small gap between tip and sample, allowing the quantum tunnelling of electrons, a difference of electric

potential must exist between the two electrodes. If not, the current produced by the electrons tunnelling in both directions will cancel, and no net current will be measured. The electric potential between the tip and the sample is usually called the *bias voltage* of simply *bias*.



It is to be noted that even if a circuit is open, electric current can exist when the electric potential is changing. This is, in fact, a common situation in our daily life as most electric sources are alternating potential, and any transformers or capacitors are effectively open circuits. The tip and sample of an STM can be seen as forming a capacitor. This can be used to evaluate the tip-sample distance when the distance doesn't allow tunnelling current[41]. This is also something to consider during the experiments, especially when using techniques such as lock-in measurement, which is introduced in subsection 2.1.3.

### 2.1.2. TOPOGRAPHY

One of the fundamental capabilities of an STM is its ability to generate topographic scans of surfaces with a precision that allows researchers to "see" the surface at the atomic level. The scans are constructed by systematically moving the STM tip across the surface along parallel lines, recording the variations in the current (or tip's height for constant current mode), and compiling these lines to create a two-dimensional surface map.

Topographic scans are typically created using the constant-current mode tip's height and, unless in specific experiments, the default mode in which an STM operate. This approach helps avoid potential damage to the surface or tip (by "crashing" the tip into the surface). It simultaneously ensures that the tip remains within the tunnelling range while scanning or moving across surfaces. To keep the tip within tunnelling ranges, a feedback loop controlled by a PID (or a simpler PI) is active and keeps the current constant by adjusting the height of the tip. The value at which the current is kept is often called the current setpoint. A safe but tunnelling distance between the tip and the surface is ensured by using an appropriate current setpoint and by moving the tip over the surface slowly enough so that the controller has enough time to adjust the tip height.

It is important to note that the resulting topographic map does not necessarily correspond to a map of the height variation of the surface. The map is a constant current surface over the sample. The map will mostly correspond to the height of the sample if it is formed of identical molecules. Even then, a single missing atom may create a hole that may not be properly mapped because of localised electronic states or the finite precision of the mapping. Moreover, the surfaces studied often include different molecules and contaminants with different conductance, changing the distance at which a specific current is observed. This is particularly apparent when insulating islands are grown on a surface, for example, $Cu_3Au$ over Cu that is discussed in chapter 4. The insulating nature of the $Cu_3Au$ islands requires that the tip is brought closer even though the islands are physically higher. The physically higher islands will appear lower than the surrounding Cu on the topographic scan.

### 2.1.3. LOCK-IN MEASUREMENT

An essential technique used with STM is lock-in measurements. Even if this technique is not specific to STM but rather a general experimental technique used in multiple contexts, its ubiquity in STM experiments is worth briefly introducing. The technique is notably used for inelastic electron tunnelling spectroscopy (subsection 2.1.5) experiment and for the study of field emission resonance (subsection 2.3.3).

In some situations, a low signal-to-noise ratio greatly hinders the capacity to measure specific values in an experiment. It may be possible to average out the noise in some contexts, but that could be impractical or impossible. Suppose it is feasible to modulate the phenomena at a known frequency. In that case, measuring not the direct value but the derivative of this value related to the stimulation with a greatly enhanced precision is possible. The lock-in amplifier (the instrument used to do a lock-in measurement) can be seen as a way to filter out all the frequencies except for the frequency that modulates the phenomenon of interest. The ratio between the stimulation amplitude and the resulting amplitude constitutes the measurement.

To understand how the lock-in amplifier works, we can begin by supposing an observable $y(x)$, where $x$ is an adjustable parameter $x$, with a noisy background $h(t)$. The noisy signal can be written as

$$s = y(x_0) + h(t) \tag{2.6}$$

We modulate the adjustable parameter like $x_0 \to x_0 + \Delta x \cos(\omega t)$ so that

$$s = y(x_0 + \Delta x \cos(\omega t)) + h(t) \tag{2.7}$$

If the amplitude of the modulation is small enough, a good approximation of $s$ can be obtained by using a first-order Taylor expansion for $y(x)$. With that approximation, the measured signal takes the form

$$s = y(x_0) + \Delta x' \frac{\mathrm{d}y}{\mathrm{d}x} \cos\big(\omega t + \phi\big) + h(t) \tag{2.8}$$

where $\phi$ account for a delay, and $\Delta x'$ is an attenuated $\Delta x$ caused by the transmission of the signal or the experiment.

The signal is demodulated by mixing it with a signal of the same frequency than the modulation so that

$$s' = y(x_0)\cos(\omega t) + \Delta x \frac{\mathrm{d}y}{\mathrm{d}x} \cos\big(\omega t + \phi\big)\cos(\omega t) + h(t)\cos(\omega t) \tag{2.9}$$

$$= \big[y(x_0) + h(t)\big]\cos(\omega t) + \Delta x \frac{\mathrm{d}y}{\mathrm{d}x} \frac{1}{2}\big[\cos\big(\phi\big) + \cos\big(2\omega t + \phi\big)\big] \tag{2.10}$$

This equation contains a constant value proportional to the derivative of $y$ related to $x$ that can be isolated by using a combination of low-pass filter and time averaging.

Even if the lock-in measurement allows evaluating specific values with a better signal-to-noise ratio than a direct measurement, the measurement is not absolute and needs to

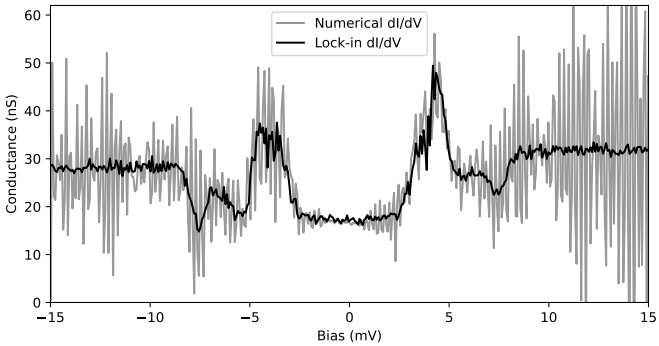


**Figure 2.3: Example of lock-in measurement**. In grey is the numerical differentiation of the current to obtain the conductance. In black is the data measured by the lock-in amplifier. The data of the two curves were obtained at the same time. The numerical data are an absolute (noisy) conductance measurement used to scale the lock-in amplifier measurement to the correct values. The measurement is a spin-polarised bias spectroscopy measurement of an atom of the structure built in chapter 5 (the data shown is only as an example and not presented in the chapter).

be scaled to convert to the correct unit. This scaling depends on multiple factors, notably the modulation amplitude, lock-in sensitivity, and loss during signal propagation. With an STM, this scaling factor can be further complicated by the trans-impedance amplifier, data acquisition, and STM systems. A more straightforward approach is to use a numerical differentiation to obtain a noisy but absolute value measured simultaneously then the lock-in measurement. The conversion factor is evaluated by comparing the lock-in and direct measurements. This is illustrated in Figure 2.3.

### 2.1.4. DIFFERENTIAL CONDUCTANCE

A measurement of great interest that can be accomplished with an STM is the differential conductance ($\mathrm{d}I/\mathrm{d}V$), *i.e.* the change in current under a change in bias voltage. This measurement gives us information on the energy states of the system below the tip. When applied at low bias voltages ($< 100 - 200$ mV), specifically on certain atomic or molecular systems as the ones described in this thesis, $\mathrm{d}I/\mathrm{d}V$ measurements can be used to perform inelastic electron tunnelling spectroscopy (IETS), which will be discussed in more detail in subsection 2.1.5. The usual approach for measuring an IETS curve is to position the tip over the region of interest and remove the feedback loop so the tip stays at a constant distance from the sample. The bias voltage is modulated so that the lock-in measurement of the current results in a measurement of the current variation versus a variation of the bias voltage around this bias voltage ($\mathrm{d}I/\mathrm{d}V$). The measurement is repeated at multiple bias voltages without changing the tip position or height to obtain the IETS curve. The Figure 2.3 is an example of such a measurement.

At higher voltage ($> 1 - 2$ V), $\mathrm{d}I/\mathrm{d}V$ can be used to observe, on particular surfaces, image potential states (IPS), which will be discussed in more detail in subsection 2.3.3.

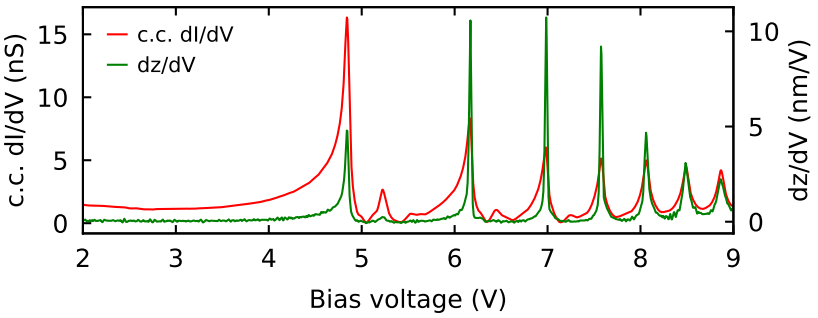


**Figure 2.4: Comparison between $\mathrm{d}I/\mathrm{d}V$ and $\mathrm{d}z/\mathrm{d}V$.** The red curve corresponds to a lock-in measurement of the c.c. $\mathrm{d}I/\mathrm{d}V$ curve taken over a square patch of chlorine vacancies (see subsection 2.3.3. Each peak corresponds to a field emission resonance. The green curve is the numerical differentiation of the height variation relative to the bias variation. The height variation was measured simultaneously with the lock-in measurement. The plot shows some overlap in the feature, but the two curves are quantitatively and qualitatively different.

However, in contrast to IETS, keeping a constant tip-sample distance during the experiment is impractical. The broad voltage bias window needed to observe IPS creates a considerable variation in the current that can saturate the lock-in amplifier or make the signal too weak for an accurate measurement. Consequently, when measuring, the current is maintained constant by keeping the feedback loop active. So the change in current will be compensated by adjusting the tip-sample distance. This measurement will be called 'constant current differential conductance' (c.c. $\mathrm{d}I/\mathrm{d}V$).

A consequence of the change in the height of the tip during the measurement is that it is not possible to use a numerical derivation of the current to calculate a scaling factor for the lock-in values. The current being kept at a constant value, the numerical derivation of the current will be near zero and only noise. However, because the amplitude of the modulation is small and its frequency fast, the feedback loop cannot compensate for the change in current. In other words, the feedback loop neglects the variation in current due to the lock-in modulation. However, this variation in current exists and is measured by the lock-in amplifier. At each stable bias voltage, the measurement is equivalent to a constant height measurement at this height, but the height will change between each bias voltage. This makes the data more complex to analyse.

It could be argued that since the height ($z$) changes instead of the current, we are measuring the $\mathrm{d}z/\mathrm{d}V$. However, in reality, even though the information contained in a c.c. $\mathrm{d}I/\mathrm{d}V$ has some overlap with the $\mathrm{d}z/\mathrm{d}V$, they are quantitatively and qualitatively different. Mathematically, the current is not a linear function of the height, resulting in a more complex relationship than simple proportionality between the c.c. $\mathrm{d}I/\mathrm{d}V$ and the $\mathrm{d}z/\mathrm{d}V$. Experimentally, the height variation exists because of the feedback loop and is not a direct effect. Consequently, measuring the height variation requires a low frequency, complicating the lock-in measurement. Therefore, we rely on numerical deriva-

tion to calculate the $\mathrm{d}z/\mathrm{d}V$, reducing the precision of the measurement. Even if we would implement such a scheme to record the $\mathrm{d}z/\mathrm{d}V$ directly with a lock-in amplifier, we can see in Figure 2.4 that the two curves differ in value and shape. The $\mathrm{d}z/\mathrm{d}V$ cannot reproduce the details of the c.c. $\mathrm{d}I/\mathrm{d}V$ and also differs in shape and absolute value.



### 2.1.5. INELASTIC ELECTRON TUNNELLING SPECTROSCOPY

Historically, inelastic electron tunnelling spectroscopy (IETS) refers to the study of the vibrational modes of molecules within a tunnel junction[42] by measuring the variation of the tunnelling current under a change in bias voltage. When the electrons tunnelling between the electrodes excite the molecules' vibrational modes, they open new tunnelling pathways and thus increase the conductance of the junction. Because the electron needs to transfer some of its energy to excite the vibrational mode, the process is inelastic and only occurs when the tunnelling electrons have enough energy. This gives characteristic steps in the conductance versus energy curve (or $\mathrm{d}I/\mathrm{d}V$) at the energy of the vibrational modes. The tip and sample in an STM form a junction, and the technique can be applied to STM, with the added benefit of being able to observe single molecule[43].

While initially used for vibrational excitations, STM-IETS can also be used to observe spin-excitation of atoms[44]. It is in this context that the technique will be used in this work. In this approach, the measurement is done on an atom adsorbed in a layer insulating it from a metallic substrate below to allow longer lifetimes of the excited states. For example, in chapter 5, the substrate is a monocrystal of $Cu_3Au$, the insulating layer is an island of $Cu_2N$, and the adatoms are Fe atoms. The tip is brought at a tunnelling distance to the atom, and a $\mathrm{d}I/\mathrm{d}V$ curve at constant height is measured.

At low voltage, the electron will tunnel through the atom in an elastic process, and no energy exchange occurs. However, the electrons can excite the adatom spin at specific energies by transferring some of its energy, potentially flipping the spin state in the process, before tunnelling to the other electrode. The process is inelastic as some energy is transferred; however, only excitations where the total angular momentum is conserved are permitted. The adatom will return to its ground state by interacting with the electron bath of the metallic substrate. This process opens new tunnelling pathways (or channels), similar to what happens with the vibrational modes.

Another way to understand the phenomenon is through the Bardeen formalism. In 1961, Bardeen derived a theoretical model for the current generated between two parallel electrodes[45]. The approach solves the Schrödinger equation for a time-dependent perturbative many-particle problem by considering the tip and the sample wave function as two interacting subsystems. In this formalism, the tunnelling current is proportional to the sum of the matrix elements of the transition matrix between the initial and final states, integrated over the energy distribution of the electrons. In the Bardeen formalism, the current can be written as[46]

$$I = \frac{2\pi e}{\hbar} \sum_{\mu,\nu} f\left(E_\mu\right)\left(1 - f\left(E_\nu + eV\right)\right)\left|M_{\mu\nu}\right|^2 \delta\left(E_\mu - E_\nu\right). \tag{2.11}$$

where $f$ is the temperature-dependent Fermi function defined as $f(E) = \left(1 + \exp(E\beta)\right)^{-1}$ with $\beta = 1/k_B T$ ($k_B$ being the Boltzmann constant and $T$ the temperature). $M_{\mu\nu}$ are the elements of the transition probability matrix between states where an electron moves between the tip and the sample. The equation only allows the tunnelling of an electron when the temperature-dependent Fermi distribution of the occupied electron states of the tip overlaps with the unoccupied electron states of the sample.



### 2.1.6. SPIN-PORALISED ELECTRON TUNNELLING

Another breakthrough was the advent of spin-polarised STM (SP-STM)[47, 48]. With SP-STM, the scanning tip is functionalised by a magnetic cluster at the tip apex or via a magnetic coating of the tip. Such tips will unbalance the proportion of spin ↑ and ↓ in the current tunnelling through the tip, *i.e.* the electrons in the current have a preferred spin orientation. Magnetic materials have different densities of states for spin up and spin down, leading to a conductance dependence on the spin orientation of the tunnelling electrons. This effect is called magnetoresistance. This difference in conductance will be apparent on the scan of $\mathrm{d}I/\mathrm{d}V$ when scanning magnetic atoms with non-degenerated ground states. The theory around STM-IETS and SP-STM will be explored in more detail in chapter 3.

### 2.1.7. ATOM MANIPULATION

An STM is a sensitive instrument well suited to observe one or a few atoms on a surface. Those atoms are bound to the surface but can be disturbed by high current, bias voltage, or a combination of both. This can be an experimental limitation, but it is also an opportunity. In some circumstances, it is possible to manipulate and move these atoms with a precision of picometers[13, 15, 49, 50]. The possibility of reorganising the atoms on the surface is used extensively in this work.

We can distinguish two atom manipulation classes: lateral and vertical. The main difference between the two techniques is that, for vertical manipulation, the atom is bounded with the tip (picked up) when moved before being deposed (dropped off) at a new location. The lateral manipulation methods use the tip to push or pull the atom and do not involve any tip alteration by a bounded atom. Because of that, the lateral manipulation methods are generally more reliable and allow the precise positioning and repositioning of thousands of atoms[13]. However, the possibility of using either technique depends on the specific surface, atoms and tip used in the experiment.

#### VERTICAL MANIPULATION

During a vertical manipulation[12, 50], the atom is physically transferred to the tip and deposed at another position. The pick-up and drop-off processes are accomplished by bringing the tip close to the targeted atom and applying a short bias voltage pulse. The exact parameters depend on the surface, atom and tip. This process modifies the tip apex. This makes the vertical manipulation quite delicate and prone to unwanted ef-

fects, notably picking up or deposing more than intended and irremediably altering the tip or the surface.

Nonetheless, with enough patience and meticulousness, structures including tens of atoms can be built using the technique[36]. Vertical manipulation was used to assemble the structures presented in chapter 5. The method used is a pick-up, drop-off and hop process adapted from Spinelli[51].



#### LATERAL MANIPULATION

With lateral manipulation, the atom is pushed or pulled on the surface by interacting with the tip[13, 15, 49] without bounding to it. The precise mechanisms of the manipulation can depend on several factors, including the nature of the atom, the surface, the temperature, the proximity to the atom, the tunnelling current and the bias voltage.

The typical approach to lateral manipulation, used notably by Eigler and Schweizer in their seminal paper[15], consists of positioning the tip close enough to the atom for tunnelling to occurs and applying a bias voltage so that the interaction between the tip and the atom is such that the atom will follow the tip when moved before releasing it to a new position by removing the bias voltage. In this process, the tip stay bound to the surface and is not transferred to the tip.

A more recent approach for lateral manipulation consists of making the atoms jump between bounding sites by applying a bias pulse in its vicinity. For the experiment presented in chapter 6 the vacancies of an undersaturated chlorine layer over a Cu(111) surface was used to assemble the structures on the surface. The evaporation of chlorine atoms on a Cu(100) crystal creates a square c$(2 \times 2)$ reconstruction monolayer of chlorine on top of the metallic surface[13]. If the evaporation is made so the chlorine atoms do not saturate the surface, it will contain defects, *i.e.* missing chlorine atoms. These holes in the chlorine lattice are called chlorine vacancies or simply vacancies.

Moving the chlorine vacancies and placing them precisely at the atomic scale is possible. In Figure 6.1, an STM image taken at 600 mV shows a Cl/Cu(100) surface containing multiple vacancies and some artificially assembled clusters of vacancies placed using a horizontal manipulation procedure. First, the tip is positioned midway between a chlorine atom and a vacancy. Afterwards, a bias voltage pulse is applied between the tip and the sample. The pulse induces a jump of the atom to a neighbouring binding site. The tip position will bias the direction of the jump. When the chlorine atom moves into the neighbouring vacancy, it leaves behind a new vacancy, effectively moving it. The vacancies host vacuum surface state that can be used to engineer artificial structures[52, 53] and will be studied further in chapter 6.

## 2.2. EXPERIMENTAL SETUPS

An STM depends on multiple systems to function correctly. At its core, it needs systems to precisely position the tip, isolate it from mechanical noise and thermal fluctuation,

control the applied bias voltage, and measure the tunnelling current. Other typical systems include pump and vacuum chambers, cryostat for cooling, magnetic field generators and in-situ sample preparation instruments. We will briefly introduce those different systems and the experimental setup available in our labs and used in this work.



The group have access to two STMs in their laboratories: a SPECS$^{TM}$ JT-STM and a UNISOKU$^{TM}$ USM-1300. Both of the STMs were used for the work described here. The JT-STM was used for the field emission resonance of chapter 6, and the USM-1300 was used for the study of copper nitride island on copper-gold in chapter 4 and of magnetically frustrated spin loops in chapter 5. The two machines are cryogenic, ultra-high vacuum STM. The metal substrates used as bases for the samples are commercially bought single crystals. They are inserted inside a vacuum chamber connected to the rest of the systems and prepared *in situ* using a combination of ion gun for sample, electron beam annealing and evaporators for molecular and atomic deposition. The different chambers attached to the STM are kept under a vacuum below $10^{-}9$ mbar by turbopumps and molecular pumps.

### 2.2.1. JT-STM

The SPECS$^{TM}$ JT-STM is a commercial Joules-Thomson STM from SPECS. The tip and the sample are mounted vertically, with the sample at the bottom and approaching the tip from below. The tip and sample stage can be visually accessed via a window, and a manipulator allows changing the sample and tip. This window and the manipulator make the STM easy to use and suitable for studies that require changing the sample often. The STM head is at the center of a split-coil superconducting magnet that allows a magnetic field of up to 3 Tesla out-of-plane (*i.e.* , perpendicular to the sample surface) and resides at the bottom of a cryostat formed by two hollow concentric cylinders.

The outer cylinder is filled with liquid nitrogen, allowing a stable operation at 77 K. This temperature regime was not used in the current work. The inner cylinder can be filled with liquid helium-4, giving access to a stable 4 K temperature. The STM also allows a lower temperature, made possible by the Joule-Thomson pot situated near the sample stage. In normal operation mode, a physical bridge connects the STM head to the inner cryostat keeping the head a 4K. Removing that link and allowing the head to only be cooled by the JT pot make operating at a temperature of 1K possible.

### 2.2.2. USM 1300

The UNISOKU$^{TM}$ USM-1300S is a commercial low-temperature ultra-high vacuum $^{3}$He system. The tip and sample are mounted vertically, with the tip at the bottom. The sample is approached from above. Contrary to the JT-STM, the sample and tip manipulations are done without visual aid, making the USM-1300S a more difficult machine to operate. The STM head is situated in the centre of a large cryostat that can contain up to 130 litres of $^{3}$He. Near the STM head, inside the cryostat, a pot allows the pumping of the helium through a valve to cool the STM head by Joule-Thomson effect. Also present is a $^{3}$He pot thermally connected to the sample stage where it is possible to condense

the $^3$He to cool the system further. This setup allows the STM to operate at two stable temperatures: 1.5 K during normal operation mode or 330 mK during condensation the $^3$He. The reservoir of 20 litres of $^3$He gas allows it to operate in single shot mode at its base temperature of 330 mK for approximately 24 hours.

The STM head is situated at the centre of a 2D superconducting magnet. The field out-of-plane can reach up to 9 Tesla, and the field parallel to the surface 2 Tesla. Like the JT-STM, the USM 1300 is connected to a series of vacuum chambers kept at room temperature allowing the preparation of the samples.



## 2.3. FIELD EMISSION RESONANCES

Directly above a surface *extrinsic surface states* exist, known as image potential states (IPS)[54–56]. These states originate from an attractive potential toward the surface, the image potential, combined with a bulk bandgap at the right energy that prevents the electrons from entering the surface. These two effects trap the electrons above the surface, outside the bulk. It is possible to observe those states using an STM.

### 2.3.1. IMAGE POTENTIAL STATES (IPS)

Shockley[57] envisaged the existence of these extrinsic states in 1939 in his work on surface states, but it is Cole and Cohen, in their 1969 pioneer work[54] that gave a more concrete description and defined criteria for their existence. They speculated their presence at the surface of insulating materials. They established conditions for observing IPS (called *surface bands* in the publication) on insulating materials, notably near the surface of a liquid or solid $^3$He, $^4$He, Ne, $H_2$ and $D_2$. The peculiar motion of helium ions near their vapour-liquid interface observed by Shikin[58] (1970) was later attributed to the existence of those states [55].

Echenique and Pendry[59] significantly extended the theoretical foundation of the IPS and predicted that IPS could also exist on a metal surface[56]. They applied a similar approach to the one used for deriving surface states[60] where the Schödinger equation is used to calculate reflections at interfaces and the resulting stable states. They also proposed using Low-Energy Electron Diffraction (LEED) to observe IPS experimentally and revisited results from an earlier LEED experiment by McRae[61]. The observed resonances were coherent with the presence of IPS. Shortly after, McRae repeated similar experiments on other metal surfaces[62] and again observed similar resonances.

Even if the McRae LEED experiments gave the first clues of the existence of IPS, it was in 1983 that more concrete evidence came from inverse-photoemission experiments by Johnson and Smith[63], and finally, by Dose *et al.*[64] in 1984. They later used momentum-resolved photoemission on bare Cu(100) surfaces and on chlorine-covered copper (100) to demonstrate that the emission is pinned to the vacuum level, shows free-electron-like dispersion, and is independent of the temperature in terms of intensity. These observations confirmed the IPS nature of the emissions. Following these results, multiple variations of photoemission experiments were used to probe and char-

acterise the IPS. For example, two photon photoemissions (2PPE)[65, 66], inverse photoemission [67], bichromatic 2PPE[68], angle-resolved 2PPE[69] and time-resolved and momentum-resolved 2PPE[70–74]. Those experiments allowed notably to establish that the electrons form a 2D gas over the surface with free-like motion parallel to the surface, the energy of IPS on multiple surfaces, and their lifetimes.

The newly developed STM by Binnig and Rohrer[75] revealed itself to be a valuable experimental tool to study IPS[76–79]. In particular, contrary to the previously mentioned methods that always give averaged values over a large surface, STM allows observation of localised IPS and their variation caused by the surface inhomogeneity[80, 80–84].

### 2.3.2. THE IMAGE POTENTIAL (IP)

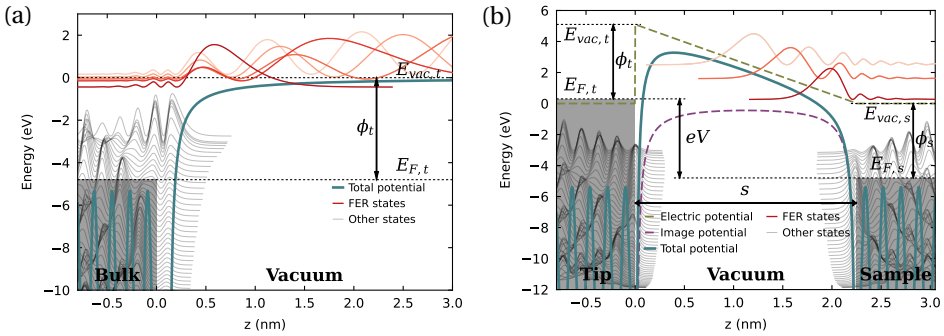


**Figure 2.5: Examples of IPS on a single surface and on a tip-sample interface.** (a) Potential (teal) and states (grey/red) over a Cu(100) surface. The image potential, in blue, have the form $-1/4(z-z_i)$ with $z_i$ the image plane distance.(b) The potentials and states around an STM junction in the presence of both tip and sample. The vacuum potential is the sum of a plate-plate potential between the tip and the sample with a bias voltage of 5.1 V, and a tip-sample distance is 2.25 nm. (a,b) The image plane is $z_i = 0.123$ nm[85]. More information about the calculations, the potentials and the parameters can be read in section 3.4.

The electric charge of an electron near a surface disturbs the distribution of charge inside the solid[86]. Its negative charge repels the electrons inside the solid, creating a deficit in the distribution of electrons. This can effectively create a positive charge inside the solid that attracts the vacuum electron. The vacuum electron is attracted to the surface by its perturbation of the surface. This effect is particularly pronounced in metals, where electrons can move easily, but can be observed in other materials.

The redistribution of charges is made apparent by the method often used to evaluate the electric field caused by a charge near a conducting surface, the image method[87]. The reasoning goes as follows, to ensure that all field lines are perpendicular to the surface at the boundary, so no lateral force exists, as it should be for a conductor, an imaginary inverse charge is placed at the same distance from the surface but inside the solid. This ensures that the forces parallel to the surface cancel out at the interface, only leaving the perpendicular forces. By doing so, the sum of the potential of the two charges, the real and the image, correctly describes the potential outside the conductor. The image

method is also used to solve more complex problems, for example, the charged sphere near a conductor used in section 3.4. This mathematical 'trick' reveals itself to be a real effect and has consequences on the physics of the surface.

Using the image method, we can derive the form that the image potential takes as [88, 89]

$$V_{\text{im}} = -\frac{1}{4z}, \tag{2.12}$$

where $z$ is the distance from the surface. If, in addition to this attractive potential, a bandgap prevents the electron from entering the solid at certain energies, typically close to the vacuum energy, an electron can be trapped above the surface, forming the states that we call IPS. Trapped between the IP and the surface, the states form a Rydberg series converging to the vacuum with an energy distribution as [56, 73, 90, 91]

$$E_n = -\left[32(n+a)^2\right]^{-1} \tag{2.13}$$

where $n$ is the quantum number. The value of $a$ depends on the relative position of the bandgap and the vacuum level[59]. For reference, for a (100) copper surface $a \approx 0.28$[59]. This potential can be used to quantitatively model the IPS[56, 68, 92, 93].

Figure 2.5(a) shows an example of calculation results from a Cu(100) surface. The IPS states are highlighted in red. They form between the surface ($z = 0$) and the IP, with only a quickly dying tail inside the bulk. The potential asymptotically reaches the vacuum level ($E = 0$). The way the calculation is performed is explained in section 3.4.

### 2.3.3. FIELD EMISSION RESONANCE (FER)

One of the fundamental concepts of STM is the voltage bias applied between the tip and the sample responsible for the quantum tunnelling current measured at the junction. This bias voltage generates an electrostatic field between the tip and the sample. If the field is strong enough, it can generate field-emitted electrons, creating current even when the quantum tunnelling contribution is negligible. This current can be particularly important if the energy of the electrons corresponds to the energy of an IPS. When this condition is fulfilled, the electrons can populate the image potential states and tunnel through them, resulting in a significantly higher current than otherwise. This phenomenon is called field-emission resonance (FER) and is characterised by strong conduction peaks in the differential conductance spectra at specific energies above the work function of the surface. The energies at which the FER can be observed vary with the separation of the tip and the sample[94], as well as with the applied bias voltage[76], and the nature of the tip and of the sample[83].

There are no IPS above the vacuum energy on a single surface as the IP asymptotically reaches the vacuum energy, and so only states below that energy can exist. In the case of the STM, the second surface (the tip) and the electromagnetic field change the potential landscape and create a potential wall that can be higher than the vacuum energy. The IPS are pushed to higher energy allowing the observation of FER. The potential shape will be discussed in section 3.4.

In short, IPS and FER can be viewed as two aspects of the same phenomenon, the latter being an experimental observation (a resonance) of the first under a finite bias at an STM junction.



### 2.3.4. SHOCKLEY AND TAMM STATES

A discussion on IPS would not be complete without introducing the Shockley states[57] and the Tamm states[95]. They can also be observed near some surfaces, but contrary to the IPS, they mostly exist inside the bulk and show a tail that quickly dies out in the vacuum. Because they are predominantly internal to the solid, they are also called *intrinsic surface states* or simply *surface states*. In the same way, the IPS are also called *extrinsic surface states*. It should be noted that while Shockley states and the Tamm states are sometimes described as two separate phenomena, they only differ in their theoretical modeling[96].

The Shockley and the Tamm states' theoretical proposition originates from the observation that a solid's last plane of atoms (the surface) is fundamentally different from the inside of the solid. There is a breaking of symmetry at the interface. The atoms forming the surface have fewer neighbouring atoms than the bulk, and so some bonds that the atoms typically create inside the bulk are broken; the formation of a surface costs energy[96]. Consequently, the surface electronic structure differs from the bulk electronics structures. Many phenomena are linked to this change in the electronic structure, for example, the specific chemical reactivity and the surface free energy[97].

Shockley derived the existence of intrinsic surface states by solving the Schrödinger equation of a one-dimensional semi-infinite periodic potential in a nearly-free-electron approach[98]. The potential models the periodicity of the bulk until it reaches the end of the solid and smoothly reaches the vacuum potential. This smooth transition was used by Shockley but is not essential for the derivation of the surface states. Shockley showed that, depending on the potential period, some states can exist between projected bandgaps and that those states only exist in the vicinity of the surface. He also extended his model in three dimensions, showing that the solutions follow a Bloch wave propagation parallel to the surface.

Tamm tackled the problem by using a tightly bound electrons model and considering the wave functions as linear combinations of atomic orbitals (LCAO). In this description, the outmost layer (surface) has fewer neighbours than the preceding layers (bulk), which translates into fewer bonds, leading to the existence of dangling bonds[96] at the surface. This difference in the atoms' electronic configuration will lower the wave functions' overlap compared to the wave functions inside the bulk, making the wave functions of the surface atoms closer to the free atom's wave functions. The wave function overlap results in the states splitting (gap) and shifting. With this effect being stronger in the bulk than at the surface, states at the surface can exist inside this bulk gap, thus creating localised surface states.

# REFERENCES


[1] G. Binnig and H. Rohrer, *Scanning tunneling microscopy,* Surface Science **126**, 236 (1983).

[2] G. Binnig and H. Rohrer, *Scanning tunneling microscopy—from birth to adolescence,* Rev. Mod. Phys. **59**, 615 (1987).

[3] D. P. E. Smith, H. Hörber, Ch. Gerber, and G. Binnig, *Smectic Liquid Crystal Monolayers on Graphite Observed by Scanning Tunneling Microscopy,* Science **245**, 43 (1989).

[4] S. De Feyter and F. C. De Schryver, *Self-Assembly at the Liquid/Solid Interface: STM Reveals,* J. Phys. Chem. B **109**, 4290 (2005).

[5] G. C. McGonigal, R. H. Bernhardt, and D. J. Thomson, *Imaging alkane layers at the liquid/graphite interface with the scanning tunneling microscope,* Appl. Phys. Lett. **57**, 28 (1990).

[6] J. S. Foster and J. E. Frommer, *Imaging of liquid crystals using a tunnelling microscope,* Nature **333**, 542 (1988).

[7] T. A. Jung, R. R. Schlittler, and J. K. Gimzewski, *Conformational identification of individual adsorbed molecules with the STM,* Nature **386**, 696 (1997).

[8] I. S. Tilinin, M. K. Rose, J. C. Dunphy, M. Salmeron, and M. A. Van Hove, *Identification of adatoms on metal surfaces by STM: Experiment and theory,* Surface Science **418**, 511 (1998).

[9] P. T. Wouda, M. Schmid, B. E. Nieuwenhuys, and P. Varga, *STM study of the (111) and (100) surfaces of PdAg,* Surface Science **417**, 292 (1998).

[10] A. A. Saranin, A. V. Zotov, V. G. Lifshits, J. T. Ryu, O. Kubo, H. Tani, T. Harada, M. Katayama, and K. Oura, *Analysis of surface structures through determination of their composition using STM: Si(100)4x3-In and Si(111)4x1-In reconstructions,* Phys. Rev. B **60**, 14372 (1999).

[11] L. Bartels, G. Meyer, and K.-H. Rieder, *Basic Steps of Lateral Manipulation of Single Atoms and Diatomic Clusters with a Scanning Tunneling Microscope Tip,* Phys. Rev. Lett. **79**, 697 (1997).

[12] D. M. Eigler, C. P. Lutz, and W. E. Rudge, *An atomic switch realized with the scanning tunnelling microscope,* Nature **352**, 600 (1991).

[13] F. E. Kalff, M. P. Rebergen, E. Fahrenfort, J. Girovsky, R. Toskovic, J. L. Lado, J. Fernández-Rossier, and A. F. Otte, *A kilobyte rewritable atomic memory,* Nat Nano **11**, 926 (2016).

[14] I.-W. Lyo and P. Avouris, *Field-Induced Nanometer- to Atomic-Scale Manipulation of Silicon Surfaces with the STM,* Science **253**, 173 (1991).

[15] D. M. Eigler and E. K. Schweizer, *Positioning single atoms with a scanning tunnelling microscope,* Nature **344**, 524 (1990).

[16] A. Spinelli, B. Bryant, F. Delgado, J. Fernández-Rossier, and A. F. Otte, *Imaging of spin waves in atomically designed nanomagnets,* Nat Mater **13**, 782 (2014).

[17] S. Yan, L. Malavolti, J. A. J. Burgess, A. Droghetti, A. Rubio, and S. Loth, *Nonlocally sensing the magnetic states of nanoscale antiferromagnets with an atomic spin sensor,* Science Advances **3**, e1603137 (2017).

[18] M. N. Huda, S. Kezilebieke, and P. Liljeroth, *Designer flat bands in quasi-one-dimensional atomic lattices,* Phys. Rev. Research **2**, 043426 (2020).

[19] L. Yan and P. Liljeroth, *Engineered electronic states in atomically precise artificial lattices and graphene nanoribbons,* Advances in Physics: X **4**, 1651672 (2019).

[20] M. Bode, M. Getzlaff, and R. Wiesendanger, *Spin-Polarized Vacuum Tunneling into the Exchange-Split Surface State of Gd(0001),* Phys. Rev. Lett. **81**, 4256 (1998).

[21] M. Cavallini and F. Biscarini, *Electrochemically etched nickel tips for spin polarized scanning tunneling microscopy,* Review of Scientific Instruments **71**, 4457 (2000).

[22] A. Kubetzka, M. Bode, O. Pietzsch, and R. Wiesendanger, *Spin-Polarized Scanning Tunneling Microscopy with Antiferromagnetic Probe Tips,* Phys. Rev. Lett. **88**, 057201 (2002).

[23] A. Li Bassi, C. S. Casari, D. Cattaneo, F. Donati, S. Foglio, M. Passoni, C. E. Bottani, P. Biagioni, A. Brambilla, M. Finazzi, F. Ciccacci, and L. Duò, *Bulk Cr tips for scanning tunneling microscopy and spin-polarized scanning tunneling microscopy,* Appl. Phys. Lett. **91**, 173120 (2007).

[24] R. Wiesendanger, H.-J. Güntherodt, G. Güntherodt, R. J. Gambino, and R. Ruf, *Observation of vacuum tunneling of spin-polarized electrons with the scanning tunneling microscope,* Phys. Rev. Lett. **65**, 247 (1990).

[25] D. Wortmann, S. Heinze, Ph. Kurz, G. Bihlmayer, and S. Blügel, *Resolving Complex Atomic-Scale Spin Structures by Spin-Polarized Scanning Tunneling Microscopy,* Phys. Rev. Lett. **86**, 4132 (2001).

[26] S. Loth, M. Etzkorn, C. P. Lutz, D. M. Eigler, and A. J. Heinrich, *Measurement of Fast Electron Spin Relaxation Times with Atomic Resolution,* Science **329**, 1628 (2010).

[27] F. Delgado, S. Loth, M. Zielinski, and J. Fernández-Rossier, *The emergence of classical behaviour in magnetic adatoms,* EPL **109**, 57001 (2015).

[28] S. Baumann, W. Paul, T. Choi, C. P. Lutz, A. Ardavan, and A. J. Heinrich, *Electron paramagnetic resonance of individual atoms on a surface,* Science **350**, 417 (2015).

[29] M. Rashidi, J. A. J. Burgess, M. Taucer, R. Achal, J. L. Pitters, S. Loth, and R. A. Wolkow, *Time-resolved single dopant charge dynamics in silicon,* Nature Communications **7**, 13258 (2016).

[30] S. Yan, D.-J. Choi, J. A. J. Burgess, S. Rolf-Pissarczyk, and S. Loth, *Control of quantum magnets by atomic exchange bias,* Nature Nanotechnology **10**, 40 (2015).

[31] L. M. Veldman, L. Farinacci, R. Rejali, R. Broekhoven, J. Gobeil, D. Coffey, M. Ternes, and A. F. Otte, *Free coherent evolution of a coupled atomic spin system initialized by electron scattering,* Science **372**, 964 (2021).

[32] A. Spinelli, M. Gerrits, R. Toskovic, B. Bryant, M. Ternes, and A. F. Otte, *Exploring the phase diagram of the two-impurity Kondo problem,* Nature Communications **6**, 10046 (2015).

[33] R. Toskovic, R. van den Berg, A. Spinelli, I. S. Eliens, B. van den Toorn, B. Bryant, J.-S. Caux, and A. F. Otte, *Atomic spin-chain realization of a model for quantum criticality,* Nat Phys **12**, 656 (2016).

[34] L. Farinacci, L. M. Veldman, P. Willke, and S. Otte, *Experimental Determination of a Single Atom Ground State Orbital through Hyperfine Anisotropy,* Nano Lett. **22**, 8470 (2022).

[35] S. Baumann, F. Donati, S. Stepanow, S. Rusponi, W. Paul, S. Gangopadhyay, I. G. Rau, G. E. Pacchioni, L. Gragnaniello, M. Pivetta, J. Dreiser, C. Piamonteze, C. P. Lutz, R. M. Macfarlane, B. A. Jones, P. Gambardella, A. J. Heinrich, and H. Brune, *Origin of Perpendicular Magnetic Anisotropy and Large Orbital Moment in Fe Atoms on MgO,* Phys. Rev. Lett. **115**, 237202 (2015).

[36] S. Loth, S. Baumann, C. P. Lutz, D. M. Eigler, and A. J. Heinrich, *Bistability in Atomic-Scale Antiferromagnets,* Science **335**, 196 (2012).

[37] L. Mandelstam and Ig. Tamm, *The Uncertainty Relation Between Energy and Time in Non-relativistic Quantum Mechanics,* in *Selected Papers* (Springer Berlin Heidelberg, Berlin, Heidelberg, 1991) pp. 115–123.

[38] M. B. King, *Quest for Zero Point Energy: Engineering Principles for 'free Energy' Inventions* (Adventures Unlimited Press, 2001).

[39] L. Marchildon, *Quantum Mechanics: From Basic Principles to Numerical Methods and Applications*, Advanced Texts in Physics (Springer-Verlag, Berlin Heidelberg, 2002).

[40] D. J. Griffiths and D. F. Schroeter, *Introduction to Quantum Mechanics*, 3rd ed. (Cambridge University Press, Cambridge, 2018).

[41] J. M. de Voogd, M. A. van Spronsen, F. E. Kalff, B. Bryant, O. Ostojić, A. M. J. den Haan, I. M. N. Groot, T. H. Oosterkamp, A. F. Otte, and M. J. Rost, *Fast and reliable pre-approach for scanning probe microscopes based on tip-sample capacitance,* Ultramicroscopy **181**, 61 (2017).

[42] J. Lambe and R. C. Jaklevic, *Molecular Vibration Spectra by Inelastic Electron Tunneling,* Phys. Rev. **165**, 821 (1968).

[43] B. C. Stipe, M. A. Rezaei, and W. Ho, *Single-Molecule Vibrational Spectroscopy and Microscopy,* Science **280**, 1732 (1998).

[44] A. J. Heinrich, J. A. Gupta, C. P. Lutz, and D. M. Eigler, *Single-Atom Spin-Flip Spectroscopy,* Science **306**, 466 (2004).

[45] J. Bardeen, *Tunnelling from a Many-Particle Point of View,* Phys. Rev. Lett. **6**, 57 (1961).

[46] J. Tersoff and D. R. Hamann, *Theory of the scanning tunneling microscope,* Phys. Rev. B **31**, 805 (1985).

[47] M. Bode, M. Heide, K. von Bergmann, P. Ferriani, S. Heinze, G. Bihlmayer, A. Kubetzka, O. Pietzsch, S. Blügel, and R. Wiesendanger, *Chiral magnetic order at surfaces driven by inversion asymmetry,* Nature **447**, 190 (2007).

[48] M. Bode, *Spin-polarized scanning tunnelling microscopy,* Rep. Prog. Phys. **66**, 523 (2003).

[49] M. F. Crommie, C. P. Lutz, and D. M. Eigler, *Confinement of Electrons to Quantum Corrals on a Metal Surface,* Science **262**, 218 (1993).

[50] C. F. Hirjibehedin, C. P. Lutz, and A. J. Heinrich, *Spin Coupling in Engineered Atomic Structures,* Science **312**, 1021 (2006).

[51] A. Spinelli, M. P. Rebergen, and a. A. F. Otte, *Atomically crafted spin lattices as model systems for quantum magnetism,* Journal of Physics: Condensed Matter **27**, 243203 (2015).

[52] R. Drost, T. Ojanen, A. Harju, and P. Liljeroth, *Topological states in engineered atomic lattices,* Nature Phys **13**, 668 (2017).

[53] J. Girovsky, J. Lado, S. Otte, F. Kalff, E. Fahrenfort, L. Peters, and J. Fernández-Rossier, *Emergence of quasiparticle Bloch states in artificial crystals crafted atom-by-atom,* SciPost Physics **2**, 020 (2017).

[54] M. W. Cole and M. H. Cohen, *Image-Potential-Induced Surface Bands in Insulators,* Phys. Rev. Lett. **23**, 1238 (1969).

[55] M. W. Cole, *Electronic Surface States of a Dielectric Film on a Metal Substrate,* Phys. Rev. B **3**, 4418 (1971).

[56] P. M. Echenique and J. B. Pendry, *The existence and detection of Rydberg states at surfaces,* Journal of Physics C: Solid State Physics **11**, 2065 (1978).

[57] W. Shockley, *On the Surface States Associated with a Periodic Potential,* Phys. Rev. **56**, 317 (1939).

[58] V. B. Shikin, *Motion of helium ions near a vaport-liquid surface,* Soviet Physics JETP **31**, 5 (1970).

[59] P. M. Echenique and J. B. Pendry, *Theory of image states at metal surfaces,* Progress in Surface Science **32**, 111 (1989).

[60] J. B. Pendry and S. J. Gurman, *Theory of surface states: General criteria for their existence,* Surface Science **49**, 87 (1975).

[61] E. G. McRae and C. W. Caldwell, *Observation of multiple scattering resonance effects in low energy electron diffraction studies of LiF, NaF and graphite,* Surface Science **7**, 41 (1967).

[62] E. G. McRae, *Electronic surface resonances of crystals,* Rev. Mod. Phys. **51**, 541 (1979).

[63] P. D. Johnson and N. V. Smith, *Image-potential states and energy-loss satellites in inverse photoemission spectra,* Phys. Rev. B **27**, 2527 (1983).

[64] V. Dose, W. Altmann, A. Goldmann, U. Kolac, and J. Rogozik, *Image-Potential States Observed by Inverse Photoemission,* Phys. Rev. Lett. **52**, 1919 (1984).

[65] K. Giesen, F. Hage, F. J. Himpsel, H. J. Riess, W. Steinmann, and N. V. Smith, *Effective mass of image-potential states,* Phys. Rev. B **35**, 975 (1987).

[66] Ch. Reuß, I. L. Shumay, U. Thomann, M. Kutschera, M. Weinelt, Th. Fauster, and U. Höfer, *Control of the Dephasing of Image-Potential States by CO Adsorption on Cu(100),* Phys. Rev. Lett. **82**, 153 (1999).

[67] N. Garcia, B. Reihl, K. H. Frank, and A. R. Williams, *Image States: Binding Energies, Effective Masses, and Surface Corrugation,* Phys. Rev. Lett. **54**, 591 (1985).

[68] S. Schuppler, N. Fischer, Th. Fauster, and W. Steinmann, *Bichromatic two-photon photoemission spectroscopy of image potential states on Ag(100),* Appl. Phys. A **51**, 322 (1990).

[69] J. D. McNeill, R. L. Lingle, R. E. Jordan, D. F. Padowitz, and C. B. Harris, *Interfacial quantum well states of Xe and Kr adsorbed on Ag(111),* The Journal of Chemical Physics **105**, 3883 (1996).

[70] U. Höfer, I. L. Shumay, C. Reuß, U. Thomann, W. Wallauer, and T. Fauster, *Time-Resolved Coherent Photoelectron Spectroscopy of Quantized Electronic States on Metal Surfaces,* Science **277**, 1480 (1997).

[71] I. L. Shumay, U. Höfer, Ch. Reuß, U. Thomann, W. Wallauer, and Th. Fauster, *Lifetimes of image-potential states on Cu(100) and Ag(100) measured by femtosecond time-resolved two-photon photoemission,* Phys. Rev. B **58**, 13974 (1998).

[72] W. Berthold, U. Höfer, P. Feulner, E. V. Chulkov, V. M. Silkin, and P. M. Echenique, *Momentum-Resolved Lifetimes of Image-Potential States on Cu(100),* Phys. Rev. Lett. **88**, 056805 (2002).

[73] K. Schubert, A. Damm, S. V. Eremeev, M. Marks, M. Shibuta, W. Berthold, J. Güdde, A. G. Borisov, S. S. Tsirkin, E. V. Chulkov, and U. Höfer, *Momentum-resolved electron dynamics of image-potential states on Cu and Ag surfaces,* Phys. Rev. B **85**, 205431 (2012).

[74] M. Rohleder, W. Berthold, J. Güdde, and U. Höfer, *Time-Resolved Two-Photon Photoemission of Buried Interface States in Ar/Cu(100),* Phys. Rev. Lett. **94**, 017401 (2005).

[75] G. Binnig, H. Rohrer, Ch. Gerber, and E. Weibel, *Surface Studies by Scanning Tunneling Microscopy,* Phys. Rev. Lett. **49**, 57 (1982).

[76] G. Binnig, K. H. Frank, H. Fuchs, N. Garcia, B. Reihl, H. Rohrer, F. Salvan, and A. R. Williams, *Tunneling Spectroscopy and Inverse Photoemission: Image and Field States,* Phys. Rev. Lett. **55**, 991 (1985).

[77] R. S. Becker, J. A. Golovchenko, and B. S. Swartzentruber, *Electron Interferometry at Crystal Surfaces,* Phys. Rev. Lett. **55**, 987 (1985).

[78] L. Bürgi, O. Jeandupeux, H. Brune, and K. Kern, *Probing Hot-Electron Dynamics at Surfaces with a Cold Scanning Tunneling Microscope,* Phys. Rev. Lett. **82**, 4516 (1999).

[79] P. Wahl, M. A. Schneider, L. Diekhöner, R. Vogelgesang, and K. Kern, *Quantum Coherence of Image-Potential States,* Phys. Rev. Lett. **91**, 106802 (2003).

[80] T. Jung, Y. W. Mo, and F. J. Himpsel, *Identification of Metals in Scanning Tunneling Microscopy via Image States,* Phys. Rev. Lett. **74**, 1641 (1995).

[81] M. Pivetta, F. Patthey, M. Stengel, A. Baldereschi, and W.-D. Schneider, *Local work function Moir\'e pattern on ultrathin ionic films: NaCl on Ag(100),* Phys. Rev. B **72**, 115404 (2005).

[82] H.-C. Ploigt, C. Brun, M. Pivetta, F. Patthey, and W.-D. Schneider, *Local work function changes determined by field emission resonances: NaCl/Ag(100),* Phys. Rev. B **76**, 195404 (2007).

[83] P. Ruffieux, K. Aït-Mansour, A. Bendounan, R. Fasel, L. Patthey, P. Gröning, and O. Gröning, *Mapping the Electronic Surface Potential of Nanostructured Surfaces,* Phys. Rev. Lett. **102**, 086807 (2009).

[84] S. Stepanow, A. Mugarza, G. Ceballos, P. Gambardella, I. Aldazabal, A. G. Borisov, and A. Arnau, *Localization, splitting, and mixing of field emission resonances induced by alkali metal clusters on Cu(100),* Phys. Rev. B **83**, 115101 (2011).

[85] N. V. Smith, C. T. Chen, and M. Weinert, *Distance of the image plane from metal surfaces,* Phys. Rev. B **40**, 7565 (1989).

[86] N. D. Lang and W. Kohn, *Theory of Metal Surfaces: Induced Surface Charge and Image Potential,* Phys. Rev. B **7**, 3541 (1973).

[87] D. J. Griffiths, *Introduction to Electrodynamics*, 4th ed. (Cambridge University Press, Cambridge, United Kingdom ; New York, NY, 2017).

[88] P. M. Echenique, J. M. Pitarke, E. V. Chulkov, and V. M. Silkin, *Image-potential-induced states at metal surfaces,* Journal of Electron Spectroscopy and Related Phenomena Special Issue in Honor of Neville V. Smith and Charles Fadley's 60th Birthdays, **126**, 163 (2002).

[89] P. M. Echenique, R. Berndt, E. V. Chulkov, Th. Fauster, A. Goldmann, and U. Höfer, *Decay of electronic excitations at metal surfaces,* Surface Science Reports **52**, 219 (2004).

[90] D. Straub and F. J. Himpsel, *Identification of Image-Potential Surface States on Metals,* Phys. Rev. Lett. **52**, 1922 (1984).

[91] N. V. Smith, *Phase analysis of image states and surface states associated with nearly-free-electron band gaps,* Phys. Rev. B **32**, 3549 (1985).

[92] R. E. Dietz, E. G. McRae, and R. L. Campbell, *Saturation of the Image Potential Observed in Low-Energy Electron Reflection at Cu(001) Surface,* Phys. Rev. Lett. **45**, 1280 (1980).

[93] P. J. Jennings and R. O. Jones, *Surface barrier determination using spin-polarized LEED: W(001),* Solid State Communications **44**, 17 (1982).

[94] D. B. Dougherty, P. Maksymovych, J. Lee, M. Feng, H. Petek, and J. T. Yates, *Tunneling spectroscopy of Stark-shifted image potential states on Cu and Au surfaces,* Phys. Rev. B **76**, 125428 (2007).

[95] I. Tamm, *On the possible bound states of electrons on a crystal surface,* Phys. Z. Sowjetunion **1**, 733 (1932).

[96] H. Lüth, *Solid Surfaces, Interfaces and Thin Films*, Graduate Texts in Physics (Springer International Publishing, Cham, 2015).

[97] H. Ibach, *Physics of Surfaces and Interfaces* (Springer, Berlin ; New York, 2006).

[98] E. T. Goodwin, *Electronic states at the surfaces of crystals: I. The approximation of nearly free electrons,* Mathematical Proceedings of the Cambridge Philosophical Society **35**, 205 (1939).

# 3

# NUMERICAL METHODS AND MODELS

*This chapter lays the theoretical and computational groundwork necessary to understand and interpret the experimental observations detailed in the following chapters. We present the numerical methods and models for simulating frustrated spin loops and image potential states. We describe the spin Hamiltonian model, including Zeeman energy, magnetic anisotropy, and Heisenberg coupling, which form the basis for evaluating the spin states. To model the observable current, we use the rate equation model and Pauli Master Equation. This model enables us to predict transitions between quantum states, helping our understanding of quantum dynamics. Finally, an approach to solving the Schrödinger equation to evaluate the wavefunction of image potential states using 1D and 2D models is presented. This allows us to analyse the complex potential created by specific atomic configurations and their impact on trapped electrons.*

## 3.1. SPIN HAMILTONIAN MODEL

The first element needed to compute the current is a model of the atomic system that the electrons will tunnel through. Our system of interest is a single or few coupled magnetic atoms adsorbed on an insulating layer. A typical and helpful model is the Spin Hamiltonian model. This model can reproduce both the position and the height of the step in an IETS curve.



The model will be assembled step-by-step to understand the effect of each part of the Hamiltonian. Fe adatom on an $Cu_2N$ island is used as a concrete numerical example of the model. This system is also the base of the experiment presented in chapter 4 and chapter 5.

As a basis, let us define some basic concepts. The Hamiltonian uses the spin operator defined as

$$\vec{S} = \begin{pmatrix} \hat{S}_x \\ \hat{S}_y \\ \hat{S}_z \end{pmatrix} \tag{3.1}$$

where the $\hat{S}_i$ are the spin components along the $x$, $y$ and $z$ axes. The spin components matrix elements can be evaluated using

$$\langle m'|\hat{S}_x|m\rangle = \frac{\hbar}{2}\left(\delta_{m'+1,m} + \delta_{m',m+1}\right)\sqrt{s(s+1) - m'm} \tag{3.2}$$

$$\langle m'|\hat{S}_y|m\rangle = i\frac{\hbar}{2}\left(\delta_{m'+1,m} - \delta_{m',m+1}\right)\sqrt{s(s+1) - m'm} \tag{3.3}$$

$$\langle m'|\hat{S}_z|m\rangle = \hbar\delta_{m',m}m \tag{3.4}$$

with $\{m, m'\} = -s, -s+1, \ldots, s$, where $s$ is the spin quantum number of the particle or atom. For reference, for an electron where $s = 1/2$, the spin components are

$$\hat{S}_x = \frac{\hbar}{2}\begin{pmatrix} 0 & 1 \\ 1 & 0 \end{pmatrix}, \quad \hat{S}_y = \frac{\hbar}{2}\begin{pmatrix} 0 & -i \\ i & 0 \end{pmatrix}, \quad \hat{S}_z = \frac{\hbar}{2}\begin{pmatrix} 1 & 0 \\ 0 & -1 \end{pmatrix} \tag{3.5}$$

or, using the Pauli matrices

$$\hat{S}_i = \frac{\hbar}{2}\hat{\sigma}_i. \tag{3.6}$$

If multiple spins interact in a system, it is necessary to build a larger space. The Kronecker space, or tensor product space, is a way to combine smaller Hilbert spaces into a larger space. The tensor product space is not exclusive to quantum mechanics but has applications in various mathematics branches like linear algebra and tensor analysis.

The space is built using the Kronecker product, or tensor product symbolised by the symbol $\otimes$. The tensor product map two subspace in a larger space as follows

$$\begin{pmatrix} a_{11} & a_{12} \\ a_{21} & a_{22} \end{pmatrix} \otimes \begin{pmatrix} b_{11} & b_{12} \\ b_{21} & b_{22} \end{pmatrix} = \begin{pmatrix} a_{11}b_{11} & a_{11}b_{12} & a_{12}b_{11} & a_{12}b_{12} \\ a_{11}b_{21} & a_{11}b_{22} & a_{12}b_{12} & a_{12}b_{22} \\ a_{21}b_{11} & a_{21}b_{12} & a_{22}b_{11} & a_{22}b_{12} \\ a_{21}b_{21} & a_{21}b_{22} & a_{22}b_{12} & a_{22}b_{22} \end{pmatrix} \tag{3.7}$$

It is worth noting that Kronecker products are often implicit and may be omitted for simplicity.

To see how an operator can be expressed in a larger space, let's consider a set of $N$ Hilbert spaces, each of dimension $n_i$. The $S_k$ component of the $i$-th spin in the total Kronecker space can be evaluated using

$$\hat{S}_{k,i} = I^{(n_1)} \otimes I^{(n_2)} \otimes \cdots \otimes I^{(n_{i-1})} \otimes \hat{S}_k \otimes I^{(n_{i+1})} \otimes \ldots I^{(n_N)}. \tag{3.8}$$

As an example, the $\hat{S}_z$ operators of a two-particle system of spins $s = 1/2$ and $s = 1$ is

$$\hat{S}_{z,1} = \hat{S}_z^{s=1/2} \otimes I^{(3)} = \frac{\hbar}{2}\begin{pmatrix} 1 & \\ & -1 \end{pmatrix} \otimes \begin{pmatrix} 1 & & \\ & 1 & \\ & & 1 \end{pmatrix} = \frac{\hbar}{2}\begin{pmatrix} 1 & & & & & \\ & 1 & & & & \\ & & 1 & & & \\ & & & -1 & & \\ & & & & -1 & \\ & & & & & -1 \end{pmatrix} \tag{3.9}$$

$$\hat{S}_{z,2} = I^{(2)} \otimes \hat{S}_z^{s=1} = \frac{\hbar}{2}\begin{pmatrix} 1 & \\ & 1 \end{pmatrix} \otimes \begin{pmatrix} 1 & & \\ & 0 & \\ & & -1 \end{pmatrix} = \begin{pmatrix} 1 & & & & & \\ & 0 & & & & \\ & & -1 & & & \\ & & & 1 & & \\ & & & & 0 & \\ & & & & & -1 \end{pmatrix} \tag{3.10}$$

The size $M$ of the Kronecker space combining all the subspace is $M = \prod_i n_i$. The exponential growth of the space as elements are added to a system is one of the key consequences of quantum mechanics. This explosion of the memory needed to store the complete operators and vectors of a quantum system, greatly limits the size of the systems that can be fully simulated. To circumvent these limitations, approximations are made, like the dynamical mean field theory and computational techniques are implemented such as the sparse matrices approach. This exponential growth also forms the basis of aspirations to use the laws of quantum mechanics for doing computations that could not be done classically.

### 3.1.1. ZEEMAN ENERGY

The first element that will be added to the spin Hamiltonian is the Zeeman energy. The Zeeman energy is responsible for splitting the spin's energy proportionally to its projection on an external magnetic field. The Zeeman energy takes the form

$$\hat{H}_{\text{zeeman}} = -\mu_B\left(\vec{L} + 2\vec{S}\right) \cdot \vec{B} \tag{3.11}$$

where $\hat{L}$ is the orbital momentum operator, $\hat{S}$ the spin operator, $\mu_B$ is the permeability of free-space and $\vec{B}$ is the magnetic field.

In some circumstances, notably for a Fe atom on $Cu_2N$, it is more convenient to use an effective spin combining a partially quenched orbital momentum and electron spins.

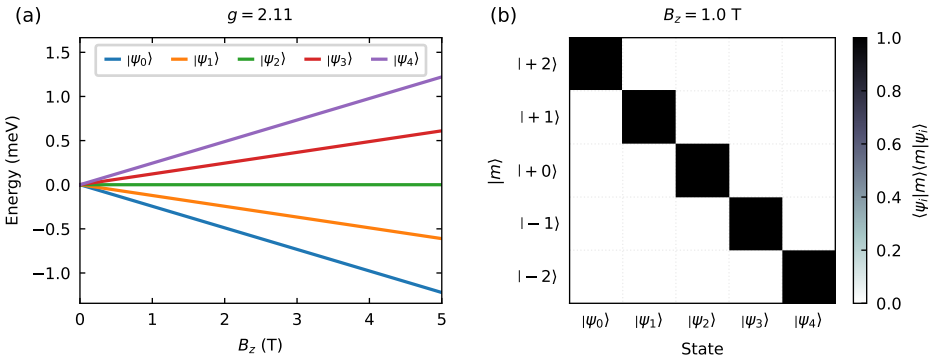


**Figure 3.1: Zeeman energy of a single Fe atom in a magnetic field with** $g = 2.11$. On the left is a plot of the dependence of the atom's state energies on the external magnetic field magnitude. On the right is the composition in absolute values of the atom's spin state composition in a basis aligned with the magnetic field.

The combined operator needs to be scaled by a constant, the Landé g-factor, that will depend on the specificity of the system. In the case of a Fe adatom on $Cu_2N$, an effective spin is $s = 2$ and a g-factor of $g = 2.11$[1–3] gives good agreement with the experimental observation. With this effective spin, the Hamiltonian takes the form

$$\hat{H}_{\text{zeeman}} = -g\mu_B \vec{S} \cdot \vec{B} = -g\mu_B \left(\hat{S}_x B_x + \hat{S}_y B_y + \hat{S}_z B_z\right) \tag{3.12}$$

In Figure 3.1, the solution of Equation 3.11 under a variation of the magnetic field is shown. The consequence of the Zeeman effect is to split the energy of the spin states. The spins aligned with the external field will be favoured over counter-align and lower-magnitude spin and so the atom's ground state will be the $|+2\rangle$ state.

### 3.1.2. MAGNETIC ANISOTROPY

The atom is not floating in free space but is bound to a surface. This breaks the symmetry of the free atom and creates a favoured or distorted magnetic moment. One way to model this distortion of the magnetic moment is to use the anisotropy Hamiltonian defined as

$$\hat{H}_{\text{anisotropy}} = D\hat{S}_z^2 + E\left(\hat{S}_x^2 - \hat{S}_y^2\right) \tag{3.13}$$

where $D$ is the uniaxial anisotropy and $E$ is the transverse anisotropy. In this model, the orbital momentum is considered quenched, and only the combined spin momenta of the atom's unpaired electrons can change.

The coordinate system is adjusted so that the $|D|$ is maximal and that $E \geq 0$. With these conditions, the effect of the $D$ will be such that the states with the minimal $D|S|$, where $|S|$ is the magnitude of $\hat{S}_z$, will be of lowest energy. This means that the ground states of a $s = 2$ particle, like the Fe on $Cu_2N$, will be $|+2\rangle$ and $|-2\rangle$.

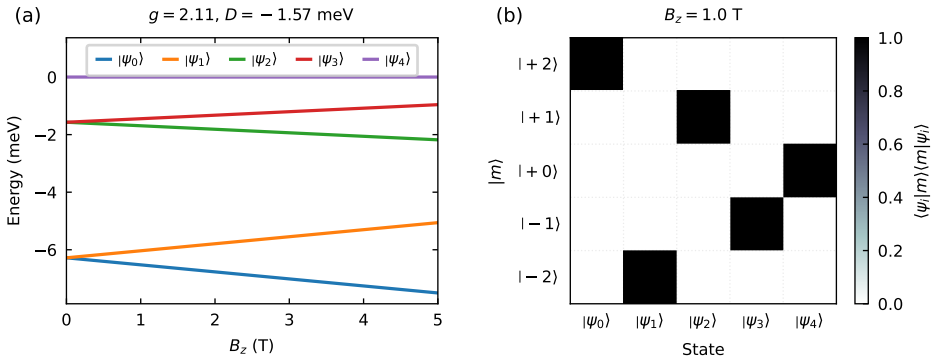


**Figure 3.2: Effect of the axial anisotropy parameter** $D$. On the left is a plot of the dependence of the atom's state energies under a change in the magnetic field. On the right is the composition in absolute values of the atom's spin state composition in a basis aligned with the magnetic field. The Landé g-factor is set to $g = 2.11$ and the axial anisotropy parameter to $D = -1.57$ meV.

Figure 3.2 and Figure 3.3 show the effect of the anisotropy on a single Fe on $Cu_2N$. The axial anisotropy $D$ is responsible for reordering the energies of the states by favouring the maximum absolute value of the spins. The ground state stays $|+2\rangle$, but in contrast to the free-floating atom, the first excitation is $|-2\rangle$. The difference in energy to the doublet of $|+1\rangle$ and $|-1\rangle$ states is also increased, creating, in practice, a binary system composed of $|+2\rangle$ and $|-2\rangle$. This observation will be important in chapter 5, where a chain of antiferromagnetically and ferromagnetically coupled atoms is studied.

The effect of the transverse anisotropy $E$ is that it hybridises the states. The mixing is a consequence of the non-commutation of the operator $S_z$ with $S_x$ and $S_y$. This mixing increases the probability of jumping between the states because of their overlap. The transverse anisotropy also creates a zero-field splitting, lifting the degeneracy of the ground state when no external magnetic field is present.

The values of the parameters $D$ and $E$ can be determined by fitting the IETS curves with the model[4]. In the case of a single Fe on $Cu_2N$, the value s $D = -1.57$ meV and $E = 0.31$ meV are able to reproduce good precision of the step positions in the $\mathrm{d}I/\mathrm{d}V$.

### 3.1.3. HEISENBERG COUPLING

If the spins are close enough, they can interact. This interaction can be of multiple origins like dipolar interaction, exchange interaction[5], superexchange interaction[6], DMI[7] or RKKY interaction[8] or a combination of interactions. Some interactions are mediated by the substrate and so will depend on the direction, distance and binding position of the two atoms[9].

It is possible to combine these interactions by using an effective term $J_{ij}$ characterising the binding energy between two adatoms. The effective interaction will be for each pair of adatoms in a specific configuration and can range from antiferromagnetic inter-

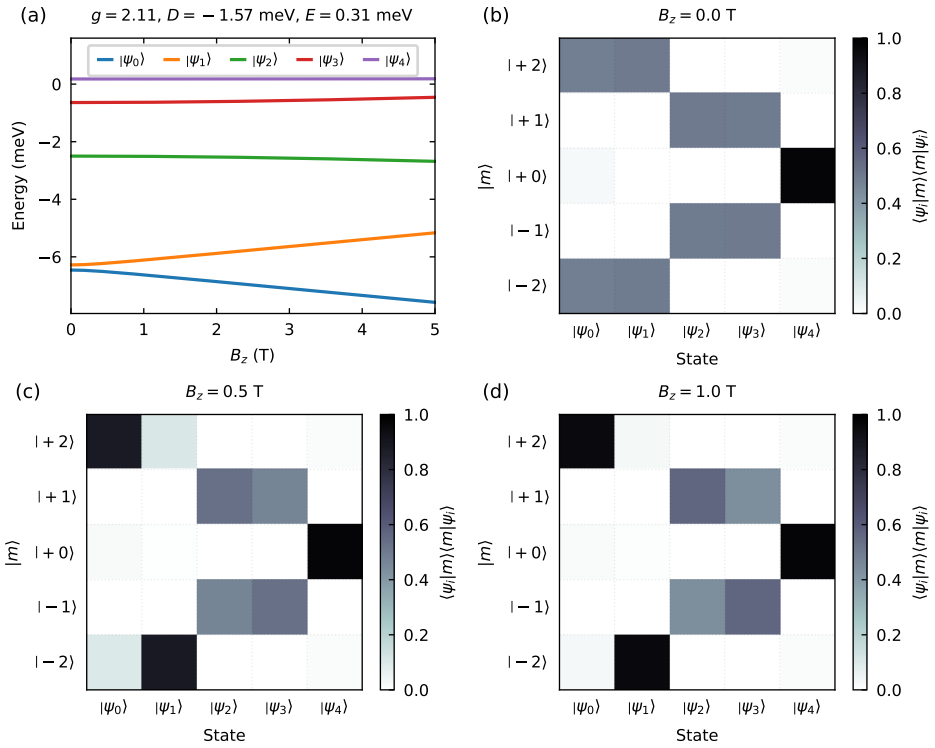


**Figure 3.3: Effect of the transverse anisotropy parameter** $E$. On the top-left is a plot of the dependence of the atom's state energies under a change in the magnetic field. On the top-right and bottom are the composition in absolute values of the atom's spin state composition in a basis aligned with the magnetic field. The Landé g-factor is set to $g = 2.11$, the axial anisotropy parameter to $D = -1.57$ meV and the transverse anisotropy to $E = 0.31$ meV.

action ($J_{ij} > 0$) to ferromagnetic interaction ($J_{ij} < 0$)[2]. The energy associated with this interaction is the Heisenberg Hamiltonian, defined as

$$\hat{H}_{\text{Heisenberg}} = \sum_{i>j} J_{ij} \vec{S}_i \cdot \vec{S}_j = \sum_{i>j} J_{ij} \left( \hat{S}_{x,i} \hat{S}_{x,j} + \hat{S}_{y,i} \hat{S}_{y,j} + \hat{S}_{z,i} \hat{S}_{z,j} \right). \tag{3.14}$$

This Hamiltonian take into account the interaction between all the pair of spin. However, in most cases, only a subset of the interactions will be worth considering as most interactions will be negligible due to the distance between the adatoms.



## 3.2. RATE EQUATION MODEL

As an STM measures the current flowing between a tip and a sample, the models developed should have as final results the current $I$ or, as it is often the value of interest and easier to measure precisely, the $\mathrm{d}I/\mathrm{d}V$ . The current can be calculated by evaluating the difference between the number of electrons flowing from the tip and the sample and those flowing from the sample to the tip. In this approach, the current can be written as [10, 11]

$$I(V,t) = e \sum_{i,j} \left( r_{ij}^{t \to s} - r_{ij}^{s \to t} \right) n_i(t) + b_0 G_0 V \tag{3.15}$$

where $V$ is the bias voltage, the term $b_0 G_0 V$ accounts for tunnelling electrons that don't interact with the adatom, $b_0$ is the fraction of electrons not interacting with the adatom, $G_0$ the background conductance, $r_{ij}^{t \to s}$ and $r_{ij}^{s \to t}$ are the rates of tunnelling between the states $i$ and $j$ from the tip ($t$) to the sample ($s$) and from the sample to the tip, respectively and $n_i(t)$ is the time-dependant state population probabilities.

The term $b_0 G_0 V$ corresponds to the background elastic tunnelling current. From Equation 2.5, in the limit where the energies of the electrons are greatly smaller than the potential barrier ($V_0 >> E$), the transmitivity is proportional to the electron energies. This justifies using a simply proportional term like $b_0 G_0 V$ for the elastic tunnelling of electrons.

The state population probabilities $n_i$ are time-dependent. However, because the dynamics of the electrons are fast compared to the STM measurement, usually only the steady-state solution when $t \to \infty$ will be of interest.

To use Equation 3.15, two things need to be known: the states in which the electrons will tunnel inelastically and the tunnelling rates. The states in question are the states of the spin Hamiltonian derived in the previous section. A way to evaluate the rate $r_{ij}$ follows. The approach is based on work by Loth *et al.*[10, 12, 13], Rolf-Pissarczyk *el al.*[14], and Ternes[11].

### 3.2.1. PAULI MASTER EQUATION

The Pauli Master Equation[15] describes the time-evolution of the state probability distribution ($n_i$) of a quantum system. The equation assumes that the transitions between

the states are Markovian, *i.e.* the transition rates $r_{ij}$ are constant and that the probability distribution at each step depends only on the previous step. For a constant bias, temperature and position of the tip, the transition rates are constant and can be used with the Pauli Master Equation.

The equation can be understood as follows. For a moment $t$, the change in a state's population is the difference between the quantity that leaves that state and the quantity that enters that state. Mathematically, we can write the equation as

$$\frac{\mathrm{d}}{\mathrm{d}t} n_i(t) = \sum_j \left( r_{ji} n_j(t) - r_{ij} n_i(t) \right) \tag{3.16}$$

where $n_i(t)$ is the population probability of state $i$ at the moment $t$ and $r_{ij}$ is the transition rate between the state $i$ and $j$.

We can rewrite the series of equations using a matrix notation as

$$\frac{\mathrm{d}}{\mathrm{d}t} \vec{n}(t) = \begin{bmatrix} \sum_j r_{j,1} n_j - n_1 \sum_j r_{1,j} \\ \sum_j r_{j,2} n_j - n_2 \sum_j r_{2,j} \\ \vdots \\ \sum_j r_{j,N} n_j - n_N \sum_j r_{N,j} \end{bmatrix} = R^{\Sigma} \cdot \vec{n}(t) \tag{3.17}$$

where $\vec{n}(t)$ is the vector of $n_i(t)$ value and the matrix elements of $R^{\Sigma}$ are

$$R^{\Sigma}_{ij} = r_{ji} - \delta_{ij} \sum_k r_{i,k} \tag{3.18}$$

The set of differential equations in 3.16 can be solved by starting from an initial condition at $t_0$ and integrating to find the distribution at a time $t_1$. However, as stated above, the value of interest is the distribution of the steady-state solution when $t \to \infty$, noted $\vec{n}(t \to \infty) = \vec{n}$. This simplifies the problem that now consists of solving

$$\frac{\mathrm{d}}{\mathrm{d}t} \vec{n} = 0 = R^{\Sigma} \vec{n} \tag{3.19}$$

The vector $\vec{n}$ that satisfies Equation 3.19 is called the null space (or kernel) of $R^{\Sigma}$[16], and methods to find the null space are implemented in many numerical libraries[17–19].

It is interesting to note that the previous result is independent of the initial conditions of the system, *i.e.* $\vec{n}$ always converge to the same value, whatever the initial condition.

### 3.2.2. TRANSITION MATRIX

The transition matrix evaluates the transition intensity between an initial state and a final state of the combined system formed by the effective spin of the adatom and an electron. The transition matrix can also be interpreted as the overlap of the states after the interaction between the electron and the adatom spin. The electron can tunnel to the adatom from the tip or the electrons bath of the substrate and will tunnel back to

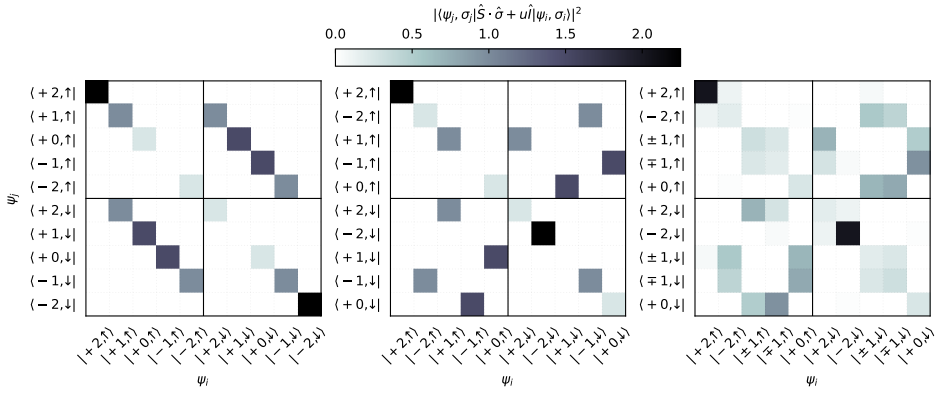


**Figure 3.4: Visual representation of the transition matrix**. Each subplot corresponds to a calculation of the transition matrix $Y$ of the spin Hamiltonian with different magnetic anisotropy parameters. All the calculations consider that a magnetic field of 1 tesla parallel with the uniaxial anisotropy ($D$) is present. The horizontal axes correspond to the states before the scattering event, and the vertical axes correspond to the state after the event. (left) Transition matrix without magnetic anisotropy. The state compositions are the same as Figure 3.1. (center) Transition matrix with a uniaxial anisotropy of $D = -1.57$ meV. The state compositions are the same as Figure 3.2. (right) Transition matrix with uniaxial anisotropy of $D = -1.57$ meV and a transverse anisotropy of $E = -0.31$ meV. The state compositions are the same as Figure 3.3.

either after the interaction. The interaction needs to keep the quantum numbers constant, notably to total spin. This will limit the possible transition between the states. The transition matrix elements can be evaluated as

$$Y_{ij} = \left|\left\langle\phi_j,\sigma_j\right|\vec{S}\cdot\vec{\sigma}+u\hat{I}\left|\phi_i,\sigma_i\right\rangle\right|^2 \tag{3.20}$$

where $\vec{S}$ is the effective spin operator of the adatom, $\vec{\sigma}$ is the spin operator of the tunnelling electron (a spin 1/2 operator), $i$ and $j$ are associated with the initial states and final states respectively, and $u$ accounts for spin-independent interactions such as potential scattering[12].

Example of calculations for Equation 3.20 where the $|\phi_i\rangle$ states are from the spin Hamiltonian described in section 3.1, are shown in Figure 3.4. The conservation of the spin can be clearly seen in Figure 3.4(a). In this case, only the Zeeman energy is active, and the states are ordered relative to their spin value. When the electron state is $|+1/2\rangle$, only transitions between states that increase the spin value of the adatom of +1 or keep it unchanged are permitted. If the adatom's spin value changes, the electron's spin also changes. A similar observation can be made when the spin of the electron is $|-1/2\rangle$.

### 3.2.3. RATES

Multiple pathways exist for the electrons to interact with the adatoms. The electrons can tunnel from the tip to the sample and vis-versa ($t \to s$ and $s \to t$), but also from the sample and back to the sample ($s \to s$) or from the tip and back to the tip ($t \to t$). The

total rate between two states will be the sum of these different rates:

$$r_{ij} = r_{ij}^{t\to s} + r_{ij}^{s\to t} + r_{ij}^{s\to s} + r_{ij}^{t\to t}. \tag{3.21}$$

However, the process going from the tip and back to the tip ($t \to t$) will be neglected as the coupling between the tip and the sample is weak and will contribute minimally to the state density probability.



Using the transition matrix element from Equation 3.20, the probability of transition per unit of time between two states ($P_{ij}$) is

$$P_{ij}^{t\to s} = \frac{1}{P_0}\sum_{\sigma,\sigma'} Y\left(\phi_j,\sigma',\phi_i,\sigma\right)\left(\frac{1}{2}+\eta\sigma\right) \tag{3.22}$$

$$P_{ij}^{s\to t} = \frac{1}{P_0}\sum_{\sigma,\sigma'} Y\left(\phi_j,\sigma',\phi_i,\sigma\right)\left(\frac{1}{2}+\eta\sigma'\right) \tag{3.23}$$

$$P_{ij}^{s\to s} = \frac{1}{2P_0}\sum_{\sigma,\sigma'} Y\left(\phi_j,\sigma',\phi_i,\sigma\right) \tag{3.24}$$

where $P_0$ is a normalisation constant, the summation is on the all the combination of the spin values of the electron ($\pm 1/2$) for the input $\sigma$ and the output $\sigma'$ (so four terms in the sum), and $\eta$ is the polarisation of the current. The parameter $\eta$ allows the calculation to account for a spin-polarised current. $\eta$ characterises the imbalance in the proportion of spin up and down in the current and is defined as

$$\eta = \frac{\rho_\uparrow - \rho_\downarrow}{\rho_\uparrow + \rho_\downarrow} \tag{3.25}$$

where $\rho_\uparrow$ and $\rho_\downarrow$ are the up-polarised current and down-polarised current, respectively. A value of $\eta = 1$ means a fully positively polarised current ($|+1/2\rangle$), a value of $\eta = -1$ means a fully negatively polarised current ($|-1/2\rangle$), and $\eta = 0$ means a non-polarised current. The transition probability due to the $s \to s$ process is independent of the tip polarisation as the electron does not interact with the tip in this process.

As the electrons move between the two electrodes ($t$ and $s$), they must go from a filled state to an empty state. The distribution of the electron energy in the electrodes is considered to follow the Fermi-Dirac distribution, defined as

$$F(\epsilon) = \frac{1}{e^{\beta\epsilon}+1} \tag{3.26}$$

where $\beta = 1/k_B T$, $k_B$ is the Boltzmann constant and $T$ the temperature.

The rates can be calculated with

$$r_{ij}^{t\to s} = (1-b_0)\frac{G_0}{e^2}P_{ij}^{t\to s}\int_{-\infty}^{\infty} F(\epsilon - eV)\left(1-F\left(\epsilon - E_{ij}\right)\right)\mathrm{d}\epsilon \tag{3.27}$$

$$r_{ij}^{s\to t} = (1-b_0)\frac{G_0}{e^2}P_{ij}^{s\to t}\int_{-\infty}^{\infty} F(\epsilon + eV)\left(1-F\left(\epsilon - E_{ij}\right)\right)\mathrm{d}\epsilon \tag{3.28}$$

$$r_{ij}^{s\to s} = \frac{G_s}{e^2}P_{ij}^{s\to s}\int_{-\infty}^{\infty} F(\epsilon)\left(1-F\left(\epsilon - E_{ij}\right)\right)\mathrm{d}\epsilon \tag{3.29}$$

where $b_0$ is the fraction of elastic tunnelling, as defined previously. The integral can be evaluated analytically as

$$F_*(E_0, E_1) = \int_{-\infty}^{\infty} F(\epsilon - E_0)\,(1 - F(\epsilon - E_1))\mathrm{d}\epsilon = \begin{cases} \frac{E_1 - E_0}{e^{\beta(E_1 - E_0)} - 1}, & E_0 \neq E_1 \\ \beta^{-1}, & E_0 = E_1 \end{cases} \tag{3.30}$$

This analytic solution simplifies the numeral calculation to evaluate the rates as

$$r_{ij}^{t\to s} = \frac{(1 - b_0)}{e^2} P_{ij}^{t\to s} F_*\left(eV, E_{ij}\right) \tag{3.31}$$

$$r_{ij}^{s\to t} = \frac{(1 - b_0)}{e^2} P_{ij}^{s\to t} F_*\left(-eV, E_{ij}\right) \tag{3.32}$$

$$r_{ij}^{s\to s} = \frac{G_s}{e^2} P_{ij}^{s\to s} F_*\left(0, E_{ij}\right). \tag{3.33}$$

It is possible to calculate the current and compare it to an experiment measurement using these rates. The model depends on multiple parameters that need to be fitted. Some parameters are the same between multiple adatoms of the same type ($D$, $E$, $g$, $J_i j$ and $G_s$), some depend on the tip condition and distance ($b_0$, $P_0$, $\eta$, $G_0$), and some are experimental conditions ($T$).

## 3.3. WAVEFUNCTION MODELS

In chapter 6, we present the experimental observation of vacuum states confined by surface structure. To model those states, we solve the Schrödinger equation using a custom code implementation. The theoretical implication is discussed in this section.

### 3.3.1. SOLVING THE SCHRÖDINGER EQUATION

The time-independent Schrödinger equation can be written as

$$\hat{H}\,|\Psi\rangle = E\,|\Psi\rangle \tag{3.34}$$

Simple in form, this equation can be complex to solve depending on the definition of the Hamiltonian $\hat{H}$.

The Hamiltonian can be decomposed as the sum of two parts: a kinetic part ($\hat{T}$) and a potential part ($\hat{V}$). We are interested in the behaviour of a single electron under the influence of an electric field, so the potential will not include an electron-electron or electron-proton interaction term. More precisely, the atoms in the system will be modelled using an electric potential. The definition of the electric potential inside the solid and in the vacuum are discussed in section 3.4 and subsection 3.4.2. The quantum mechanic kinetic energy of an electron takes the form

$$\hat{T} = \frac{-\hbar^2 \nabla^2}{2m_e} \tag{3.35}$$

In order to solve the Schrödinger equation for a single electron in an arbitrary potential, we implement a variational method using a basis of shifted Gaussian functions[20]. The limited spatial extent of the Gaussian function allows the resolution of a spatially limited wave function without the problem of boundaries and periodic conditions, as opposed to a plane-wave basis or power series.

The variational principle is the demonstration that for an arbitrary normalised trial function $|\Psi\rangle$ the ground state energy $E_0$ of a quantum system will respect

$$E_0 \leq \langle\Psi|\hat{H}|\Psi\rangle \tag{3.36}$$

where $\hat{H}$ is the Hamiltonian of the system and $E_0$ its ground state energy. The equality will be true only if $|\Psi\rangle$ is a valid wavefunction of the system. This principle is used in many quantum calculations, notably in density functional theory (DFT), where the trial function is iteratively minimised to obtain an approximated wave function. Here, we use the Ritz method to express the trial function on a function basis and solve the resulting eigenvalue problem.

Using a basis function set, we can write $|\Psi\rangle$ as

$$|\Psi\rangle = \sum_{k}^{N_s} c_k \left|\phi_k\right\rangle \tag{3.37}$$

To be able to map an arbitrary wave function in an n-dimensional space this set should have a limit $N_s = \infty$, but in practice, the summation need to be cut off at some point and the size of the basis function set will be finite. The number of functions in the set will be one of the factors affecting the precision of the approximation.

Using this basis with the variational principle (Equation 3.36)

$$\epsilon = \frac{\sum_{k,i}^{N_s} c_k^* c_i \left\langle\phi_j\right|\hat{H}\left|\phi_i\right\rangle}{\sum_{k,i}^{N_s} c_k^* c_i \left\langle\phi_k|\phi_i\right\rangle} = \frac{\sum_{k,i}^{N_s} c_k^* c_i H_{ki}}{\sum_{k,i}^{N_s} c_k^* c_i O_{ki}} \tag{3.38}$$

where $\epsilon$ is the energy corresponding to the trial wave function $\Psi$ and $H_{ik}$ is the matrix elements of the Hamiltonian on the basis of the function set. The $O_{ik}$ correspond to the overlap of functions that are typically non-orthogonal.

The Ritz method uses the observation that around the minimum of $\epsilon = E_0$ an infinitesimal variation of one of the constant $c_k$ defining the trial function will not change the resulting energy. In other terms, near the exact wave function of the system, the first

derivative of Equation 3.38 relative to one of the $c_k$ will be zero, so that

$$\begin{aligned}
\frac{\partial \epsilon}{\partial c_k^*} = 0 &= \frac{\sum_i^{N_s} c_i H_{ki}}{\sum_{k,i}^{N_s} c_k^* c_i O_{ki}} - \frac{\left(\sum_{k,i}^{N_s} c_k^* c_i H_{ki}\right)\left(\sum_i^{N_s} c_i O_{ki}\right)}{\left(\sum_i^{N_s} c_k^* c_i O_{ki}\right)^2} \\
&= \sum_i^{N_s} c_i H_{ki} - \left(\frac{\sum_{k,i}^{N_s} c_k^* c_i H_{ki}}{\sum_{k,i}^{N_s} c_k^* c_i O_{ki}}\right) \sum_i^{N_s} c_i O_{ki} \\
&= \sum_i^{N_s} c_i H_{ki} - \epsilon \sum_i^{N_s} c_i O_{ki} \\
\frac{\partial \epsilon}{\partial c_k^*} = 0 &= \sum_i^{N_s} c_i (H_{ki} - \epsilon O_{ki})
\end{aligned} \tag{3.39}$$

The last equation is an eigenvalues problem where the $\epsilon_i$ are the system's ground states and excitation energies. The eigenvectors are the $c_k$ that approximate the wave function in the basis function set for the corresponding eigenvalue.

The basis function set used in the code are $N$-dimensional isotropic Gaussian functions. They are defined as

$$\phi_i(\vec{r}) = \left(\frac{2\nu}{\pi}\right)^{N/4} \mathrm{e}^{-\nu(\vec{r}-\vec{\mu}_i)^2} \tag{3.40}$$

where $\nu = 1/2\sigma^2$ is the half inverse variance (and used to simplify the notation) and $\vec{\mu}_i$ is the position of the centre of the Gaussian $i$. The normalization factor before the exponential was chosen so that $\langle \phi_i | \phi_i \rangle = 1$. The value of this normalization constant does not impact the calculated eigenvalues and wave functions other than ensuring that there is no arithmetic underflow or overflow during the calculation.

To alleviate some of the numerical calculation, it is possible to solve for this specific basis some parts of Equation 3.39 analytically. This reduces drastically the computational work needed.

The function overlap is

$$O_{ij} = \langle \phi_i | \phi_j \rangle = \left(\frac{2\nu}{\pi}\right)^{N/2} \int_{-\infty}^{\infty} \mathrm{e}^{-\nu(\vec{r}-\vec{\mu}_i)^2 - \nu(\vec{r}-\vec{\mu}_j)^2} \, \mathrm{d}\vec{r}$$

$$O_{ij} = \mathrm{e}^{-\frac{\nu}{2}(\vec{\mu}_i - \vec{\mu}_j)^2} \tag{3.41}$$

And the kinetic operator is

$$T_{ij} = \langle \phi_i | \hat{T} | \phi_j \rangle = \left(\frac{2\nu}{\pi}\right)^{N/2} \int_{-\infty}^{\infty} \mathrm{e}^{-\nu(\vec{r}-\vec{\mu}_i)^2} \frac{-\hbar^2}{2m} \nabla^2 \left(\mathrm{e}^{-\nu(\vec{r}-\vec{\mu}_j)^2}\right) \mathrm{d}\vec{r}$$

$$T_{ij} = \left(\frac{-\hbar^2}{2m}\right) v^2 \left(\mu_i - \mu_j\right)^2 O_{ij} \tag{3.42}$$

That leaves only the potential terms to calculate by numerically integrating

$$V_{ij} = \langle \phi_i | V | \phi_j \rangle = \left(\frac{2v}{\pi}\right)^{N/2} \int_{-\infty}^{\infty} V(\vec{r})\, \mathrm{e}^{-v(\vec{r}-\vec{\mu}_i)^2 - v(\vec{r}-\vec{\mu}_j)^2}\, \mathrm{d}\vec{r} \tag{3.43}$$

assuming that the potential depends only on the position $\vec{r}$, an assumption that will be respected in our calculations.https://www.overleaf.com/project/5d887bb11d557100017c8aea

The code was written in the Julia language[21], and the code is available at `github.com/JGobeil/Schrod`.

## 3.4. IMAGE POTENTIAL STATE MODELS

In order to quantitatively understand tunnelling spectroscopy data acquired over the confined FER states, we used multiple numerical methods to model and analyse the data. We wrote code that allows us to solve the time-independent Schrödinger equation in multiple dimensions for an arbitrary potential. A quick introduction to the theory implemented in the software is presented in subsection 3.3.1, the 1D models in section 3.4 and the 2D models in subsection 3.4.2.

We model the confining potential in two parts the out-of-plane with a 1D potential and the in-plane confinement with a 2D potential. The out-of-plane confinement using the potential shown in Figure 2.5. The potential is composed of three parts: a nearly-free electron model for the sample potential[22, 23]; a plate-plate model for the electric potential between the tip and the sample[24]; and the exact classical model for the image potential[25].

For the in-plane confinement, we take three approaches for modelling the confinement potential: the infinite, the finite and the slanted potential well models. The infinite well solutions are evaluated analytically, and the two others solution are obtained using numerical calculations. The resulting probability distributions ($|\Psi^2|$) are shown in Figure 6.9, with the corresponding calculated energies shown in Figure 6.8. In both models, the bottom of the potential well is situated at 4.73 eV, corresponding to the energy of the first FER on a bare Cu(100) surface[26]. The height of the finite well is taken to be 5.61 eV, corresponding to the next FER observed on the chlorine. The spatial character (number and orientation of nodal planes) of the measured eigenstates is well reproduced by both models, though the spatial extent of the states is underestimated in the calculations.

### 3.4.1. 1D MODELS

#### IPS WITHOUT TIP

For the purpose of IPS modelling, the potential above a metallic surface, without a tip, is typically modelled using the image potential. On a metallic surface, this corresponds to

the Coulomb attraction of the electron to its image charge and take the form

$$V(z) = -\frac{1}{4(z-z_i)}, \quad z > z_i. \tag{3.44}$$

where $z$ is the position along a line perpendicular to the surface with $z = 0$ corresponding to the atomic plane of the surface and $z < 0$ is inside the surface. $z_i$ is the position of the image plane and will be discussed shortly. The image potential reach asymptotically the vacuum level and the IPS associated with this potential creates a Rydberg series (see Equation 2.13).



In the case of a dielectric the equation needs a slight modification and become[27, 28]

$$V(z) = -\left(\frac{\epsilon-1}{\epsilon+1}\right)\frac{1}{4(z-z_i)}, \quad z > z_i. \tag{3.45}$$

The potential inside the surface can be modelled in different ways, for example, by putting a potential wall at the surface[29] or using a nearly-free-electron (NFE) model[30, 31]. In this work, we use an NFE model to reproduce the appropriate projected bandgap at the surface. An example of the resulting potentials is shown in Figure 2.5. The NFE values used for the calculation were taken from Chulkov[23].

The potentials in Equation 3.44 and Equation 3.45 were used to quantitatively explain the observation of IPS resonance with LEED[32–34], inverse photoemission[29], time-resolved coherent photoelectron spectroscopy[35] and time-resolved two-photon photo-emission[36], to name a few. It is also used in most theoretical works[27, 28, 37, 38]. However, this potential includes an abrupt change leading to an infinite first derivative and thus, an infinite force. This kind of potential is not physically possible. To circumvent that, corrections were proposed to this potential to allow a smooth transition from the image potential to the crystal potential. Notably, the Jones-Jennings-Jepsen (JJJ) potential[39] use an exponential function to create a smooth transition from the bulk to the image potential of the surface. Subsequently, this approach was also applied to a tip-sample interface[25, 40].

### IMAGE PLANE

When trying to model the potential near a surface, estimating where the surface ends and the vacuum begins is difficult. Because of the delocalised nature of the electron wavefunctions, the surface position is not easily defined, and multiple factors can play a role.

One factor is when considering the truncated solid model, where the distance between the atomic planes is the same for the surface as for inside the bulk. This model needs some corrections to simulate the surface dynamics correctly. Because of the differences in the neighbouring atoms and bounding at the surface compared to the bulk, the inter-plane distance will be different between the last and second last planes compared to the planes in the solid bulk. This effect is hard to measure experimentally, and few results are available[41].

Another consequence of the surface different neighbouring is that the distribution and density of the electrons is different at the surface than inside the bulk. The Shockley and the Tamm states are direct consequences of this difference. At the surface, the cloud of electrons extends outside of the surface and affects the surface's effective position.

The image plane[31, 38] tries to encompass those effects by defining an effective position where the vacuum potential, usually the image potential, begins. The image plane position is defined relative to the surface plane. A typical value for the image place of a Cu(100) surface is 115 pm[42].



The surface plane, located at $z = z_0$, is defined as the position of the surface atoms in the truncated solid model, *i.e.* the plane crossing the center of the last layer of atoms.

### TIP-SAMPLE ELECTRIC POTENTIAL

The potential between the tip and the sample can be separated into two parts: the electric potential (or tip field) and the image potential.

The electric potential is caused by the difference in the Fermi energy between the two metals and the voltage bias applied between them. The shape of the potential inside the vacuum will depend on the geometry of the two electrodes (the tip and the sample) forming the STM junction. The electric potential between two nearby capacitors is a well know problem in electrostatics, and we can use the know methods and results to model it[24, 43].

We will introduce two typical approaches used to model the tip: the flat tip or plate-plate model; and the spherical tip.

A simple model to describe the electric potential in the vacuum between the tip and a metallic surface is two infinite parallel plates. This approximation was used in multiple publications to model the vacuum potential[44–46]. Such potential can be written as

$$V_{pp}(z) = -\frac{z}{s}\left(V_a - \phi_s + \phi_t\right) \tag{3.46}$$

where $V_a$ is the applied bias voltage, $s$ is the distance between the tip and the sample and $\phi_s$ ($\phi_t$) is the work function of the sample (tip). The $z = 0$ position is defined as the position of the atom at the apex of the tip and $z = s$ as the plane's position of the first atoms of the sample. In other words, the tip is a $z < 0$, the sample at $z > s$, and the vacuum in between. This model has the advantage to be simple and having only one unknown parameter, the tip-sample distance. This model is used in Figure 2.5.

Realistically, the tip cannot be flat. There is to be a protuberance and, because of the exponential dependence of the tunnelling current on the size of the gap, the point that sticks out will dominate the tunnelling current. A way to refine the model is to consider the tip to be a sphere. This model was used with success[25, 45, 47, 48] and can provide a description closer to the observation than the flat tip model, but at the cost of one more fitting parameter, *i.e.* the radius of the tip.

The image method can be used to evaluate the electric potential in the vacuum between a sphere and a surface. The approach requires to sum an infinite series of charges

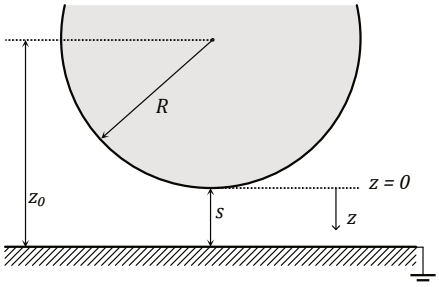


**Figure 3.5: Spherical tip model.**



inside the sphere and anti-charge inside the surface[49, 50]. By doing so, the electric potential in the vacuum along a line perpendicular to the surface and crossing the center of the sphere can be written as

$$V_{sp}(z) = R\big(V_a - \phi_s + \phi_t\big) \sum_{i=0}^{\infty} \left( \frac{\xi_i}{z - z_i} - \frac{\xi_i}{z + z_i} \right) \tag{3.47}$$

$$z_0 = s + R, \qquad z_i = z_0 - \frac{R^2}{z_0 + z_{i-1}} \tag{3.48a}$$

$$\xi_0 = 1, \qquad \xi_i = \frac{R\xi_{i-1}}{z_0 + z_{i-i}} \tag{3.48b}$$

Even if the spherical tip model is a better model, this is at the cost of one more parameter to set, and often the increased precision is negligible, especially at a close distance. The difference between a flat tip model and a spherical tip becomes significant only when the tip radius is similar to the distance between the tip and the sample ($R \approx s$).

### TIP-SAMPLE IMAGE POTENTIAL

The image potential is created by the presence of an electron near a surface. The electron charge induces a positive image charge (*i.e.* , a hole) in the electronics charge of the surface, attracting the electron that created it. In a tip-sample interface, both the sample and the tip will exhibit an image potential. When the tip is brought in close range to the surface, the two image potentials will combine to create a more complex potential.

A first approximation is obtained by simply summing the two image potentials.

$$V_{\text{im}}(z) = -\frac{s}{4z(s-z)} \tag{3.49}$$

where $s$ is the distance between the tip and the sample. This potential is called the first image charge[25].

The previous equation only considers the first image charge, hence the name, and ignore that each image charge will induce another image charge in the other plate. This

creates an infinite sum of image charges in the two plates, and the resulting potential is named the exact classical image[25].

$$V_{\text{im}}(z) = -\frac{1}{4}\left(\frac{1}{z}+\frac{1}{s-z}\right)+\frac{1}{4s}\left[\sum_{n=1}^{\infty}\left(\frac{2}{n}-\frac{1}{n+z/s}\right)-\sum_{n=2}^{\infty}\left(\frac{1}{n-z/s}\right)\right] \tag{3.50}$$

$$= -\frac{s}{4z(s-z)}+\frac{1}{4s}\left[2\gamma+\Psi\left(1+\frac{z}{s}\right)\Psi\left(2-\frac{z}{s}\right)\right] \tag{3.51}$$

where $s$ is the distance between the tip and the sample, $\gamma$ is the Euler number, and $\Psi(x)$ is the digamma function. This equation is quite complex, and an approximation was proposed by Simmon[24] with

$$V_{\text{im}}(z) = -1.15\ln 2\frac{s}{4z(s-z)} \tag{3.52}$$

where $s$ is the distance between the tip and the sample.

Finally, let us mention that the Jones-Jennings-Jepson (JJJ) potential[39] for a surface was adapted by Pitarke *et al.*[25] for an STM junction. The potential uses exponential functions to transition between the surface and image potential to create a smooth transition, including the first derivative. This approach introduces two free parameters characterising the length of the transition. The correction on the calculated energies is expected to be minimal compared to Equation 3.51.

### 3.4.2. IMAGE POTENTIAL STATE: 2D MODELS

Typically with FER, the electrons are trapped vertically but can move freely perpendicularly to the surface before diffusing into the substrate. Consequently, they do not show any quantisation of their energy due to in-plane confinement. In our case, the electrons are also trapped in-plane and will show quantisation in-plane. The two quantisations can be treated separately, and their energies summed. We can write the energy of the FER as

$$E_{n_x n_y n_z} = E_{n_z} + E_{n_x n_y} \tag{3.53}$$

where $E_{n_x n_y n_z}$ are the measured energies, $E_{n_x n_y}$ are the energy associated with the in-plane confinement and $E_{n_z}$ with the vertical confinement. We measure multiple IPS for the same vertical mode ($n_z$) due to the different $n_x n_y$ modes, but as the tip height changes to maintain the constant current, the energy of the vertical mode will change as the potential changes. When considered alone, the in-plane confinement is independent of the tip-sample distance. However, its energy is affected indirectly by the change in the vertical IPS energy. In other words, we should write $E_{n_z} \rightarrow E_{n_z}(z)$ and

$$E_{n_x n_y n_z}(z) = E_{n_x n_y} + E_{n_z}(z) \tag{3.54}$$

However, looking at Figure 6.10 we can see that after the modes $(n,1)$ the tip-sample distance stays mostly the same, and so we can consider that Equation 3.53 is a good approximation of the energies.

Three simple models of in-plane confinement are considered to calculate energy excitation: infinite box, finite box and slanted box model. For all the models, the potential is centred at $(x, y) = (0,0)$ and the degenerated states were grouped using a hierarchical clustering algorithm with a grouping tolerance of 0.05V.

### INFINITE BOX MODEL

The infinite box model is the textbook analytical solution of the Schrödinger equation of a particle inside a 2D box with infinite walls. Inside the box, the potential is constant at a value $V_{min}$ and outside, the potential is infinite ($V_{max} = \infty$). The box is characterised by its length in the $x$ and $y$ direction, named respectively $L_x$ and $L_y$, and by its potential at the minimum $V_{min}$. Outside the box, the wave function is null. Inside the box, the spatial part of the wave function takes the form

$$\Psi_{n_x,n_y}(x,y) = \sqrt{\frac{4}{L_x L_y}} \sin\left[\frac{n_x \pi}{L_x}\left(x - \frac{L_x}{2}\right)\right] \sin\left[\frac{n_y \pi}{L_y}\left(y - \frac{L_y}{2}\right)\right] \tag{3.55}$$

The solutions are standing waves inside the box parametrized by their modes $n_x$ and $n_y$, where $n_i = 1,2,3,\ldots$. The associated energies of an electron inside the box are

$$E_{n_x,n_y} = \frac{\pi^2}{2}\left(\frac{n_x^2}{L_x^2} + \frac{n_y^2}{L_y^2}\right) + V_{min} \tag{3.56}$$

where $m_e$ is the mass of the electron.

### FINITE BOX MODEL

The finite box removes the infinity wall and gives them a finite value of $V_{max}$. This allows some part of the wave function to leak outside the limit of the box. To find the wave function of such a potential, we used the Schrödinger solver mentioned previously.

As for the infinite box, the potential is parametrised by its dimension $L_x$, $L_y$, its energy of the bottom $V_{min}$, but with the additonal parameter of the energy at the top $V_{max}$.

$$V(x,y) = \begin{cases} V_{max} & \text{for } |x| > L_x \text{ or } |y| > L_y \\ V_{min} & \text{for } |x| \leq L_x \text{ and } |y| \leq L_y \end{cases} \tag{3.57}$$

### SLANTED BOX MODEL

The slanted box model further extends the finite box model by replacing the step function at the edge with a slope. The potential is defined, in addition to the $V_{min}$ and $V_{max}$ values, by its outside edge lengths $L_x$ and $L_y$, and its inside side length $l_x$ and $l_y$. Between the inside and outside edges, the potential is linear. This potential can be written

as

$$V(x,y) = \begin{cases} V_{max} & \text{for } |x| > L_x \text{ or } |y| > L_y \\ V_{min} & \text{for } |x| \leq l_x \text{ and } |y| \leq l_y \\ V_{min} + 2\frac{V_{max}-V_{min}}{L_x-l_x}(|x| - l_x/2) & \text{for } |x| > |y| \\ V_{min} + 2\frac{V_{max}-V_{min}}{L_y-l_y}(|y| - l_y/2) & \text{for } |y| \leq |x| \end{cases} \tag{3.58}$$



The results from the different models are presented in chapter 6.

## REFERENCES


[1] C. F. Hirjibehedin, C.-Y. Lin, A. F. Otte, M. Ternes, C. P. Lutz, B. A. Jones, and A. J. Heinrich, *Large Magnetic Anisotropy of a Single Atomic Spin Embedded in a Surface Molecular Network,* Science **317**, 1199 (2007).

[2] A. Spinelli, M. Gerrits, R. Toskovic, B. Bryant, M. Ternes, and A. F. Otte, *Exploring the phase diagram of the two-impurity Kondo problem,* Nature Communications **6**, 10046 (2015).

[3] R. Toskovic, R. van den Berg, A. Spinelli, I. S. Eliens, B. van den Toorn, B. Bryant, J.-S. Caux, and A. F. Otte, *Atomic spin-chain realization of a model for quantum criticality,* Nat Phys **12**, 656 (2016).

[4] B. Bryant, A. Spinelli, J. J. T. Wagenaar, M. Gerrits, and A. F. Otte, *Local Control of Single Atom Magnetocrystalline Anisotropy,* Phys. Rev. Lett. **111**, 127203 (2013).

[5] P. Wahl, P. Simon, L. Diekhöner, V. S. Stepanyuk, P. Bruno, M. A. Schneider, and K. Kern, *Exchange Interaction between Single Magnetic Adatoms,* Phys. Rev. Lett. **98**, 056601 (2007).

[6] D.-J. Choi, R. Robles, S. Yan, J. A. Burgess, S. Rolf-Pissarczyk, J.-P. Gauyacq, N. Lorente, M. Ternes, and S. Loth, *Building complex Kondo impurities by manipulating entangled spin chains,* Nano Lett. (2017), 10.1021/acs.nanolett.7b02882.

[7] J. Bouaziz, M. d. S. Dias, A. Ziane, M. Benakki, S. Blügel, and S. Lounis, *Chiral magnetism of magnetic adatoms generated by Rashba electrons,* New J. Phys. **19**, 023010 (2017).

[8] L. Zhou, J. Wiebe, S. Lounis, E. Vedmedenko, F. Meier, S. Blügel, P. H. Dederichs, and R. Wiesendanger, *Strength and directionality of surface Ruderman–Kittel–Kasuya–Yosida interaction mapped on the atomic scale,* Nature Physics **6**, 187 (2010).

[9] A. Spinelli, *Quantum magnetism through atomic assembly,* (2015).

[10] S. Loth, K. von Bergmann, M. Ternes, A. F. Otte, C. P. Lutz, and A. J. Heinrich, *Controlling the state of quantum spins with electric currents,* Nat Phys **6**, 340 (2010).

[11] M. Ternes, *Spin excitations and correlations in scanning tunneling spectroscopy,* New J. Phys. **17**, 063016 (2015).

[12] S. Loth, C. P. Lutz, and A. J. Heinrich, *Spin-polarized spin excitation spectroscopy,* New J. Phys. **12**, 125021 (2010).

[13] S. Loth, S. Baumann, C. P. Lutz, D. M. Eigler, and A. J. Heinrich, *Bistability in Atomic-Scale Antiferromagnets,* Science **335**, 196 (2012).

[14] S. Rolf-Pissarczyk, S. Yan, L. Malavolti, J. A. J. Burgess, G. McMurtrie, and S. Loth, *Dynamical Negative Differential Resistance in Antiferromagnetically Coupled Few-Atom Spin Chains,* Phys. Rev. Lett. **119**, 217201 (2017).

[15] H.-P. Breuer and F. Petruccione, *Quantum Master Equations,* in *The Theory of Open Quantum Systems*, edited by H.-P. Breuer and F. Petruccione (Oxford University Press, 2007) p. 0.

[16] E. W. Weisstein, *Null Space,* https://mathworld.wolfram.com/ (2023).

[17] *Null space of matrix,* https://www.mathworks.com/help/matlab/ref/null.html (2023).

[18] *NullSpace,* https://reference.wolfram.com/language/ref/NullSpace.html (2023).

[19] *Scipy.linalg.null_space,* https://docs.scipy.org/doc/ (2023).

[20] K. Varga and J. A. Driscoll, *Computational Nanoscience: Applications for Molecules, Clusters, and Solids* (Cambridge University Press, 2011).

[21] J. Bezanson, A. Edelman, S. Karpinski, and V. B. Shah, *Julia: A Fresh Approach to Numerical Computing,* SIAM Rev. **59**, 65 (2017).

[22] E. T. Goodwin, *Electronic states at the surfaces of crystals: I. The approximation of nearly free electrons,* Mathematical Proceedings of the Cambridge Philosophical Society **35**, 205 (1939).

[23] E. V. Chulkov, V. M. Silkin, and P. M. Echenique, *Image potential states on metal surfaces: Binding energies and wave functions,* Surface Science **437**, 330 (1999).

[24] J. G. Simmons, *Potential Barriers and Emission-Limited Current Flow Between Closely Spaced Parallel Metal Electrodes,* Journal of Applied Physics **35**, 2472 (1964).

[25] J. M. Pitarke, F. Flores, and P. M. Echenique, *Tunneling spectroscopy: Surface geometry and interface potential effects,* Surface Science **234**, 1 (1990).

[26] P. Wahl, M. A. Schneider, L. Diekhöner, R. Vogelgesang, and K. Kern, *Quantum Coherence of Image-Potential States,* Phys. Rev. Lett. **91**, 106802 (2003).

[27] M. W. Cole, *Electronic Surface States of a Dielectric Film on a Metal Substrate,* Phys. Rev. B **3**, 4418 (1971).

[28] P. M. Echenique and J. B. Pendry, *The existence and detection of Rydberg states at surfaces,* Journal of Physics C: Solid State Physics **11**, 2065 (1978).

[29] D. Straub and F. J. Himpsel, *Identification of Image-Potential Surface States on Metals,* Phys. Rev. Lett. **52**, 1922 (1984).

[30] N. V. Smith, *Phase analysis of image states and surface states associated with nearly-free-electron band gaps,* Phys. Rev. B **32**, 3549 (1985).

[31] M. Ortuo and P. M. Echenique, *Phase shifts, image planes, and surface states at metal surfaces,* Phys. Rev. B **34**, 5199 (1986).

[32] R. E. Dietz, E. G. McRae, and R. L. Campbell, *Saturation of the Image Potential Observed in Low-Energy Electron Reflection at Cu(001) Surface,* Phys. Rev. Lett. **45**, 1280 (1980).

[33] P. J. Jennings and R. O. Jones, *Surface barrier determination using spin-polarized LEED: W(001),* Solid State Communications **44**, 17 (1982).

[34] E. G. McRae, *Electronic surface resonances of crystals,* Rev. Mod. Phys. **51**, 541 (1979).

[35] U. Höfer, I. L. Shumay, C. Reuß, U. Thomann, W. Wallauer, and T. Fauster, *Time-Resolved Coherent Photoelectron Spectroscopy of Quantized Electronic States on Metal Surfaces,* Science **277**, 1480 (1997).

[36] E. V. Chulkov, I. Sarría, V. M. Silkin, J. M. Pitarke, and P. M. Echenique, *Lifetimes of Image-Potential States on Copper Surfaces,* Phys. Rev. Lett. **80**, 4947 (1998).

[37] M. W. Cole and M. H. Cohen, *Image-Potential-Induced Surface Bands in Insulators,* Phys. Rev. Lett. **23**, 1238 (1969).

[38] N. D. Lang and W. Kohn, *Theory of Metal Surfaces: Induced Surface Charge and Image Potential,* Phys. Rev. B **7**, 3541 (1973).

[39] R. O. Jones, P. J. Jennings, and O. Jepsen, *Surface barrier in metals: A new model with application to W(001),* Phys. Rev. B **29**, 6474 (1984).

[40] J. M. Pitarke, P. M. Echenique, and F. Flores, *Apparent barrier height for tunneling electrons in STM,* Surface Science **217**, 267 (1989).

[41] H. Lüth, *Solid Surfaces, Interfaces and Thin Films*, Graduate Texts in Physics (Springer International Publishing, Cham, 2015).

[42] N. V. Smith, C. T. Chen, and M. Weinert, *Distance of the image plane from metal surfaces,* Phys. Rev. B **40**, 7565 (1989).

[43] D. J. Griffiths, *Introduction to Electrodynamics*, 4th ed. (Cambridge University Press, Cambridge, United Kingdom ; New York, NY, 2017).

[44] P. Ruffieux, K. Aït-Mansour, A. Bendounan, R. Fasel, L. Patthey, P. Gröning, and O. Gröning, *Mapping the Electronic Surface Potential of Nanostructured Surfaces,* Phys. Rev. Lett. **102**, 086807 (2009).

[45] S. Stepanow, A. Mugarza, G. Ceballos, P. Gambardella, I. Aldazabal, A. G. Borisov, and A. Arnau, *Localization, splitting, and mixing of field emission resonances induced by alkali metal clusters on Cu(100),* Phys. Rev. B **83**, 115101 (2011).

[46] J.-F. Ge, H. Zhang, Y. He, Z. Zhu, Y. C. Yam, P. Chen, and J. E. Hoffman, *Probing image potential states on the surface of the topological semimetal antimony,* Phys. Rev. B **101**, 035152 (2020).

[47] J. I. Pascual, C. Corriol, G. Ceballos, I. Aldazabal, H.-P. Rust, K. Horn, J. M. Pitarke, P. M. Echenique, and A. Arnau, *Role of the electric field in surface electron dynamics above the vacuum level,* Phys. Rev. B **75**, 165326 (2007).

[48] J. Martínez-Blanco, S. C. Erwin, K. Kanisawa, and S. Fölsch, *Energy splitting of image states induced by the surface potential corrugation of InAs(111)A,* Phys. Rev. B **92**, 115444 (2015).

[49] B. Techaumnat and T. Takuma, *Analysis of the electric field and force in an arrangement of a conducting sphere and a plane electrode with a dielectric barrier,* IEEE Transactions on Dielectrics and Electrical Insulation **13**, 336 (2006).

[50] F. F. Dall'Agnol and V. P. Mammana, *Solution for the electric potential distribution produced by sphere-plane electrodes using the method of images,* Rev. Bras. Ensino Fís. **31**, 3503.1 (2009).

# 4

# LARGE INSULATING NITRIDE ISLANDS ON $Cu_3Au$

*We present controlled growth of c(2×2)N islands on the (100) surface of $Cu_3Au$, which can be used as an insulating surface template for manipulation of magnetic adatoms. Compared to the commonly used Cu(100)/c(2×2)N surface, where island sizes do not exceed several nanometers due to strain limitation, the current system provides better lattice matching between metal and adsorption layer, allowing larger unstrained islands to be formed. We show that we can achieve island sizes ranging from tens to hundreds of nanometers, increasing the potential building area by a factor $10^3$. Initial manipulation attempts show no observable difference in adatom behaviour, either in manipulation or spectroscopy.*

Parts of this chapter have been published in Surface Science **679**, 202 (2019) [1].

## 4.1. INTRODUCTION

THE ability to position individual magnetic adatoms into a specific arrangement on a surface holds great potential for atomic scale studies of quantum magnetism [2]. A particularly successful template for the placement of transition metal atoms is the c(2×2) reconstruction of nitrogen on the Cu(100) crystal surface [3], which provides a self-terminated insulating monolayer, separating the atomic spins from the conduction electrons in the metal below [4]. Due to its covalent structure, the copper-nitride surface provides significant magneto-crystalline anisotropy [5] and allows for tunable spin-spin coupling between neighbouring atoms, both ferromagnetic and antiferromagnetic [6, 7]. The combination of these techniques has given rise to a range of seminal experiments, including the construction of a 96-atom magnetic byte [8], the observation of spin waves in a one-dimensional spin chain [9], and the atomically precise study of various highly entangled spin systems [10, 11].



As atom manipulation techniques become more reliable [12], the size of atomic structures is only limited by the maximum available continuous building area. In the case of copper-nitride, this limit is imposed by the nitrogen islands. Due to a 3% lattice mismatch between the adsorption layer and the underlying Cu(100) crystal, island sizes are strain-limited to ~ 5 nm × 5 nm — or, on saturated surfaces up to 20 nm× 20 nm [13] — hampering the assembly of any spin structure larger than that. Here, we present growth of nitride islands on a different metal substrate: the $Cu_3Au(100)$ surface. With a lattice constant $a = 0.375$ nm [14], its lattice much better matches the one of copper-nitride ($a = 0.372$ nm [15]) than the Cu(100) surface ($a = 0.359$ nm [16]) does. By properly tuning growth conditions, we can routinely grow islands ranging from tens to hundreds of nanometres across, vastly increasing the area on which spin structures can be assembled.

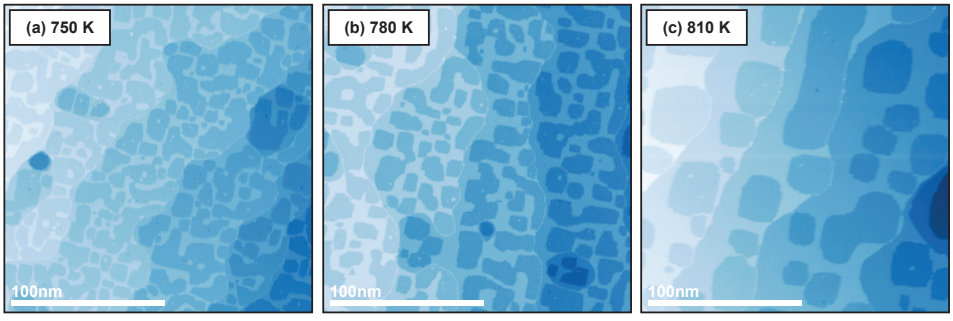


**Figure 4.1:** STM images of nitrogen islands on ordered $Cu_3Au(100)$ after 5 minutes of annealing at (a) 750 K (b) 780 K and (c) 810 K. The images were acquire at a temperature of 1.5 K with constant current at (a) 0.1 nA and 0.2 V, (b) 0.1 nA and 1 V and (c) 0.4 nA and 0.2 V. The nitrogen islands appear as darker areas surrounded by brighter areas, which are bare $Cu_3Au(100)$.

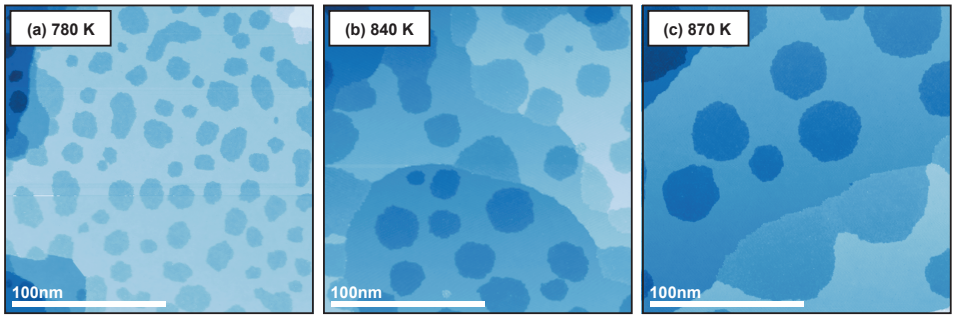


**Figure 4.2:** STM images of nitrogen islands on disordered $Cu_3Au(100)$ after 5 min of annealing at (a) 780 K (b) 840 K and (c) 870 K. The images were acquire at a temperature of 1.5 K with constant current at (a) 0.1 nA and 50 mV, (b) 0.2 nA and 100 mV and (c) 0.2 nA and 50 mV.



## 4.2. EXPERIMENTAL DETAILS

The experiments were performed in a scanning tunnelling microscope (STM) operating in ultra-high vacuum (UHV) and cryogenic conditions. During measurements the pressure was $<5 \times 10^{-10}$ mbar and the temperature was between 1.4 K and 1.5 K. Sample preparation was performed *in situ* in a UHV chamber connected to the STM, which has a base pressure of $<4 \times 10^{-10}$ mbar. The preparation chamber is equipped with standard sputtering and e-beam annealing equipment, and has inlets for pure argon and nitrogen (99.999%).

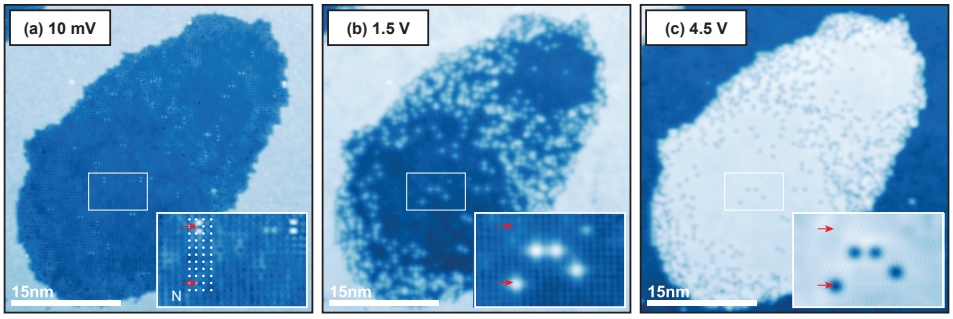


**Figure 4.3:** STM images of a nitrogen islands on disordered $Cu_3Au(100)$, scanned at a constant current of 0.5 nA and a bias of (a) 10 mV, (b) 1.5 V and (c) 4.5 V. The surface was annealed 5 min at 840 K after nitrogen sputtering. The insets are higher resolution scans of a section of the nitrogen island taken at identical measurement parameters. The corresponding area on the island is indicated by a white rectangle. For (a) and (b) the nitrogen islands are darker than the surrounding bare $Cu_3Au(100)$. This contrast is inverted for (c). In inset of (a), the white circles correspond to the nitrogen position in the CuN layer. To avoid clutter, copper positions, which are located in between nitrogen nearest neighbours, are omitted. The red arrows, repeated in all three insets, indicate the two types of defect described in the text.

### NOTE ON THE REPORTED TEMPERATURE

We monitor the sample temperature during annealing by means of a pyrometer. Due to stray radiation originating from the filament behind the sample, the actual temperature readout, while reliable, is overestimated. In order to approximate the real temperature of the sample during annealing, we record the cooling curves after turning off the filament, and extrapolate back.

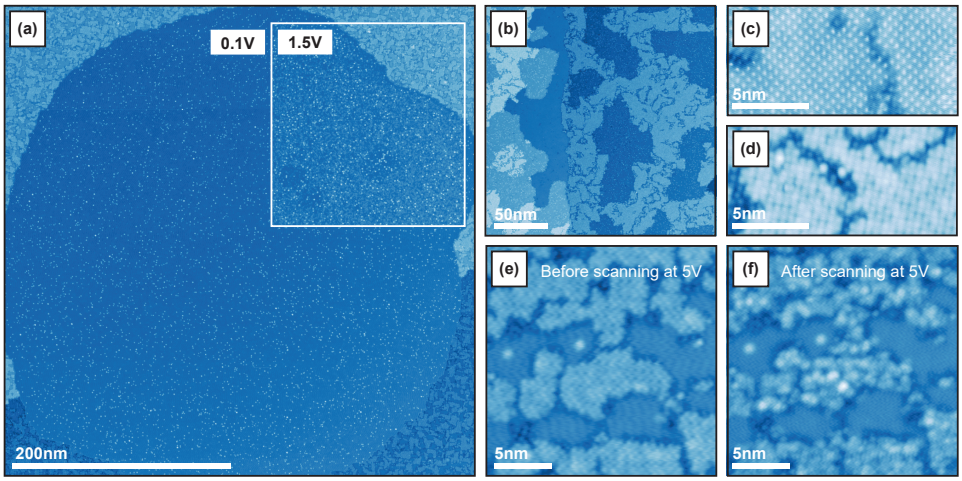


**Figure 4.4:** (a) Nitrogen island with an area of over 145 000 $nm^2$ with Fe adatoms evaporated onto it. (b-f) STM images of percolated areas. The sample was annealed for (a,e,f) 15 min in three steps at 810 K, 780 K and 750 K, (b) 20 min at 930 K and (c,d) 20 min at 870 K. The STM images were taken at (a) 0.2 nA and 100 mV (inset at 1.5 V), (b) 0.1 nA and 200 mV, (c) 0.1 nA and –20 mV, (d) 0.2 nA and 20 mV and (e, f) 0.1 nA and 100 mV. (e) and (f) show the same area before and after a scan of this area at 0.1 nA and 5 V.

We used a commercial $Cu_3Au$ crystal grown by *Surface Preparation Laboratory*, which was cut along the (100) plane with ~0.1° accuracy and polished to a roughness <0.03 µm. Prior to growing the nitride islands, the crystal was cleaned with multiple rounds of argon sputtering at kV 1 followed by annealing. This process was repeated until a clean surface with large plateaus was observed in STM images.

Nitrogen was subsequently implanted into the superficial layer by sputtering $N^+$ ions onto the surface. We used an sputtering voltage of 500 V and a current of 1 µA to achieve coverages in the order of a monolayer per minute. To favor the mobility of the implanted nitrogen atoms and repair possible damage to the surface, we follow the sputtering by an annealing process, leading to the formation of a c(2x2)N reconstruction on the $Cu_3Au(100)$ surface, similar to that reported for Cu(100) [3].

A $Cu_3Au$ crystal can be in two distinct phases: an ordered $L1_2$ phase [17, 18] upon annealing below a critical temperature $T_c = 663$ K [19–21], and a disordered phase above this temperature [22, 23]. While both phases have the FCC crystal structure, in the $L1_2$ phase the Au atoms are periodically distributed over the crystal whereas in the disordered phase they are not. The transition between the two phases is reversible [24, 25]:

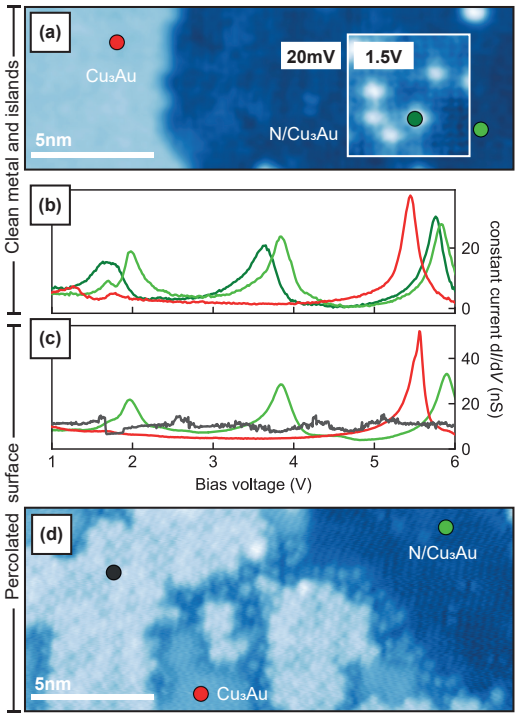


**Figure 4.5:** Tunneling specstroscopy measurements on regular and percolated areas. (a) STM image of a regular nitrogen island on disordered $Cu_3Au$. (b,c) $dI/dV$ spectroscopy measurements at constant current of (b) 1 nA and (c) 2 nA, taken at different positions on regular (b) and percolated (c) areas. Measurement locations are indicated with corresponding colours in (a) and (d). (d) STM image taken in a percolated area. STM scans were taken at 1.5 K and (a) 100 pA and 20 mV (inset at 1.2 V) and (d) 200 pA and 100 mV.

the crystal can be brought back into the $L1_2$ phase in a matter of hours by annealing at temperature near $T_c$ [24, 26]. The lattice constant of the disordered phase is slightly larger than the ordered $L1_2$ phase (0.3762 nm and 0.3754 nm respectively [27]).

## 4.3. RESULTS AND DISCUSSIONS

In a first series of experiments, a clean and ordered $L1_2$ sample was sputtered with nitrogen for 45 s at a current of 0.8 µA and an accelerating voltage of kV 0.5. The sample was then annealed for 5 min. The annealing temperature was kept at $T > T_c$ for only short periods of time, preserving the order in the bulk of the crystal. The surface is faster to both order and disorder when crossing the critical temperature, taking place on a broader temperature range [28, 29].

Figure 4.1 shows the effect of different annealing temperatures (as determined via the process described above) on the size and distribution of the islands. The resulting islands vary in size from 10 nm to 100 nm in their longest direction where the largest is-

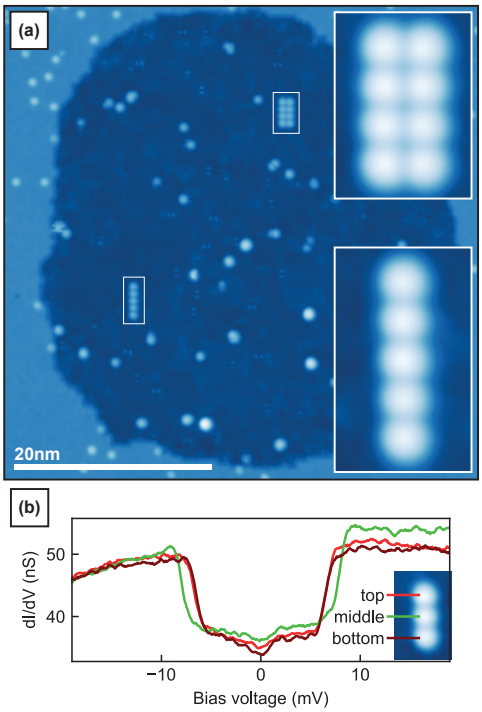


**Figure 4.6:** (a) 1 × 5 and 2 × 4 structures of Fe atoms similar to [8] assembled through vertical manipulation on a ~5000 $nm^2$ nitrogen island on $Cu_3Au$. (b) $dI/dV$ spectroscopy measurements taken on each of the atoms of a 1 × 3 Fe structure built on an island of similar size as in (a). Spectroscopy was taken in the center of each atom with initial settings of 800 pA and –20 mV. All structures were built on the same sample, which was annealed at 810 K, 780 K and 750 K for 5 min at each temperature. The STM images were taken at (a) 50 pA and 20 mV and (b) 200 pA and 50 mV.

lands appear only at a higher temperature. We observe a trend towards larger islands for higher temperatures. The edges of the island are mostly straight and oriented along the crystallographic axes (rotated between 5° and 10° clockwise relative to the image frame), as is observed on Cu(100). The island size is strongly increased with respect to the case of Cu(100) owing to a reduced strain accumulation, due to the better match in lattice parameters.

A second series of experiments was performed after a prolonged high temperate treatment of the crystal. We annealed the crystal for 15 hours at >900 K. This temperature is well above the critical temperature of 663 K, driving the crystal from the ordered $L1_2$ into a disordered FCC phase.

The disordered crystal was then prepared in a similar fashion as the ordered crystal. The amount of sputtered nitrogen is similar to the amount sputtered in the preparations in Figure 4.1 and the annealing time was kept unchanged at 5 min for each preparation. The resulting surfaces at different annealing temperatures can be seen in Figure 4.2.

The island sizes follow the same trend as on the ordered crystal, with islands ranging from 10 nm to 100 nm where larger islands are observed for higher temperatures. A major difference is found in the island geometry. In the ordered case the islands have mostly straight edges. In contrast, the islands of the disordered crystal are more rounded, showing no clear preferable orientation with regards to the crystallographic directions, indicating a more isotropic diffusion. This can be explained by disorder creating slight local variations in the lattice parameters and allowing the strain of the nitrogen reconstruction to be released. This strain release process could allow the reconstruction of islands without fundamental limits in their sizes.

Scanning the surface at higher bias voltage $V_b$ reveals features that were not evident for $V_b < 0.5\,\mathrm{V}$. Figure 4.3 shows the same island scanned at different bias voltages. At $V_b = 1.5\,\mathrm{V}$ we observe bright spots appearing in the nitrogen reconstruction. At $V_b = \mathrm{mV}\,10$ and with atomic resolution, we can see that those bright spots corresponding to defects in the nitride lattice (see insets of Figure 4.3). These defects, the position of which coincides with that of copper in the nitride layer, were observed only in the disordered phase. Although their exact nature is unknown, we suggest that they are Au atoms that are incorporated into the copper-nitride layer as substitutions of Cu atoms. In the $L1_2$ phase, every other layer in the (100) direction consists exclusively of Cu atoms; after saturation with nitrogen, the surface is terminated on a Cu-only layer [14]. A second kind of defect is visible at low bias (Figure 4.3a). This defect exhibits a two-fold symmetry with a central point at the Cu position. We suggest that they are missing copper in the nitride layer.

The defect distribution gives us an indication on the formation and merging of islands. On round islands, the defects are mostly around the edges, where during growth new nitrogen joins the island and where the $c(2\times2)$ reconstruction is therefore not completed. Due to Brownian movement, the islands diffuse on the surface and will eventually collide. This process of coalescence is visible in Figure 4.3, where two islands were frozen in the process of merging. Longer annealing time or higher temperature would allow the island to properly merge and adopt a round shape. This establishes a clear relation between the elongation of the islands and the coalescence between multiple islands.

Raising the annealing temperature allows for faster dynamics, accelerating the island merging process which consequently leads to larger and rounder islands. Figure 4.4a shows a $\sim 145\,000\,\mathrm{nm}^2$ island observed on the disordered crystal. The total area of this island is an improvement of three orders of magnitude respect to the maximum area of a nitrogen islands on Cu(100) [13]. However, in the inset of Figure 4.4a, taken at higher bias, we can observe a high density of defects on the nitrogen reconstruction evenly distributed along the island, suggesting a higher Au-Cu substitution at the surface at elevated growth temperatures. Nonetheless, we successfully evaporated and manipulated Fe atoms and on this island (white dots), and were able to engineer well-behaved spin structures (see Figure 4.6).

The area surrounding this island presents an irregular topography, highlighted in Figure 4.4c-e, which we will denote as percolation regions. We observe this kind of be-

haviour for the preparations we performed at highest temperatures. They consist of a square pattern broken up by irregular channels connecting larger islands, as well as clean patches of exposed $Cu_3Au$ surface. We have seen the percolation region to be unstable for $V_b > 4\,V$ both while scanning (see Figure 4.4e, f) and during spectroscopy (see Figure 4.5).

We note that on the same sample preparation, it is possible to observe areas in the percolation regime and areas with regular nitride islands by macroscopically displacing the STM tip accros the sample surface, indicating that various phases can coexist on a single crystal. By starting the annealing at a higher temperature and gradually lowering the temperature, we are able to create round large islands with smooth nitrogen reconstruction, where the defects are mostly on the edges.



Figure 4.5 shows constant current $dI/dV$ spectroscopy measurements on both regular and percolated areas. As seen in Figure 4.5b, the nitride islands in the regular region behave analogously to those reported for Cu(100) [30]. The peaks at 2 V and 4 V observed on the nitride layer resemble those reported on nitride on Cu(100)[31]. The peaks at bias voltage beyond 5 V are image state resonances. In the percolated region (Figure 4.5c,d), three distinct phases are observed: two that behave similarly to the regular region (red, green) and the phase with the square pattern (black), where the spectroscopy is mostly featureless (apart from its instability).

The nitrogen islands on $Cu_3Au(100)$ are suitable for adatom manipulation. We assembled many structures of Fe adatoms — from dimers to longer chains and blocks. Examples of such successfully assembled structure can be seen in Figure 4.6a. In Figure 4.6b we show spectroscopy measurements on the three atoms of a Fe trimer, which are quantitatively the same as for a trimer assembled on nitride on Cu(100) [32, 33]. Atomic manipulation is performed vertically, by moving an atom from the surface to the tip and subsequently form the tip to the surface on the desired position [4]. Whereas the atomic structures shown in Figure 4.6 were built on a disordered crystal, successful manipulation was also performed on an ordered crystal. We did not observe significant differences in either manipulation or spectroscopy between the two crystal phases.

## 4.4. CONCLUSION

We have studied the growth of $c(2 \times 2)$ nitride islands on the $Cu_3Au(100)$ crystal surface, which results in island sizes that are much larger than on the well-studied Cu(100) surface. When the crystal is prepared in the ordered phase, we observe mostly rectangular nitride islands, which increase in size with temperature. On the disordered phase we see a similar relation between annealing temperature and island size, but in this case the islands are round, indicating that effects of strain due to lattice mismatch have diminished. Measurements at higher voltages reveal defects, the distribution of which gives information about the coalescence of islands during growth. The nitride islands on $Cu_3Au(100)$ are found to be equally suitable for vertical manipulation of magnetic adatoms as their counterparts on Cu(100).

# REFERENCES


[1] J. Gobeil, D. Coffey, S.-J. Wang, and A. F. Otte, *Large insulating nitride islands on Cu3Au as a template for atomic spin structures,* Surface Science **679**, 202 (2019).

[2] A. Spinelli, B. Bryant, F. Delgado, J. Fernández-Rossier, and A. F. Otte, *Imaging of spin waves in atomically designed nanomagnets,* Nat Mater **13**, 782 (2014).

[3] F. M. Leibsle, S. S. Dhesi, S. D. Barrett, and A. W. Robinson, *STM observations of Cu(100)-c(2x2)N surfaces: Evidence for attractive interactions and an incommensurate c(2x2) structure,* Surface Science **317**, 309 (1994).

[4] C. F. Hirjibehedin, C. P. Lutz, and A. J. Heinrich, *Spin Coupling in Engineered Atomic Structures,* Science **312**, 1021 (2006).

[5] C. F. Hirjibehedin, C.-Y. Lin, A. F. Otte, M. Ternes, C. P. Lutz, B. A. Jones, and A. J. Heinrich, *Large Magnetic Anisotropy of a Single Atomic Spin Embedded in a Surface Molecular Network,* Science **317**, 1199 (2007).

[6] B. Bryant, A. Spinelli, J. J. T. Wagenaar, M. Gerrits, and A. F. Otte, *Local Control of Single Atom Magnetocrystalline Anisotropy,* Phys. Rev. Lett. **111**, 127203 (2013).

[7] A. Spinelli, M. Gerrits, R. Toskovic, B. Bryant, M. Ternes, and A. F. Otte, *Exploring the phase diagram of the two-impurity Kondo problem,* Nature Communications **6**, 10046 (2015).

[8] S. Loth, S. Baumann, C. P. Lutz, D. M. Eigler, and A. J. Heinrich, *Bistability in Atomic-Scale Antiferromagnets,* Science **335**, 196 (2012).

[9] A. Spinelli, M. P. Rebergen, and a. A. F. Otte, *Atomically crafted spin lattices as model systems for quantum magnetism,* Journal of Physics: Condensed Matter **27**, 243203 (2015).

[10] R. Toskovic, R. van den Berg, A. Spinelli, I. S. Eliens, B. van den Toorn, B. Bryant, J.-S. Caux, and A. F. Otte, *Atomic spin-chain realization of a model for quantum criticality,* Nat Phys **12**, 656 (2016).

[11] D.-J. Choi, R. Robles, S. Yan, J. A. Burgess, S. Rolf-Pissarczyk, J.-P. Gauyacq, N. Lorente, M. Ternes, and S. Loth, *Building complex Kondo impurities by manipulating entangled spin chains,* Nano Lett. (2017), 10.1021/acs.nanolett.7b02882.

[12] F. E. Kalff, M. P. Rebergen, E. Fahrenfort, J. Girovsky, R. Toskovic, J. L. Lado, J. Fernández-Rossier, and A. F. Otte, *A kilobyte rewritable atomic memory,* Nat Nano **11**, 926 (2016).

[13] J. C. Oberg, M. R. Calvo, F. Delgado, M. Moro-Lagares, D. Serrate, D. Jacob, J. Fernández-Rossier, and C. F. Hirjibehedin, *Control of single-spin magnetic anisotropy by exchange coupling,* Nature Nanotechnology **9**, 64 (2014).

[14] H. Niehus and C. Achete, *Surface structure investigation of nitrogen and oxygen on Cu3Au(100),* Surface Science **289**, 19 (1993).

[15] T. Choi, C. D. Ruggiero, and J. A. Gupta, *Incommensurability and atomic structure of c2x2 N/Cu100: A scanning tunneling microscopy study,* Phys. Rev. B **78**, 035430 (2008).

[16] W. P. Davey, *Precision Measurements of the Lattice Constants of Twelve Common Metals,* Phys. Rev. **25**, 753 (1925).

[17] Z. W. Lu, S.-H. Wei, and A. Zunger, *Electronic structure of ordered and disordered Cu3Au and Cu3Pd,* Phys. Rev. B **45**, 10314 (1992).

[18] R. Oguma, T. Eguchi, S. Matsumura, and S. K. Son, *Domain growth and off-phase boundary structures in L12-type ordering,* Acta Materialia **54**, 1533 (2006).

[19] T. M. Buck, G. H. Wheatley, and L. Marchut, *Order-Disorder and Segregation Behavior at the Cu3Au(001) Surface,* Phys. Rev. Lett. **51**, 43 (1983).

[20] V. S. Sundaram, R. S. Alben, and W. D. Robertson, *The order-disorder transformation at a (100) surface of Cu3Au,* Surface Science **46**, 653 (1974).

[21] C. Mannori, G. Boato, M. Canepa, P. Cantini, L. Mattera, and S. Terreni, *Surface vs. bulk order/disorder transition in a binary alloy. A He diffraction study of the Cu3Au(001) surface,* Europhysics Letters (EPL) **45**, 686 (1999).

[22] D. G. Morris, F. M. C. Besag, and R. E. Smallman, *Ordering and disordering in Cu3Au,* The Philosophical Magazine: A Journal of Theoretical Experimental and Applied Physics **29**, 43 (1974).

[23] K. D. Jamison, D. M. Lind, F. B. Dunning, and G. K. Walters, *Polarized LEED investigation of the order/disorder transition at a Cu3Au(100) surface,* Surface Science **159**, L451 (1985).

[24] D. T. Keating and B. E. Warren, *Long-Range Order in Beta-Brass and Cu3Au,* Journal of Applied Physics **22**, 286 (1951).

[25] A. Benisek and E. Dachs, *The vibrational and configurational entropy of disordering in Cu3Au,* J Alloys Compd **632**, 585 (2015).

[26] S. Katano, M. Iizumi, and Y. Noda, *Lattice dynamics of Cu3 Au in the ordered and disordered states,* Journal of Physics F: Metal Physics **18**, 2195 (1988).

[27] T. P. Moffat, F.-R. F. Fan, and A. J. Bard, *Electrochemical and Scanning Tunneling Microscopic Study of Dealloying of Cu3Au,* J. Electrochem. Soc. **138**, 3224 (1991).

[28] V. S. Sundaram, B. Farrell, R. S. Alben, and W. D. Robertson, *Order-Disorder Transformation at the (100) Surface of Cu3Au,* Phys. Rev. Lett. **31**, 1136 (1973).

[29] L. Houssiau and P. Bertrand, *Order-disorder phase transition of the Cu3Au(100) surface studied by ToF-ion scattering,* Nuclear Instruments and Methods in Physics Research Section B: Beam Interactions with Materials and Atoms Ion Beam Analysis, **118**, 467 (1996).

[30] T. Choi, C. D. Ruggiero, and J. A. Gupta, *Tunneling spectroscopy of ultrathin insulating Cu2N films, and single Co adatoms,* Journal of Vacuum Science & Technology B: Microelectronics and Nanometer Structures Processing, Measurement, and Phenomena **27**, 887 (2009).

[31] C. D. Ruggiero, T. Choi, and J. A. Gupta, *Tunneling spectroscopy of ultrathin insulating films: CuN on Cu(100),* Appl. Phys. Lett. **91**, 253106 (2007).

[32] S. Yan, D.-J. Choi, J. A. J. Burgess, S. Rolf-Pissarczyk, and S. Loth, *Control of quantum magnets by atomic exchange bias,* Nature Nanotechnology **10**, 40 (2015).

[33] S. Rolf-Pissarczyk, S. Yan, L. Malavolti, J. A. J. Burgess, G. McMurtrie, and S. Loth, *Dynamical Negative Differential Resistance in Antiferromagnetically Coupled Few-Atom Spin Chains,* Phys. Rev. Lett. **119**, 217201 (2017).

# 5

# STATE SWITCHING IN INTRINSICALLY FRUSTRATED ENGINEERED ATOMIC SPIN LOOPS

*We use atom manipulation to build closed loops of magnetic atoms, specifically designed to host magnetic frustration. Spin polarised STM measurements reveal that the magnetisation of the loops switches between two states that correspond to different locations in the loop for the frustration to be relieved. The balance between relief points can be influenced by means of a local tunable magnetic field produced by the STM tip.*

## 5.1. INTRODUCTION

In this chapter, we show the experimental realisation of a closed loop of atomic spins designed to host magnetic frustration. The design is such that the magnetic frustration can be released at two symmetrically equivalent pairs of interacting spins, creating a doubly degenerated ground state. The degenerated ground state caused by the magnetic frustration creates a highly sensitive system where small perturbations or defects could break the symmetry. Experimentally, we observe that the symmetry is broken and that spin arrangement favour releasing the magnetic frustration between only one of the two pairs. In addition, we observe that the system shows spontaneous switching between the two metastable frustrated states. The frequency of the switching, the lifetime of each state and the relative distribution of the two states are influenced by the effective local magnetic field and the current tunnelling through the atom. We use numerical calculations to evaluate the impact of the tip and of local variations in the system proprieties and determine which parameters could cause the breaking of the symmetry.



An introduction to magnetic frustration is presented in the next section (subsection 5.1.1) followed by a description of the substrate and the experimental conditions in subsection 5.1.2. In subsection 5.2.1 we explain the chosen design for the magnetically frustrated closed loop. We qualitatively and numerically discuss the consequences of this design in subsection 5.2.2 and subsection 5.2.3. The experimental realisation is presented in subsection 5.2.4 and the measurement with a spin-polarised scanning tunnelling microscope (SP-STM) in subsection 5.2.5. The data collected using the tip field to bias the local magnetic field and the numerical study are presented in subsection 5.3.1. Finally, we present some results of an extended loop in section 5.4.

### 5.1.1. MAGNETIC FRUSTRATION

We speak of magnetic frustration when the interaction between the spins of a structure make it such that it is not possible to satisfy all the couplings simultaneously. A common textbook example that illustrates magnetic frustration is three coupled spins placed on an equilateral triangle where the interaction between each spin is antiferromagnetic (AFM) and of the same magnitude[1]. This situation is illustrated in Figure 5.1. When trying to assign a value to each spin (up or down in an Ising model), we will first antialign two spins to satisfy the AFM coupling between them. When trying to assign a value to the third one, we will necessarily have one of its coupling not satisfied: it is frustrated. Moreover, which coupling is frustrated is arbitrary, each situation leading to the same total energy, and thus the system host a six-fold degenerated ground state ($2^3$ possible combination minus 2 for when all the spin are aligned up or down). When including the Zeeman energy and an external magnetic field, the ground state will include two of the spins aligned with the field and so the system will have a three-fold degenerated ground state. If the field is high enough, the Zeeman energy can overcome the coupling energies and create more mismatched couplings and lift some or all of the ground state's degeneracy.

The basic frustrated structure of three spins can be extended by adding more spins

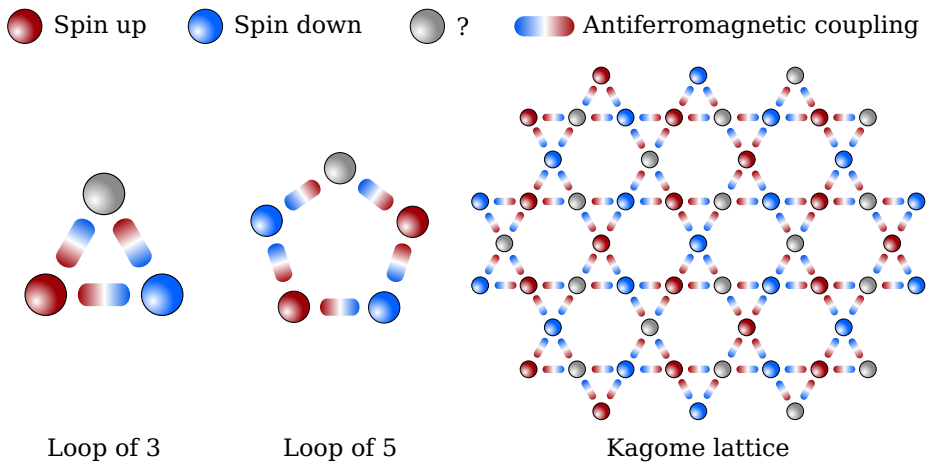


**Figure 5.1: Examples of structures hosting magnetic frustration**. Two examples of loops and one example of periodic structures (Kagome lattice) that can exhibit magnetic frustrations. The coupling between the spins (the circles) are all antiferromagnetic and of the same magnitude. The loops have an odd number of couplings and could be extended to created larger loops by adding an even number of antiferromagnetic couplings or any number of ferromagnetic coupling. The Kagome lattice is an example of structure with a massively degenerated ground state. The frustration points are numerous and the possible configuration are many. This is an example of large scale frustration with long range correlation between the spins where any change in one spin will affect the structure on a large scale.



in the loop or coupling multiple loops together. As long as the loops have an odd number of AFM bonds it will host magnetic frustration and have a multi-degenerated ground state. Usually, magnetic frustration is considered and studied in periodic lattices[2–6]. Multiple 2D structures like the triangular and the Kagomé lattice[2, 7], and 3D structure like the pyrochlore lattice[3], have been the subject of theoretical and experimental works on magnetic frustration. In such periodic lattices the frustrations are numerous and scale with the size of the system. This leads to massive degeneracy which allows quantum entanglement effects to survive over long distances. Interesting and peculiar effects have been predicted in such systems, such as special states of matter known as spin liquid[8–10] and spin ice[11].

### 5.1.2. EXPERIMENTAL SETUP

In this section, we present the experimental setup used, the sample and its basic properties. The two STMs available to the group and the general theoretical background common to most studies of magnetism with STM was discussed in chapter 2 and chapter 3. The reader is referred to these chapters for more details.

The experiment was carried out in our lab using the Unisoku USM-1300 $^3$He. Even if this STM is equipped with a vector magnet allowing a maximum of 9 Tesla out-of-plane and 2 Tesla in-plane, only the in-plane field was used up to a maximum field of 1 Tesla. As discussed below, this field is parallel to the easy axis of the assembled structure. A

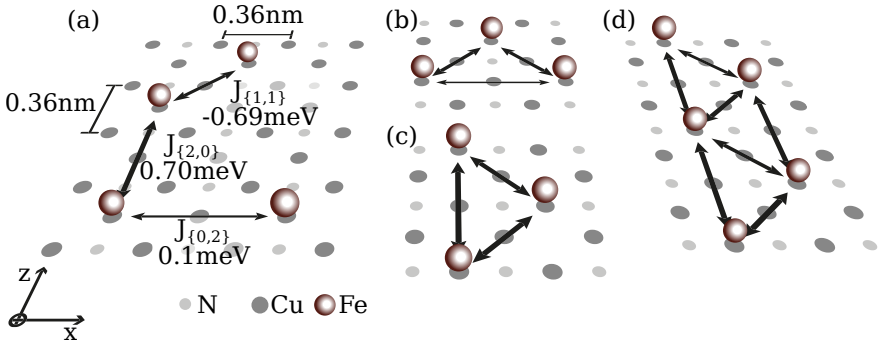


**Figure 5.2: The $Cu_2N$ substrate with example of structures**. (a) A $Cu_2N$ lattice with three Fe adatoms. The notation for the distance ($\{\Delta z, \Delta x\}$), the direction of the z-axis and x-axis and the three couplings that are considered in the experiment are indicated. The Fe adatoms are on top of Cu atoms and bound with two nearby N atoms along the z-axis (easy axis. The atoms can also bound along the x-axis, but that configuration wasn't used. (b-c) Two minimal structures that could exhibits magnetic frustration. (d) An example of a frustrated structure with 5 adatoms. The structures presented in (b-d) are experimentally not realisable because their atoms are too close.



commercial $Cu_3Au(100)$ crystal (from MaTecK), prepared *in-situ* and kept in ultra-high vacuum ($< 2 \times 10^{-10}$ mbar) was used as a substrate.

The sample used for the experiment is a $Cu_3Au(100)$ crystal on top of which copper-nitride ($Cu_2N$) islands were grown [12]. This system was presented in chapter 4. We used the $Cu_2N/Cu_3Au(100)$ as an alternative to the $Cu_2N/Cu(100)$ substrate as the two systems show similar properties with the notable advantage that $Cu_2N/Cu_3Au(100)$ offers larger $Cu_2N$ islands than $Cu_2N/Cu(100)$. As far as we observed, adtoms on the nitride layer behave similarly to those on $Cu_2N/Cu(100)$ islands and it is possible to use the knowledge and expertise acquired on $Cu_2N/Cu(100)$[13–24]. The sample was first prepared by a successive round of argon sputtering and annealing until a clean surface was observed with the STM. The islands were created by nitrogen sputtering followed by annealing the sample to promote the reconstruction of the islands. Iron atoms were evaporated on the resulting sample.

We used Fe atoms as the building blocks for assembling the magnetic structures over $Cu_2N$ insulating islands. Assembling magnetic structures on insulating islands brings two important advantages over assembling directly on the metal substrate. One key characteristic is that the islands decouple the adatoms from the conduction electrons of the metal, which would limit the lifetime of the states that we are trying to observe[15, 25]. Another advanteage is that, when evaporated on $Cu_2N$, Fe atoms preferentially occupy a bridge position[26, 27] where the Fe binds to two neighbouring N atoms and sits on top of a Cu atom, as shown in the Figure 5.2. The crystal field originating from this arrangement creates a strong uniaxial magnetic anisotropy, along the direction of the N bonds. It should be noted that two such directions exists, 90 degrees rotated from each other. It is important to place the adatoms on the correct row such that they align with the direction of the external field The orbital momentum of the Fe on $Cu_2N$ is mostly

quenched with a g-factor of $g = 2.11$[26]. The Fe adatoms carry a spin of $S = 2$ and will align parallel to the N–Fe–N bounds.

In the rest of this chapter, we will use the following notations. The relative position of two atoms on the surface will be noted $\{\Delta z, \Delta x\}$, where $\Delta z$ and $\Delta x$ are the absolute distance in unit-cell of $Cu_3Au(100)$ in the z-axis and x-axis, respectively. The z-axis will be parallel with the easy-axis of the Fe adatoms, and the x-axis will be perpendicular to the z-axis and in-plane. These notations are shown in Figure 5.2 and Figure 5.2.

Placing two Fe atoms at a distance of $\{1,0\}$ or $\{0,1\}$ is impractical, because in these configurations the atoms will to bound to the same N atoms or be too close, respectively. The typical closest positioning between Fe atoms are $\{2,0\}$, $\{0,2\}$ and $\{\pm1,\pm1\}$, with corresponding coupling noted $J_{\{2,0\}}$, $J_{\{0,2\}}$ and $J_{\{1,1\}}$, respectively. These will be the basic building block that will be used to create our structures. For longer distance, like $\{2+,1+\}$ and $\{1+,2+\}$, the coupling is weak and will not be considered.

Two nearby adatoms on the surface interact via the itinerant electrons of the substrate and mostly mediated through the Fe–N bounds[17, 22]. This interaction can be modelled using the Heisenberg Hamiltonian, as introduced in chapter 2. In this model, the coupling magnitude ($J_{i,j}$) between two spins is determined empirically from the shift in the inelastic excitation steps present in $dI/dV$ measurements done on atoms in the corresponding configuration. The three types of coupling used in the present experiment are $J_{\{2,0\}} = 0.70\,\text{meV}$[18, 28], $J_{\{1,1\}} = -0.69\,\text{meV}$[18, 28] and $J_{\{0,2\}}$. The $J_{\{0,2\}}$ value is a small AFM coupling that we estimate to be around $J_{\{1,1\}} = 0.1\,\text{meV}$. This value was not precisely measured experimentally but correspond qualitatively to the experimental observation of a weak AFM bound. This will be sufficient for our discussion.

The reported anisotropy of an isolated Fe atom over a Cu atom of a $Cu_2N$ islands is $D = 1.55\,\text{meV}$ and $E = 0.31\,\text{meV}$[26, 28]. The proximity of other atoms will also influence the anisotropy as nearby adsorbed atoms deform the lattice mesh[28]. The planar anisotropy $E$ is not be significantly disturb by the nearby atoms, but the axial anisotropy can show significant variations. For two Fe adatoms with a $\{2,0\}$ relative positioning, the presence of the other adatom along its easy-axis increases the axial anisotropy and was measured to be $D = -1.87\,\text{meV}$[18, 28]. The increase of the axial anisotropy is even greater when the adatom is surrounded by two adatoms (the middle atom of a $\{2,0\}$ trimer for example) with a measured value of $D = -2.42\,\text{meV}$[18]. In the case of the $\{1,1\}$ spacing, the axial anisotropy is reduced to a value between $-1.29\,\text{meV}$[22] and $-1.37\,\text{meV}$[28].

## 5.2. THE D-SHAPED SPIN LOOP

### 5.2.1. DESIGN

The objective of the experiment is to build a closed-loop hosting magnetic frustration. To achieve this objective, an odd number of AFM coupling inside the loop is required. The smallest loop with such proprieties is composed of three atoms with either one $J_{\{2,0\}}$ or one $J_{\{0,2\}}$ as illustrated in Figure 5.2 b and c. Experimentally, building such close-packed triangle ($(0,0)-(1,1)-(2,0)$ or $(0,0)-(1,1)-(0,2)$ was proved impractical because of the

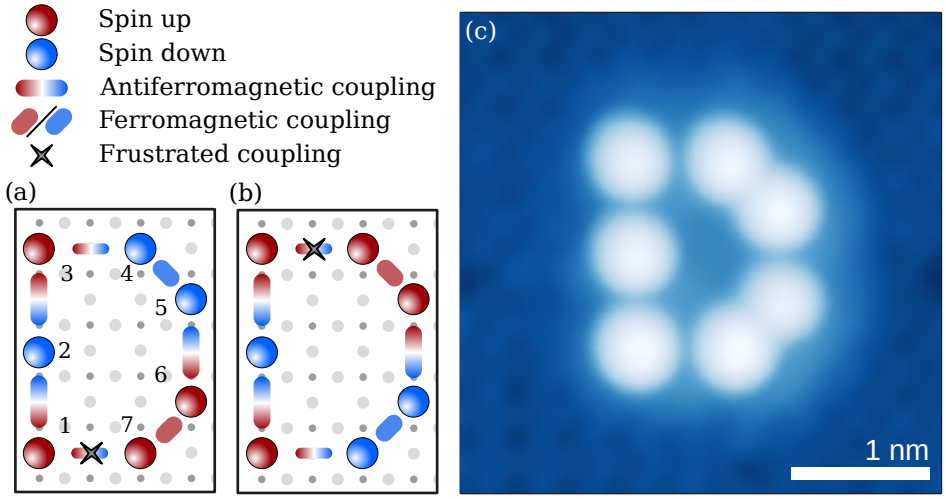


**Figure 5.3: The frustrated d-loop**. (a) Ball-model of the two spins configuration showing the position of the frustrated coupling (a magnetic field is applied in the z-axis direction). (c) Constant current topographic image of the experimentally assembled structure taken with a spin averaging tip at 50 pA and 20 mV. Each white spherical shape correspond to an iron atom placed to form the structure.

close packing of the adatoms, as mentioned above. Extending the structure in the $x$ axis to 5 atoms (Figure 5.2(d)) does not solve this issue as the structure still contains the problematic small structures. Extending this last structure in the $z$ direction this time lead to the structure presented in Figure 5.3.

This design is as follows. Starting in the bottom left corner, we place the atoms in those successive configurations: $\{2,0\}$, $\{2,0\}$, $\{0,2\}$, $\{-1,1\}$, $\{-2,0\}$ and $\{-1,-1\}$ so that the last atom also is at a $\{0,2\}$ spacing with the first atom and closes the loop. The atoms will be named by their position (1 to 7) starting for the bottom left and rotating anticlockwise. We will also name the three leftmost atoms (atoms 1, 2 and 3) the trimer, the two top right atoms (atoms 4 and 5) the top dimer and the two bottom right atoms (atoms 6 and 7) will be the bottom dimer. The reason of those names will be apparent in the following sections.

The resulting structure has 7 atoms and 7 next-neighbour couplings. Two of those couplings are FM couplings ($J_{4,5} = J_{6,7} = J_{\{1,1\}}$) and 5 are AFM couplings ($J_{1,2} = J_{2,3} = J_{5,6} = J_{\{2,0\}}$ and $J_{3,4} = J_{7,1} = J_{\{0,2\}}$). The 5 AFM couplings fulfil the requirement for magnetic frustration of an odd number of AFM couplings in a closed loop.

### 5.2.2. QUALITATIVE ANALYSIS

Fe adatoms on $Cu_2N$ are spin-2 atoms with a strong easy-axis magnetic anisotropy[28]; this constrains the spins to align parallel to this easy-axis (the z-axis in Figure 5.2). We expect that the structure will exhibit a ground state composed of $\pm 2$ spins align along

the easy-axis, which we will note as ↑ for the +2 spins (aligned) and ↓ for −2 spins (anti-aligned).

If we assign a value to the spin of the atoms, ↑ or ↓, trying to satisfy the AFM or FM nature of the couplings, we realise that it is not possible without including a frustrated coupling. For example, beginning by assigning ↑ to the atom 1 and sequentially assigning the next spin value by following the AFM or FM property of the couplings, we obtain the series ↑↓↑↓↓↑↑. The last coupling closing the loop, between 7 and 1, is an AFM coupling, but the two spins are ↑ and ↑: this coupling is magnetically frustrated. Beginning with a ↓ spin for atom 1 will lead to a similar result but with the spin of the atoms 4 to 7 inverted.

If the couplings were to have all the same magnitude, the ground states would be 14 times degenerated, one for each frustrated couplings times two for the two spin orientations. In the actual structure, the couplings are not all equivalent. There are three strong AFM couplings ($J_{\{2,0\}}$), two almost as strong FM couplings ($J_{\{1,1\}}$) and two weak AFM coupling ($J_{\{0,2\}}$). The strong AFM and FM have similar magnitude, but the $J_{\{0,2\}}$ couplings, between atoms 1 and 7, and between atoms 3 and 4, are significantly weaker. The energy cost of having these couplings frustrated will be lower than for the rest of the couplings, and so, the system ground states must include one of the two $J_{\{0,2\}}$ being frustrated. This reduces the number of degeneracy of the ground states to four. The four generated and frustrated ground states are $|\uparrow\downarrow\uparrow;\uparrow\uparrow\downarrow\downarrow\rangle$, $|\uparrow\downarrow\uparrow;\downarrow\downarrow\uparrow\uparrow\rangle$, $|\downarrow\uparrow\downarrow;\uparrow\uparrow\downarrow\downarrow\rangle$, and $|\downarrow\uparrow\downarrow;\downarrow\downarrow\uparrow\uparrow\rangle$. The ";" separates the trimer from the rest of the atoms to ease the reading and to indicate that the behaviour of the trimer is partially decoupled from the rest of the loop.

When we apply a magnetic field in the easy-axis direction (z-axis), the Zeeman effect will further reduce the degeneracy of the ground state. With a magnetic field, the states with more atoms aligned with the field will have a lower energy. In the previously mentioned states, 2 have 4 of its 7 atoms aligned, and 2 have 3 of its 7 atoms aligned. The 2 states with 4 of its 7 atoms aligned have a lower total energy and will be favoured. The ground states are now $|\uparrow\downarrow\uparrow;\uparrow\uparrow\downarrow\downarrow\rangle$ and $|\uparrow\downarrow\uparrow;\downarrow\downarrow\uparrow\uparrow\rangle$. The partial decoupling because of the weaker $J_{\{0,2\}}$ couplings is more apparent now. When a field is present, we can see the structure as a fixed trimer in a $|\uparrow\downarrow\uparrow\rangle$ state, while the rest structure is in a combination of $|\uparrow\uparrow\downarrow\downarrow\rangle$ and $|\downarrow\downarrow\uparrow\uparrow\rangle$ states.

### 5.2.3. NUMERICAL ANALYSIS

Collection of magnetic adatoms on $Cu_2N$ islands were successfully modelled using a Heisenberg Hamiltonian including surface magnetic anisotropy and Zeeman energy [15, 18, 23]. We use a similar model to do a quantitative analysis of the expected behaviour of the structure.

The Heisenberg Hamiltonian is composed of three parts: the Heisenberg coupling ($\mathcal{H}_{Heisenberg}$), the surface magnetic anisotropy ($\mathcal{H}_{anisotropy}$) and the Zeeman energy ($\mathcal{H}_{zeeman}$). For the Heisenberg coupling, we only consider the first neighbours in the loop. The total Hamiltonian take the form

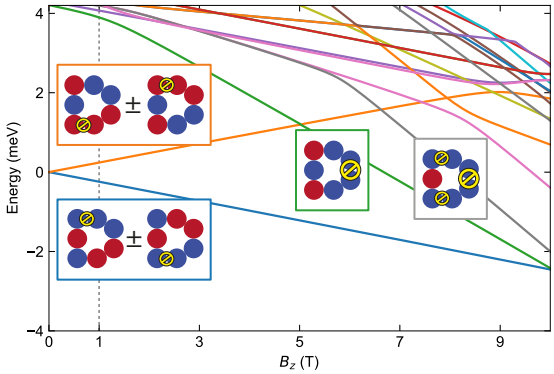


**Figure 5.4: Energy diagram of the frustrated d-loop**. Energy diagram of the first 20 energy states under a variation of an external magnetic field from 0 Tesla up to 10 Tesla. The dashed vertical line indicate where most of the experimental data were taken (1 Tesla). The small inserts represent the corresponding states composition of the $S_z$ projection for the states (the colour of each border is the same as the energy line it represent). The two divergent lines crossing starting at 0 meV are both 2-fold degenerated with the frustrated coupling either between 3-4 or 7-1.



$$\mathcal{H} = \mathcal{H}_{Heisenberg} + \mathcal{H}_{anisotropy} + \mathcal{H}_{zeeman} \tag{5.1}$$

with the right parts defined as

$$\mathcal{H}_{Heisenberg} = \sum_{i=1}^{N-1} J_{i,i+1}\vec{S}_i \cdot \vec{S}_{i+1} + J_{N,1}\vec{S}_N \cdot \vec{S}_1 \tag{5.2}$$

$$\mathcal{H}_{anisotropy} = \sum_{i=1}^{N} D_i S_{z,i}^2 + E_i\left(S_{x,i}^2 - S_{y,i}^2\right) \tag{5.3}$$

$$\mathcal{H}_{zeeman} = \sum_{i=1}^{N} -g\mu_B \vec{B} \cdot \vec{S}_i \tag{5.4}$$

where $N$ is the number of atoms (7 in the current structure), $J_{i,j}$ is the coupling between atom $i$ and $j$, $\vec{S}_i$ is the spin operator for the atoms $i$, $D_i$ and $E_i$ are the uniaxial and transverse anisotropy, $g$ is the rightfully called g-factor, $\mu_B$ is the Bohr magneton and $\vec{B}$ is the external magnetic field. The last term of Equation 5.2 ensure that the chain form a closed loop. A more general $\mathcal{H}_{Heisenberg}$ term considering the coupling between all adatoms would include the summation on all pairs of spins. In our case, we only consider neighbouring atoms coupling.

We calculated the states' energy and their composition in relation with a z-align external magnetic field. The detail of the calculation can be found in chapter 3. The resulting energy diagram is shown in Figure 5.4. From this diagram, we can confirm our previous conclusion about the ground state. At non-zero magnetic field, the ground

state is composed of the trimer in a Néel state $|\uparrow\downarrow\uparrow\rangle$ and the two dimers are in a superposition of $|\uparrow\uparrow\rangle$ and $|\downarrow\downarrow\rangle$. The frustrated coupling is one of the two $J_{\{0,2\}}$, either between atoms 1 and 7 or between atoms 3 and 4. Only at a high enough magnetic field of $B_z = 2\left(J_{\{2,0\}} - J_{\{0,2\}}\right)/\left(g\mu_B\right) \approx 10\,\mathrm{T}$ it is energetically favourable to release the frustration between the two dimers, inverting the trimer at the same time. In this high magnetic field ground state, 5 of the 7 spins are aligned with the field.

In the following experimental data, a magnetic field of 1 Tesla (dashed line on Figure 5.4) is used. At this field, the Zeeman energy causing the splitting between the ground state and the first excited state is $\approx 0.48\,\mathrm{meV}$. Typically, experiments were performed at a bias voltage 1 mV at the junction and so, the energy of the tunnelling electrons is higher than energy needed to excite the structure. However, due to selection rules this does not prevent us from observing the spin state of the underlying atoms during a spin-polarised measurement, as one electron carries a spin of ±½and thus can only induce a change in the total spin of the structure of 1. Consequently, the process of exciting from the ground state to the first excited state is a multi-electrons process and will rarely occur at the current used in our experiments.



Another point to consider that could limit the proper observation of the state during a spin-polarised measurement is the atomic exchange bias induced by the polarised tip[24]. The presence of a spin polarised cluster of atoms at the tip allows the spin sensitive measurements in STM[29, 30]. It is a fundamental technique when studying magnetism with an STM. However, this cluster can also interact with the atoms that we are trying to measure via an exchange interaction. This interaction can be included in the Heisenberg Hamiltonian by including an equivalent correction to the local magnetic field[24]. Because of this equivalence, and to ease of discussion, we will call this interaction the "tip field". This tip field, noted $B^{tip}$, follows an exponential decay with the distance as

$$B^{tip}(z) = B_0^{tip} e^{-\lambda(z-z_0)} \tag{5.5}$$

, where $B_0$ is a constant corresponding the field at $z_0$, and $\lambda$ characterise the decay.

During scan, the tip field changes the balance in the energy and split the degeneracy of the states $\uparrow\uparrow\downarrow\downarrow$ and $\downarrow\downarrow\uparrow\uparrow$ of the two dimers. This means that, if the tip field increase or decrease the local field, all the observed spins should be $\uparrow$ or $\downarrow$ respectively when scanning the dimers. However, at low current (*i.e.* tip far from the surface) the tip field influence should be small and be mostly averaged by the thermal fluctuations.

### 5.2.4. BUILDING THE LOOP

Before the manipulation of the adatoms to assemble the structure, the Fe atoms were first identified using their characteristic bias spectroscopy curve ($dI/dV$)[20]. Fe atoms over a Cu site bound to two nitrogen atoms, present a step-like feature at +/-4meV originating from an inelastic excitation; Fe atoms over an N site do not present this low energy feature. If the expected curve is not observed, a bias pulse is used to attempt to nudge the atom onto a proper Cu site, so it can be identified as Fe atom after another $dI/dV$

measurement. To assure that only Fe atoms were used to build the structure, only atoms with the proper signal were used. Depending on the samples, the proportion of rightly identified atoms can be up to 80-90% of the adatoms. The rest are either contamination or Fe atoms bounded to the surface in a peculiar way or affected by a defect.

When the atom is confirmed to be a Fe atom it is moved to his final position using vertical manipulation[31, 32] with a *pickup*, *drop* and *hop* procedure adapted from the manipulation on $Cu_2N/Cu(100)$[21]. The final step of the manipulation, the *hop*, consists in a bias voltage pulse not strong enough to pick up the atom but will instead make the atom hop laterally (or jump) onto a Cu site and bind to two N atoms. The direction of the hop and bounding determine the easy-axis direction. In our experiment, all the hops were done so that the easy-axis direction is parallel to the z-axis. The same axis is used to when an external magnetic field applied.

The building procedure follows the order with which we numbered the atoms. First the trimer was built (atoms 1, 2 and 3), followed by the top dimer (atoms 4 and 5) and finally the bottom dimer (atoms 6 and 7). Many attempts were needed to properly place the last atom (atom 7) as the final hop had a tendency to disturb the atoms already placed.



A constant current topographic scan of the assembled structure is presented in Figure 5.3(c). The atoms seem at their rightful position but the atoms 6 and 7 seem to have slight differences in relative height and size compared to the other atoms. This could be due to a difference in the height of the substrate or and improper positioning or bounding.

### 5.2.5. SPIN-POLARISED TOPOLOGY

The topography images consist of constant current scans. The current is the integral of the local density of states (LDOS) from the Fermi level up to energy set by the bias voltage. The LDOS of most atom is differs for the spin up or down. It is possible to resolve the spin configuration of the structure, by introducing a spin dependence to the contribution of the current. This can be realised by magnetizing the tip apex, enabling the technique known as Spin Polarised STM (SP-STM). Conveniently, the same Fe atoms that were evaporated on the surface to build the structure can be used to magnetise the tip. To do so, we pick up with the tip some Fe atoms to create a magnetic cluster at the apex of the tip. Simply put, this cluster will spin-polarises the current, *i.e.* creating an unbalance in the proportion of the electrons' spin $\uparrow$ and $\downarrow$ in the tunnelling current. The probability with which an $\uparrow$ or $\downarrow$ electrons can tunnel through one adatom depends on the spin state of this adatom, or put differently on the uneven LDOS between the spin up and down. Combining those two observations, the unbalanced current and the conductance dependence, a spin-polarised tip will measure different current at a given height over an adatom depending on the spin value of the adatom, or different height for a constant current measurement. It is to be noted that the intensity of the current polarisation can vary greatly from tip to tip and a trials and errors approach is used to get a "good" polarised tip.

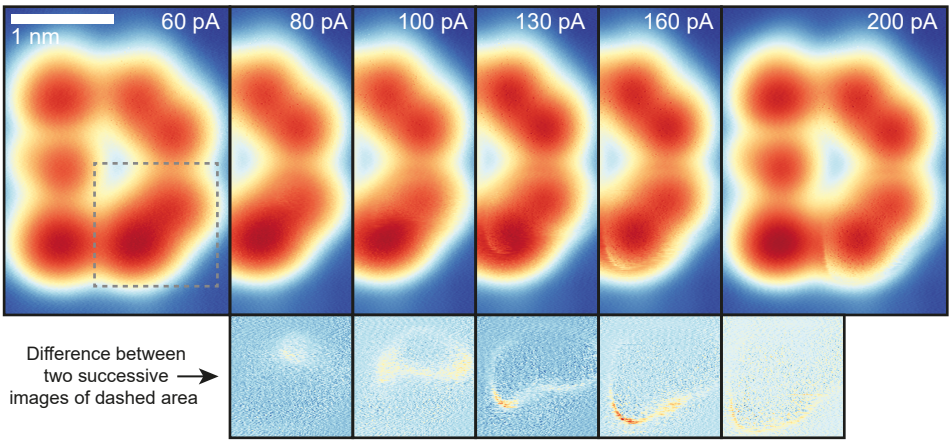


**Figure 5.5: Spin-polarised topographic scan of the frustrated d-loop**. Spin-polarised constant current topographic image of the structure taken at 2 mV and an external magnetic field of 1 Tesla taking at various regulating current. Top: images taken at increasing regulating current showing the states changing as the tip go closer (higher regulating current imply a closer tip). Bottom: Difference between two successive current of the dashed area highlighting the variation of the spin flipped area and its progression with the change of tip height.



An in-plane magnetic field, parallel to the atoms easy-axis, was applied during the measurement. The magnetic field assures a proper polarisation of the tip magnetic cluster, that we assume to be (mostly) parallel to the external field. The field also creates a split of the ground state and the first excited state due to the Zeeman energy as presented in Figure 5.4. Under this magnetic field we can consider the trimer as fixed in the state $|\uparrow\downarrow\uparrow\rangle$ and use it as a reference for the polarisation of the atoms and a test for the proper spin polarisation of the tip.

The SP-STM constant current topographic images of the structure are shown in Figure 5.5. The images were taken with an external magnetic field of 1 Tesla. On the images, we can observe the difference in apparent height of the atoms compared to Figure 5.3(c). This contrast is due to the magnetisation of the atoms. At this field, we concluded previously that the trimer (atoms 1,2 and 3) adopt the Néel state $|\uparrow\downarrow\uparrow\rangle$. From this observation, we can infer the spin of the other atoms. At 60pA , the top dimer (atoms 4 and 5) adopt a $|\downarrow\downarrow\rangle$ state, and the bottom dimer (atoms 6 and 7) a $|\uparrow\uparrow\rangle$ state.

These observations differ from the predictions of the qualitative and quantitative analysis. We expected a degenerated ground states with an equal probability of spin $\uparrow$ and $\downarrow$ for the atoms 4, 5, 6 and 7, with possibly a biased due to the local tip-field. The observed spins should either be averaged at zero or a switching between the $\uparrow$ and $\downarrow$. However, a clear unbalance is observed were the state $|\uparrow\downarrow\uparrow;\uparrow\uparrow\downarrow\downarrow\rangle$ is favoured, even over multiple scans. In this configuration, the frustrated bound is between the atoms 1 and 7.

## 5.3. TIP-FIELD BIASING

The presence of the magnetic cluster at the apex the tip polarising the tunnelling current allowing the observation the atoms' spin also creates the so-called tip field. This tip field gave us a new tool to probe the structure. By measuring at different tip-sample distance (or at different regulating current and so changing the tip-sample distance) we vary the local magnetic field experienced by the atoms and can dynamically change the conditions of the experiment. In Figure 5.5, the loop is scanned in a constant current mode at different regulating currents while the external magnetic field is kept constant at 1 Tesla. As the current increase, we can see the atoms 4 and 5 progressively going from a $|\uparrow\uparrow\rangle$ state to a $|\downarrow\downarrow\rangle$ state. This change and how it progress is made more evident in the bottom images of Figure 5.5 highlighting the difference between two successive scans of the bottom dimer. We can observe the sharp transition and the progression of spin flipped area. The atom 6 is changing state at lower current than the atom 7 and the flipped area grow toward the atom 7 as the tip go closer. The sharpness of the flip is enhanced by the feedback loop that will bring the tip closer to the sample as soon as the spin flip occur. The process is as follows: the local magnetic field is reduced by the nearby tip; the spin flip because of a change in the ground state; this decrease the current because of the increased in magneto-resistance; in return the feedback bring the tip closer to the sample to compensate for the decrease in current; the tip being closer, the intensity of the local tip-field on the atom is increased and prevent a flip back of the spin. This reduces the switching area where the ground state and the first excited state overlap in energy and where a switching between the two states occur.



After the spin flip, the height the bottom dimer is similar to the height of the top dimer, indicating that their spins have the same value and confirming the initial $|\uparrow\uparrow\rangle$ state of the bottom dimer. The rest of the atoms does not change. Specifically, the atoms 6 and 7 stay in their apparent $|\downarrow\downarrow\rangle$ states and the trimer in a $|\uparrow\downarrow\uparrow\rangle$ state even at high scanning current. This indicates that the tip field is either too weak to induce a change in the state, like for the trimer, or that the tip field reinforces the state, and no switching can occur, like for the top dimer.

The field biasing effect created by the tip is expected to be a function only of the distance to the atoms and be independent of the current intensity or direction. To confirm that this is really the nature of observed phenomenon and discard the possibility of a spin-pumping effect[33], we measured the current-height relation ($z(I)$) at different bias voltages. The regulating current was varied between 60 pA and 400 pA when measuring in the centre of the trimer's top atom (atom 3). The feedback loop was kept active during this experiment and so will try to maintain the target regulating current by correcting the height of the tip. The resulting tip height is measured. The measure was repeated positive and negative biasing voltages between $\pm$0.6mV and $\pm$1.4mV. The resulting curves are shown in Figure 5.6(a).

As expected, the variation in voltage biases change the initial and final height of the tip. A clear transition is observed at a height of 60 pm ($z = 0$ pm is arbitrary). This transition is indicated by the grey area. In addition, this transition happens at the same height independently of the current, bias voltage or bias polarity. This confirms that the effect

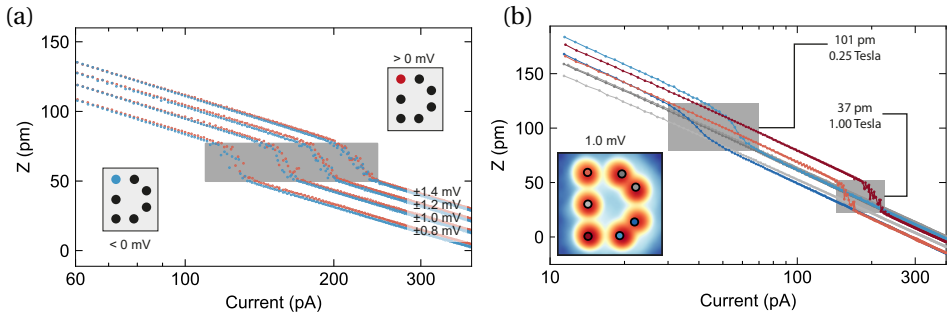


**Figure 5.6: Current vs height of a spin-polarised tip over the d-loop atoms**. (a) The height of the tip ($Z$) in relation the regulating current on the atom 3 take at different positive bias (in red) and negative bias (in blue). The grey area indicates the region where the spins flip between the up and the down states. (b) The height of the tip($Z$) on all the atoms taken at a bias voltage of 1 meV. The grey area indicate the region where the change of state occurs. The two blue curves (taken on the bottom dimer) switch in the same range of height. The same observation can be made for the red curves (two ends of the trimer). The grey lines show no switching. They correspond to the atoms in an initial down state (middle trimer and top dimer). Also indicated an estimated value of the field caused by the spins are switching. The inset indicate where the data was recorded on the atoms. In (a) and (b) the $z = 0$ value is arbitrary.

depends only on the distance with the atom. We interpret this transition as the switch from an initial ↑ state of the atom 3 when the tip is far away, to a ↓ state when the tip is close.

Furthermore, all the curves follow the same exponential decay, as show in Figure 5.6 by the linear curves on a log scale. The difference between the curves is only in their prefactor that depends on the voltage bias. The exponential decay follows the standard curves of tunnelling current, and, except for the transition area, the spins are either ↑ or ↓ and not mixed or in a superposition of states. If this were not the case, they would deviate from an exponential as the proportion of spin ↑ and ↓ would change progressively with the local field and so the current.

Another information inferred from those curves is the opposing effect of the tip field. The calculation shows that the trimer will adopt a $|\uparrow\downarrow\uparrow\rangle$ Néel state a 1 Tesla (or any field $> 0$). The transition will happen when the tip field fully cancels the external magnetic field so that the local effective field is zero. This implies that at this distance the tip field produce locally a field of -1 Tesla. The magnetic tip field goes against the external magnetic field and locally reduce it, otherwise the tip field would make the energy of the current state lower, and we would not observe a switch.

### 5.3.1. BIASING THE ATOMS

We repeated the same experience at a constant voltage bias of 1.0mV on all the atoms. In Figure 5.6(b), all the $Z(I)$ curves follow the same exponential decay, both before and after the switch, but have different heights. This difference in height is due to some experimental considerations. First, some atoms appear naturally higher or lower due to slight variation of the surface and an imperfect calibration of the surface plane. Secondly, un-

like in the topographic image in Figure 5.3, where an exceptionally sharp non-SP tip made it possible to clearly distinguish the individual atoms forming the structure, the SP functionalised tip used in Figure 5.5 and Figure 5.6 cannot reliably distinguish the atoms of the dimers. To find the position of those atoms we first place the tip over the atom 1 using an apex tracking algorithm. Subsequently, the tip was moved relatively from this position to the desired atom. The actual positions where the curves were recorded is shown in the inset of Figure 5.6(b). We can see slight mismatch due to a difference in the estimated $Cu_2N$ lattice constant, on the angle of the lattice relative to the z-axis and an imperfect tracking algorithm. A small correction of the height of some atoms (>3.9 pm) was applied to compensate these variations and for the tilt of the sample.

In Figure 5.6(b), we can see three different behaviours of the atoms: no switching (in grey, atoms 2, 6 and 7); switching at high current (in red, atoms 1 and 3), and switching at low current (in blue, atom 4 and 5).

The first set of curves, the grey curves, correspond to atoms 2, 4 and 5, shows no switching. They correspond to the atoms that are in a $|\downarrow\rangle$ state when the tip is far away. The spin of these atoms is anti-aligned with the external field and contribute a positive Zeeman energy to the total energy. Lowering their local field reduce the Zeeman energy and make the actual state ($|\downarrow\rangle$) more favourable and no switching can occur as the tip go closer.

The second set of curves, in red, includes atoms 1 and 3. Those two atoms are the ends of the trimer. The trimer is in a Néel state $|\uparrow\downarrow\uparrow\rangle$ when an external field is applied. When the tip is far (low current), the two atoms are in a $|\uparrow\rangle$ state. As the tip go closer, the local field is reduced until the atom begins to switch from $|\uparrow\rangle$ to $|\downarrow\rangle$. Using the Heisenberg Hamiltonian model, we calculated that the inflexion point happens when the local field is null, *i.e.* when the tip field is as strong as the external field (1 Tesla in the current experiment). The two atoms are switching at the same range of height, between 22 pm and 52 pm. The $z = 0$ value is set arbitrary, but consistently for all the $Z(I)$ curves.

The third set of curves, in blue, formed by the atoms 6 and 7, correspond to the bottom dimer. The switching occurs when the tip is at a greater distance than for the atoms of the trimer and so the biasing tip field lower. The switching area is the same for the two atoms and is between 79pm and 123pm. They are more sensitive to the disturbance caused by the tip field.

It is surprising that we can observe a switching at all. If all the magnetic anisotropies and couplings were all symmetric, *i.e.* no difference between the top dimer and the bottom dimer, as described before, they should behave similarly. The states $|\uparrow\uparrow\rangle$ and $|\downarrow\downarrow\rangle$ for the bottom and top dimer should be degenerated. Any hinder of the local field would break that degeneracy and favour the $|\downarrow\downarrow\rangle$ state, and we should observe only the $|\downarrow\downarrow\rangle$ state, or switching at low current. The observation of a switching on the bottom dimer and no switching on the top dimer imply that the structure is asymmetric.

The underlying principle of the tip field effect is exchange interaction. This interaction intensity is due to the overlap of the wave function of the tip and the adatoms. The sample overlap is at the origin of the tunnelling current in STM. It is reasonable to

| Name | Symbol | value |
|---|---|---|
| Spin quantum number | s | 2 |
| g-factor | $g_1 \dots g_7$ | 2.11 |
| Vertical coupling | $J_{\{2,0\}}$ | 0.7 meV |
| Horizontal coupling | $J_{\{0,2\}}$ | 0.1 meV |
| Diagonal coupling | $J_{\{1,1\}}$ | -0.69 meV |
| Planar anisotropy | $E_1 \dots E_7$ | 0.31 meV |
| Axial anisotropy (atom 1, 3) | $D_1$, $D_3$ | -1.87 meV |
| Axial anisotropy (atom 2) | $D_2$ | -2.42 meV |
| Axial anisotropy (atom 4, 7) | $D_4$, $D_7$ | -1.37 meV |
| Axial anisotropy (atom 5, 6) | $D_5$, $D_6$ | -1.62 meV |
| External magnetic field (z-axis) | $B_z$ | 1.0 T |

**Table 5.1: Base values for calculations of the d-loop states and energies.**

assume that the two effects will have the same $\lambda$ factor in the exponential decay.



$$I(z) = I_0 e^{-\lambda z} \tag{5.6}$$

We can fit the $Z(I)$ curves with Equation 5.6 to evaluate $\lambda$. The $I(z)$ curves of the different atoms, before and after the switch, follow the same exponential decay. The fits gave an average value of $\lambda = (21.9 \pm 0.6)\,\mathrm{nm}^{-1}$ (the current is divided by 10 every 105.15 pm). The incertitude is evaluated by taking the maximum difference between the fitted values and the average value.

Using this value as for the exponential decay of the tip field in Equation 5.5, and the value of 1 Tesla for the switching point of the trimer's atoms ($B^{tip}(37\,\mathrm{pm}) = 1\,\mathrm{T}$), we can evaluate that the tip field causing the switching of the bottom dimer is approximately of -0.25 Tesla (creating a local field of 0.75 Tesla).

### 5.3.2. UNBALANCED STRUCTURE

To try to understand the causes of the unbalance, we used the Heisenberg Hamiltonian model presented previously. We calculated the energies and states of the system under variations of the g-factor ($g_i$), the coupling $J_{i,j}$, the axial anisotropy $D_i$ and planar anisotropy $E_i$, for the atoms 1, 4 and 5. The base values used for the calculations of presented in Table 5.1. Because of the symmetry of the structure, the behaviour of the atoms 6 and 7 will be the same as for the atoms 4 and 5, and atom 3 will behave as atom 1. The atom 2 do not play a role in the imbalance of the structure.

To model the tip field effect, the local magnetic field on atom $i$ ($B_{z,i}$) was sweep from –0.1 T (tip close, high tip field) to 1.0 T (tip far away, no tip field). A constant external magnetic field of 1 T is applied on the rest of the atoms. The effects of the other parameters are modelled by varying only this parameter on one atom at the time.

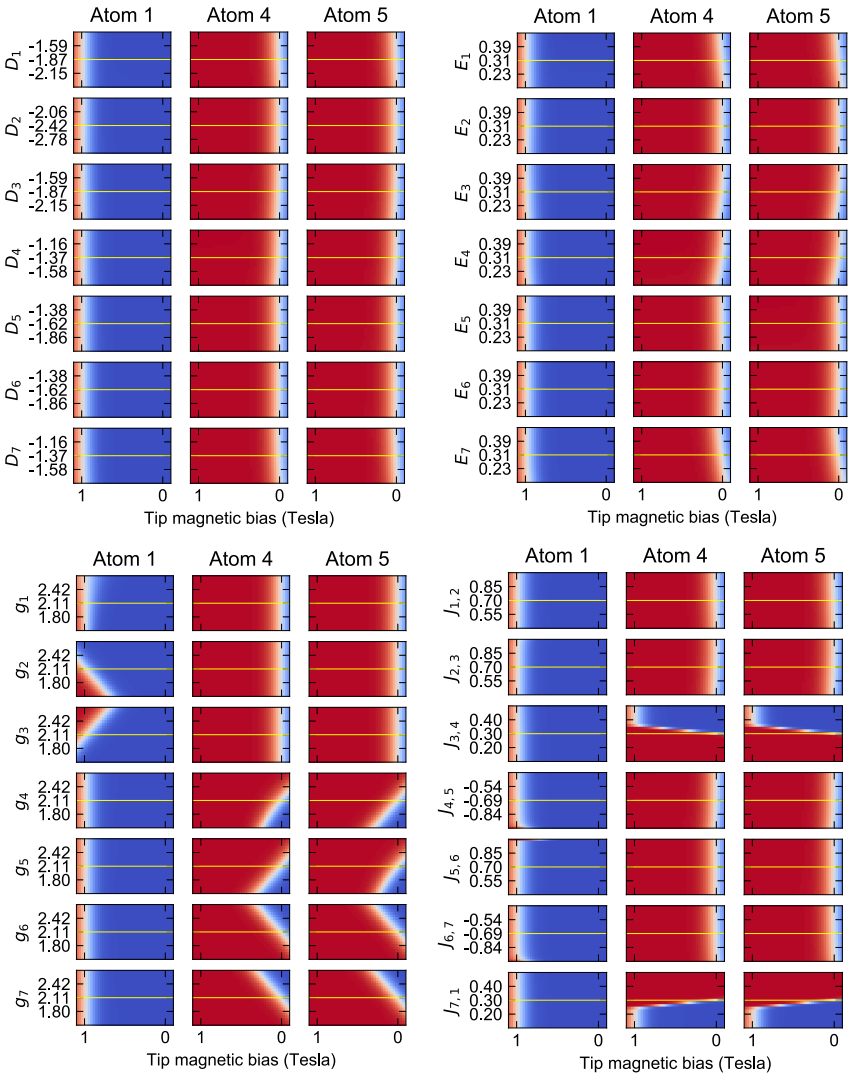


**Figure 5.7: Effect of local variations on the spin states of the loop**. Numerical calculations using a spin hamiltonian model where one parameter is slightly changed(the y-axis on the plots) from its original value (the yellow lines). The variations are done on the axial anisotropy ($D_i$), the planar anisotropies ($E_i$), coupling ($J_{i,j}$) and g-factor ($g_i$) on the spin states of atom 1, 4 and 5. $i$, $j$ correspond to the atom number. A global external field of 1 tesla is present. On the x-axis is the local tip field biasing. A value of 1 tesla of the tip field correspond to an effective local magnetic field of 0 (the tip field fully cancel the external field).

In Figure 5.7, we show the expectation value of the spin along $z$ for the atoms 1, 4 and 5 calculated using the thermal density matrix and the first $N$ energy states, as follows

$$\langle S_{z,n} \rangle = \frac{1}{Z} \sum_{i=1}^{N} e^{-\epsilon_i \beta} \langle \phi_i | S_{z,n} | \phi_i \rangle \tag{5.7}$$

where $Z = \sum_{i=1}^{N} e^{-\epsilon_i \beta}$ is the partition function, $\beta$ is related to the temperature as $\beta = 1/k_B T$, $\epsilon_i$ is the energy of the state $i$, and $|\phi_i\rangle$ is the state $i$ of the system. $N$ was chosen to be high enough that all relevant states are included in the calculation.

A first conclusion that can be drawn for the calculations is that the structure balance is resilient to the variation of the axial anisotropies $D_i$ and planar anisotropies $E_i$. Only slight variations of tip field needed to change the state can be observed and only for the largest variation of the planar anisotropies $E_i$ of the dimers' atoms. Even then, the unbalance remains small. In short, the unbalance caused by the variation of $D_i$ and $E_i$ are too small to explain the previous experimental results.

The situation is different for the g-factor and the coupling $J_{\{0,2\}}$. In both cases, the dimer's atoms act together and the change in states happen at the same tip field for the two atoms. This is coherent with what was observed on the experimental $Z(I)$ curves. The system is particularly sensitive to the variation of the weak coupling $J_{\{0,2\}}$ ($J_{3,4}$, $J_{7,1}$) linking the trimer to the dimers. A local defect in the Cu2N islands structures could lead to the needed deviation.

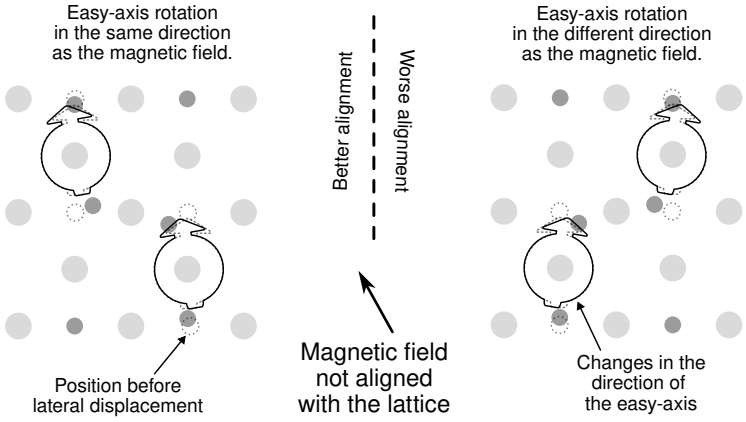


**Figure 5.8: Effect of a rotation of the magnetic field of the easy-axis of the atom's spin**. Illustration of the consequence of a misalignment of the magnetic field relative to the lattice direction combined with a rotation of the easy-axis of the atom's spin resulting from the displacement of the substrate atoms when two absorbed atoms are close. A slight anti-clockwise rotation of the field direction illustrates the misalignment of the magnetic field. In this context, the top dimer (left) easy-axises are rotated in the same direction as the misalignment. This makes a more significant proportion of the field aligned with the easy-axises compared to the bottom dimer (right). In other words, it costs less energy to align anti-align the bottom dimer spins (right) with the field than it costs for the top dimer (left).

Another hypothesis trying to explain the unbalance of the structure would be a difference in the coupling of the trimer with the top dimer and bottom dimer due to the rotation of the easy-axis of the dimer. In a previous study by Bryant & *al.*[28] it was calculated that two Fe atoms on a $Cu_2N$ substrate in a $\{0,2\}$ relative positioning would displace laterally one of the bounded nitrogen atoms. Because the easy-axis direction is due to this bounding, this displacement can change the alignment the easy-axis that will in return import the coupling of nearby spin.

Combining this rotation of the easy axis with a slight misalignment of the external magnetic with the crystallographic direction, the top and bottom dimers will be affected differently, breaking the symmetry of the system. The crystallographic direction of the Cu2N islands makes an angle of approximately 6° with the external magnetic field. This is due to a misaligned of the crystal in the sample holder. This angle makes the projection on the easy-axis of the atoms in the bottom dimer and top dimer different and creates a difference in the magnetic field felt by the atoms, as illustrated in Figure 5.8. The difference in the easy-axis direction could also play a role in the value of $J_{\{0,2\}}$ of the two dimers with the trimer.

5

## 5.4. EXTENDED D-LOOPS

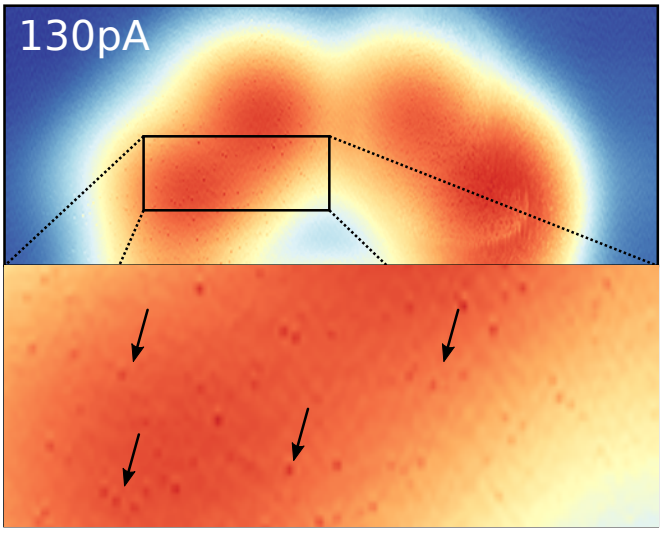


**Figure 5.9: Zoom on the dimers using a spin-polarised tip**. When zooming (bottom image) the dimers (top image) show some quick burst of the current. The arrows point toward some examples of those jumps.

In the previous sections, we observed that it is possible to use the STM tip to bias the local magnetic field and change the preferred spin state of the probed atom. When the tip field fully cancels the local field, for example, in the grey boxes of Figure 5.6, the atom spin-flip rapidly between the ↑ and ↓ states. The lifetime of the states seems different depending on the atoms. Again in Figure 5.6 the switching of the trimer atoms (subplot

(a) and bottom right box of subplot (b)) shows a noisy transition, especially compared to the smooth transition of the bottom dimer (top right box of subplot (b)). This indicates that the trimer have a slower dynamics than the dimer, and that the dimer dynamic is too fast, resulting in a measurement of an averaged value. The fast dynamic can also be observed in Figure 5.9, where we can see a zoomed portion of the dimers during a spin-polarised topographic scan. The points (some examples of these are indicated by arrows on Figure 5.9) are not noise in the signal. We interpret them as sudden short changes of the spin state of the atom. Their localisation exclusively over the atoms indicates that this "noise" can not be seen in the non spin-polarised scans, support that conclusion. Unfortunately, their dynamics are too fast on the d-loop to be measured. However, they can be observed on an extended-d-loop that was subsequently assembled (Figure 5.10, Figure 5.11).

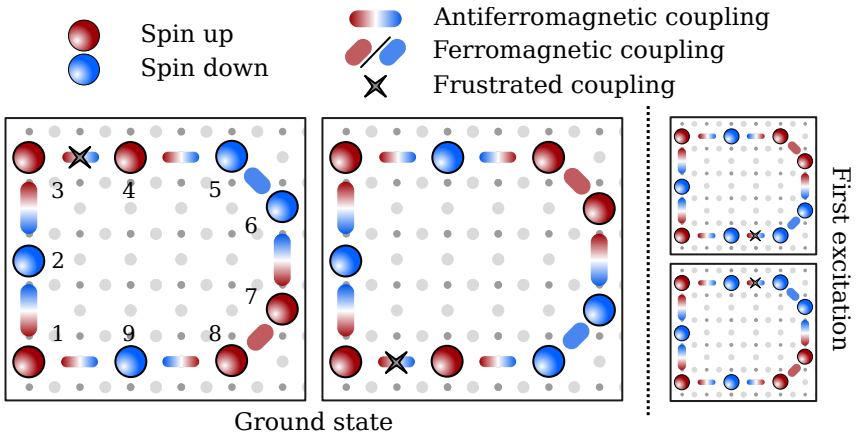


**Figure 5.10: Ball model of the extended-d-loop**. The extended-d-loop includes two more atoms compared to the standard d-loop. Those atoms extend the structure horizontally and add two antiferromagnetic couplings. The frustration will be released on one of the weak antiferromagnetic couplings between 3 and 4 or between 9 and 1.

As discussed in section 5.1, a frustrated loop can be extended by adding an odd number of antiferromagnetic couplings or any number of ferromagnetic coupling without inhibiting its magnetic frustration. The extended-d-loop was designed by adding two atoms between the trimer and the dimers. Here, the two atoms add a total of two weak antiferromagnetic couplings. Consequently, the structure still has one frustrated coupling. The frustration will be released where the cost in energy is the least. This will be in one of the weak $J_{\{0,2\}}$ couplings. However, in the case of the extended-d-loop, if the frustration is release between 4 and 5, or between 8 and 9, that imply that one more spin will be against the external magnetic field. In a first qualitative approximation, this makes it more costly to release the frustration there and the structure only a doubly-degenerated ground state, like the standard d-loop. However, the situation is more complex than in the previous structure as having atoms 4 and 9 in the up state creates three frustrated

couplings (instead of one) and aligns one more spin with the field. This becomes a balance between the coupling strength and the Zeeman energy. We know that at 1 Tesla, the difference in We know the Zeeman energy, but the $J_{\{0,2\}}$ coupling is still uncertain.

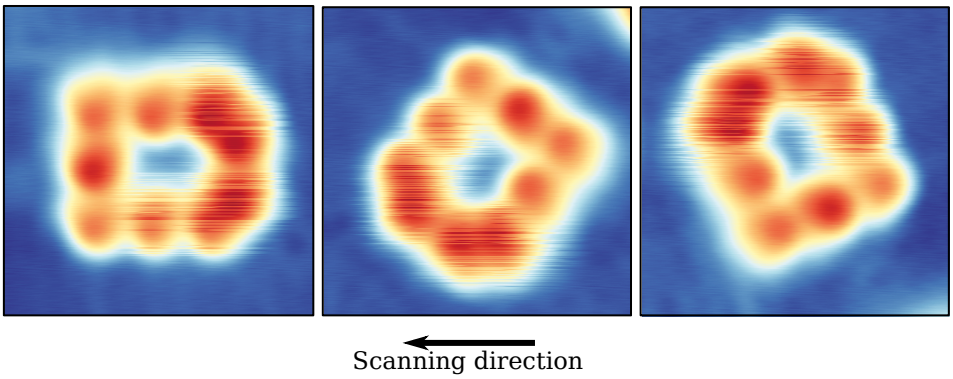




**Figure 5.11: Fast spin polarised scans over an extended d-loop structure at various angles**. The larger d-loop scanned at a high scanning speed in three different directions. The slower switching behaviour of the extended d-loop allows observing the correlation between the spin of the various atoms. It is to be noted that the tip polarisation is inverted relative to the previous scans (the ↑ spin appear lower than the ↓ spin).

The structure was assembled on the same substrate as before. The results of some spin-polarised scans of the structure are shown in Figure 5.11. It is to be noted that the tip's polarisation is different from the previous spin-polarised scans as observed on the trimer. Our previous calculation indicates that the trimer is partly decoupled from the rest of the structure and is in a ↑↓↑ Néel state. This conclusion is still valid for this larger structure. Looking at the trimer, we can conclude that this spin-polarised tip makes the ↓ appear bigger/higher/more conductive than the ↑ state.

The extended-d-loop exhibit a slowed down dynamic, and a longer lifetime of the states can be observed on the scans. The scans in Figure 5.11 were taken at a high scanning speed and at different angles relative to the structure. This allows seeing lines on the scans parallel to the scanning direction. Those are due to changes in the spin state of the underlining atoms. Following the lines, we can observe a correlation between the different spin states of the atoms in the structures. This means that the switching of the state is not only happening locally, one atom at a time, but groups of atoms change state together. In addition to the trimer, atom 4 seems to stay in an ↑ state. The two dimer states seem to correlate strongly together. When one dimer is ↑↑, the other is ↓↓. The behaviour of atom 9 is more puzzling. This atom state correlates with the two dimers' state but in a way that would suggest a ferromagnetic coupling between atoms 8 and 9. This contradicts our initial assumption that the $J_{\{0,2\}}$ coupling is a weak antiferromagnetic coupling. However, this does not invalidate our previous analysis and calculation but will have as a consequence to change the position of the frustrated coupling that was concluded previously. Further studies will be needed to clarify this point.

To observe the effect of the tip field on the switching dynamic, we measured time traces of the current over atoms at different fixed tip height. The traces and their his-

togram for atom 8 are presented in Figure 5.12. The time traces show the current at 4 different heights, going from high current/tip close to the atom/high tip field for the top plot to low current/tip far from the atom/low tip field for the bottom plot. The red values indicate the ↓ state, and the blue the ↑ state. We can see a clear inversion of the state population when the tip is close compared to when the tip is far. When the tip is far, the influence of its magnetic field is minimal, and the atom is mostly in a ↓ state. As the tip go closer, the tip bias the external magnetic field until the point of inversion of the population and where the spin spends most of the time in an ↑ state. We can also conclude from those plots that the tip field enhance the external magnetic field, in contrast with the measurement done on the smaller structure.

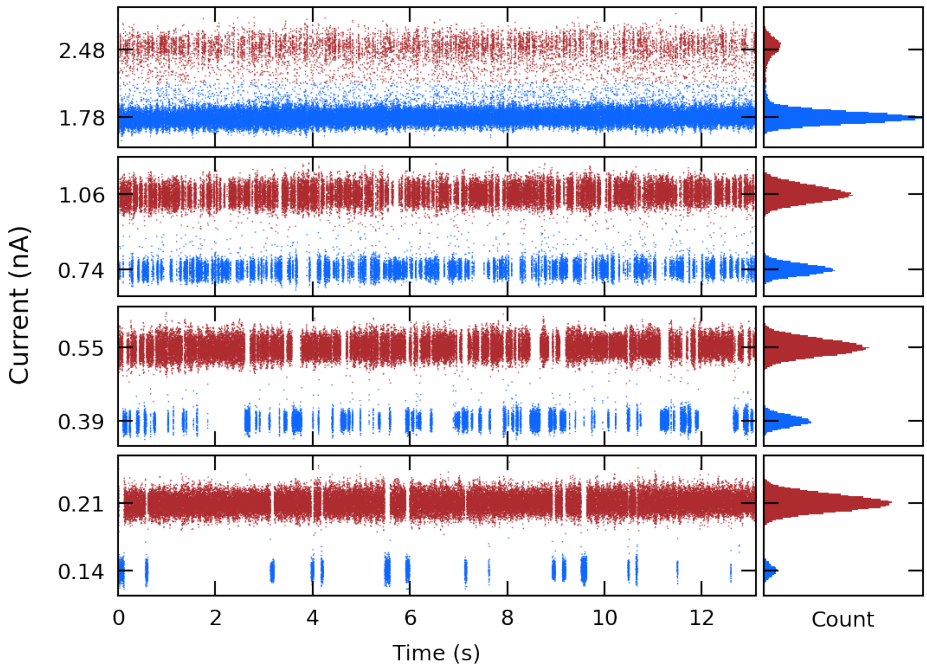


**Figure 5.12: Spin-polarised current time traces at different heights**. The current was recorded on atom 8 (bottom dimer) with the feedback loop inactivated (the tip height is fixed). The four plots were taken at different heights showing the progression of the switching rate and of the proportion of state up and down.

The time traces also allow us to observe a correlation between the state's lifetime and the current. At low current (bottom plots), the atom spend a long (s̃econd) time in the ↓ before switching for a short time to a ↑ state. At higher currents (top plots), even if the atom spends more and more time in the ↑, the lifetime of the state becomes shorter. This indicates that it is the current that drives the switching. For a switch event to occur, multiple electrons need to be involved in the process. The probability that this happens increases with the number of electrons tunnelling through the atom.

## 5.5. CONCLUSION

In this chapter, we have shown the experimental realisation of frustrated closed loops composed of single atoms on a $Cu_2N$ substrate. On that substrate, we assembled two loops: a loop of 7 atoms and a loop of 9 atoms. The structures are subject to magnetic frustration and thus show a high sensibility to perturbation. Experimentally, the smaller loop favour one of the two ground-state configurations and a fast dynamic. Using numerical calculation, we evaluated which parameters could cause the needed perturbation. The structures show switching between their spin states. The tunnelling current drives the switching rate drives, and a high current will result in a higher switching rate and shorter lifetime of the states. The distribution of states is influenced by the tip field and be changed using it.

### 5.5.1. ACKNOWLEDGEMENT

We thank F. Mila for fruitful discussion. This work was supported by the Netherlands Organisation for Scientific Research (NWO) and by the European Research Council (ERC).

5

## REFERENCES

[1] C. Lacroix, P. Mendels, and F. Mila, eds., *Introduction to Frustrated Magnetism*, Springer Series in Solid-State Sciences, Vol. 164 (Springer Berlin Heidelberg, Berlin, Heidelberg, 2011).

[2] A. P. Ramirez, *Strongly Geometrically Frustrated Magnets,* Annu. Rev. Mater. Sci. , 29 (1994).

[3] M. J. Harris, S. T. Bramwell, D. F. McMorrow, T. Zeiske, and K. W. Godfrey, *Geometrical Frustration in the Ferromagnetic Pyrochlore ${\mathrm{Ho}}_{2}{\mathrm{Ti}}_{2}{O}_{7}$,* Phys. Rev. Lett. **79**, 2554 (1997).

[4] L. Balents, *Spin liquids in frustrated magnets,* Nature **464**, 199 (2010).

[5] A. Ortiz-Ambriz and P. Tierno, *Engineering of frustration in colloidal artificial ices realized on microfeatured grooved lattices,* Nature Communications **7**, 10575 (2016).

[6] D. Shi, Z. Budrikis, A. Stein, S. A. Morley, P. D. Olmsted, G. Burnell, and C. H. Marrows, *Frustration and thermalization in an artificial magnetic quasicrystal,* Nature Physics **14**, 309 (2018).

[7] A. A. Khajetoorians, M. Steinbrecher, M. Ternes, M. Bouhassoune, M. dos Santos Dias, S. Lounis, J. Wiebe, and R. Wiesendanger, *Tailoring the chiral magnetic interaction between two individual atoms,* Nat Commun **7**, 10620 (2016).

[8] S. Bhattacharjee, *An introduction to Quantum Spin Liquids,* in *Topology and Condensed Matter Physics*, Texts and Readings in Physical Sciences (Springer, Singapore, 2017) pp. 439–470.

[9] L. Savary and L. Balents, *Quantum spin liquids: A review,* Rep. Prog. Phys. **80**, 016502 (2017).

[10] Y. Zhou, K. Kanoda, and T.-K. Ng, *Quantum spin liquid states,* Rev. Mod. Phys. **89**, 025003 (2017).

[11] Y.-L. Wang, X. Ma, J. Xu, Z.-L. Xiao, A. Snezhko, R. Divan, L. E. Ocola, J. E. Pearson, B. Janko, and W.-K. Kwok, *Switchable geometric frustration in an artificial-spin-ice–superconductor heterosystem,* Nature Nanotechnology **13**, 560 (2018).

[12] J. Gobeil, D. Coffey, S.-J. Wang, and A. F. Otte, *Large insulating nitride islands on Cu3Au as a template for atomic spin structures,* Surface Science **679**, 202 (2019).

[13] T. Choi, C. D. Ruggiero, and J. A. Gupta, *Incommensurability and atomic structure of c2x2 N/Cu100: A scanning tunneling microscopy study,* Phys. Rev. B **78**, 035430 (2008).

[14] T. Choi, C. D. Ruggiero, and J. A. Gupta, *Tunneling spectroscopy of ultrathin insulating Cu2N films, and single Co adatoms,* Journal of Vacuum Science & Technology B: Microelectronics and Nanometer Structures Processing, Measurement, and Phenomena **27**, 887 (2009).

[15] C. F. Hirjibehedin, C. P. Lutz, and A. J. Heinrich, *Spin Coupling in Engineered Atomic Structures,* Science **312**, 1021 (2006).

[16] F. M. Leibsle, S. S. Dhesi, S. D. Barrett, and A. W. Robinson, *STM observations of Cu(100)-c(2x2)N surfaces: Evidence for attractive interactions and an incommensurate c(2x2) structure,* Surface Science **317**, 309 (1994).

[17] S. Loth, S. Baumann, C. P. Lutz, D. M. Eigler, and A. J. Heinrich, *Bistability in Atomic-Scale Antiferromagnets,* Science **335**, 196 (2012).

[18] S. Rolf-Pissarczyk, S. Yan, L. Malavolti, J. A. J. Burgess, G. McMurtrie, and S. Loth, *Dynamical Negative Differential Resistance in Antiferromagnetically Coupled Few-Atom Spin Chains,* Phys. Rev. Lett. **119**, 217201 (2017).

[19] C. D. Ruggiero, T. Choi, and J. A. Gupta, *Tunneling spectroscopy of ultrathin insulating films: CuN on Cu(100),* Appl. Phys. Lett. **91**, 253106 (2007).

[20] A. Spinelli, M. P. Rebergen, and a. A. F. Otte, *Atomically crafted spin lattices as model systems for quantum magnetism,* Journal of Physics: Condensed Matter **27**, 243203 (2015).

[21] A. Spinelli, M. Gerrits, R. Toskovic, B. Bryant, M. Ternes, and A. F. Otte, *Exploring the phase diagram of the two-impurity Kondo problem,* Nature Communications **6**, 10046 (2015).

[22] A. Spinelli, B. Bryant, F. Delgado, J. Fernández-Rossier, and A. F. Otte, *Imaging of spin waves in atomically designed nanomagnets,* Nat Mater **13**, 782 (2014).

[23] R. Toskovic, R. van den Berg, A. Spinelli, I. S. Eliens, B. van den Toorn, B. Bryant, J.-S. Caux, and A. F. Otte, *Atomic spin-chain realization of a model for quantum criticality,* Nat Phys **12**, 656 (2016).

[24] S. Yan, D.-J. Choi, J. A. J. Burgess, S. Rolf-Pissarczyk, and S. Loth, *Control of quantum magnets by atomic exchange bias,* Nature Nanotechnology **10**, 40 (2015).

[25] A. J. Heinrich, J. A. Gupta, C. P. Lutz, and D. M. Eigler, *Single-Atom Spin-Flip Spectroscopy,* Science **306**, 466 (2004).

[26] C. F. Hirjibehedin, C.-Y. Lin, A. F. Otte, M. Ternes, C. P. Lutz, B. A. Jones, and A. J. Heinrich, *Large Magnetic Anisotropy of a Single Atomic Spin Embedded in a Surface Molecular Network,* Science **317**, 1199 (2007).

[27] A. F. Otte, M. Ternes, K. von Bergmann, S. Loth, H. Brune, C. P. Lutz, C. F. Hirjibehedin, and A. J. Heinrich, *The role of magnetic anisotropy in the Kondo effect,* Nature Phys **4**, 847 (2008).

[28] B. Bryant, A. Spinelli, J. J. T. Wagenaar, M. Gerrits, and A. F. Otte, *Local Control of Single Atom Magnetocrystalline Anisotropy,* Phys. Rev. Lett. **111**, 127203 (2013).

[29] D. T. Pierce, *Spin-polarized electron microscopy,* Phys. Scr. **38**, 291 (1988).

[30] M. Bode, *Spin-polarized scanning tunnelling microscopy,* Rep. Prog. Phys. **66**, 523 (2003).

[31] D. M. Eigler, C. P. Lutz, and W. E. Rudge, *An atomic switch realized with the scanning tunnelling microscope,* Nature **352**, 600 (1991).

[32] I.-W. Lyo and P. Avouris, *Field-Induced Nanometer- to Atomic-Scale Manipulation of Silicon Surfaces with the STM,* Science **253**, 173 (1991).

[33] S. Loth, K. von Bergmann, M. Ternes, A. F. Otte, C. P. Lutz, and A. J. Heinrich, *Controlling the state of quantum spins with electric currents,* Nat Phys **6**, 340 (2010).

# 6

# ARTIFICIAL LATERAL CONFINEMENT OF FIELD-EMISSION RESONANCES

*Don't quote me on that...*

Uncertain individual

*Scanning tunnelling microscope (STM) allows the experimental investigation of local field-Emission resonance (FER) caused by image potential states (IPS) bounding the electrons in a plane near the surface. Those states arise when the image charges attract the electrons toward the surface, but a projected band gap or a non-conducting surface prevents them from entering the bulk. On an unsaturated monolayer of CuCl deposed on a Cu(100) crystal, we demonstrate the possibility of further trapping the electrons in-plane by engineering the surface potential. Chlorine molecules are moved using horizontal manipulation to create areas of bare copper surrounded by insulating chlorine atoms limiting the lateral area where the FER can exist on the surface. We observe a shift in the FERs energy compared to bare Cu(100) FER, followed by smaller resonances associated with the higher energy modes of the cavity. Those electronic states show spatial dependence and energies similar to a particle in a box model.*

## 6.1. INTRODUCTION

In this chapter, we report on field emission resonances (FER)[1, 2] exhibiting in-plane confinement inside few nanometers wide square areas of bare copper(100) surrounded by chlorine atoms. We show that the insulting copper-chlorine creates a potential well allowing quantised states populated by the field-emitted electrons. The states behave similarly to a particle-in-a-box model where the different modes can be associated with s-like, p-like and d-like states. We modelled the confinement both out-of-plane and in-plane with custom code implementing a variational method and the Ritz method to solve the time-independent Schrödinger equation using a basis of shifted Gaussian functions. The data taken at different heights show a significant Stark shift of the FER energies supporting the assertion of their vacuum state nature[3, 4]. This energy shift is also observed on the single vacancy resonance around 3.2 V. In previous research on artificial lattices built from those vacancies, this shift was associated with the onset of the conduction band[5, 6]. From the $\mathrm{d}I/\mathrm{d}V$ curves, we can estimate an enhanced lifetime of the electrons in the confined states compared to the FER on bare Cu(100).

Section 6.2 give an overview of the theory surrounding image potential states (IPS), field emission resonances and their experimental observations on Cu(100) with and without a chlorine layer. The laterally constrained FER experimental observations are presented and analysed in the section 6.3. In section 3.4, the models used to describe the potential between an STM tip and a sample in the context of FER are presented and the numerical methods used in the simulation and analysis is explained. This section is followed by a short conclusion in section 6.5. The experimental materials and methods were introduced in chapter 2.

We note that the Hartree atomic units' system is used during the calculation and, unless stated otherwise, the equations in the following chapter are also written using this system of units. In short, the unit system is based on setting the reduced Planck constant ($\hbar$), the elementary charge ($e$), the Bohr radius ($a_0$) and the electron mass ($m_e$) to unity. In atomic and molecular physics, this system simplifies the notation and limits some numerical complication that can arise with an ill-fitted unit system, notably overflow and underflow problem that could occur with exponential.

## 6.2. IPS & FER

Image potential states (IPS) are electronic states that are observed above certain surfaces and interfaces. The states' wavefunctions exist mostly outside the solid, extend up to a couple of nanometers (1-3 nm) away from the surface, and die out quickly inside the bulk. They appear when the electrons are attracted by their image charges inside the surface but cannot enter the bulk because the surface exhibits a projected bandgap or is insulating. IPS were first observed using photoemission spectroscopy, where they manifest as apparent energy bands inside the gap, just below the vacuum level [7–10]. A variation of these states is found in scanning tunnelling microscopy (STM) where the proximity of the probe tip alters the confinement potential by the combined effect of the tip image potential[2, 11] and the difference in chemical potential between the two

metals [12, 13]. This increases the energy of the IPS and can brings some of them above the work function of the surface. This allows field emitted electrons to populate those states[12] and creates characteristic spikes at the states' energy in the $\mathrm{d}I/\mathrm{d}V$ spectrum. Those characteristic energies are called field emission resonances.

The field-emission regime can be viewed as another mode in which an STM can operate and, in those conditions, is closer to the original topografiner by Young *et al.*[14]. This allows new experiments with an STM, notably the possibly to scan over insulting surfaces[15] and, as the exact sequence of FER states and their associated energies are material-specific, FER spectroscopy can be used for verifying the composition of the surface [16, 17], as well as for determining the local work function [18–20].

On a clean and continuous surface, the IPSs are isomorphic in the lateral (in-plane) direction and do not confine the electrons or hinder their movements, *i.e.* the electrons in an FER propagate parallel to the surface mostly like free electrons[9, 21, 22]. However, inhomogeneities in the surface or contaminants can disturb the potential and cause dispersion and lateral confinement of the resonances. This kind of effect was observed near step edges [23–25], domain walls [26], as well as on nanoislands [27, 28], nanowires[29], quantum dots[30], and atomic clusters [31, 32]. More detailed theoretical background on FER and IPS can be found in chapter chapter 2.

In this work, we use atom manipulation [33] to engineer lateral confinement for the IPS states. By creating atomically precise rectangular confinement areas, we create a new set of resonances, the wavefunctions of which can be mapped and identified as particle-in-a-box states. The ability to engineer such well-defined quantum dots is of particular interest in view of recent STM experiments concerning artificial electronic lattices [5, 6, 34–36].



### 6.2.1. FER OVER CU(100)

The Cu(100) surface exhibits a projected bandgap around the vacuum energy; more precisely, there is a bandgap in the $\Gamma_x$ direction in the k-space that extends between -2.79 eV and +3.31 eV[37], 0 eV being the vacuum energy for Cu(100). Consequently, IPS can exist above the Cu(100) surface which was the subject of many publications related to IPS between 1983 and 1987 using inverse photoemission[7, 8], momentum-resolved photoemission [9] and two-photon- photoemission[21]. In addition to the pristine Cu(100) surface, the ClCu/Cu(100) surface was also studied in the same period[9, 38, 39]. The chlorine layer was notably used to establish that the observed phenomenon was indeed IPS[9]. This evidence comes for the difference in the IPS' energy between the Cu(100) and ClCu/Cu(100) IPS matching the difference in work function between the two surfaces, ruling out other possible causes. This shift in energy due to the difference in work function was also observed on oxygen covered Ni(100) and gold-covered Si(111)[1]. In addition to the experimental works, theoretical studies gave a solid theoretical background to the phenomenon, notably on the potential shape[11], the role of the bandgap[10] and the distance of the image plane[37, 40].

The observation of FERs on Cu(100) came a bit later, but the capacity of the STM

to distinguish nanometers scale changes on the surface showed the presence of FER standing waves parallel to the surface near step edges[23]. That result demonstrated the STM's capacity to observe changes of the FER 2D electrons gas when disturbed by local geometry and contaminants. The effective mass of the electrons gas, evaluated at $m'/m_0 = 0.9 \pm 0.1$[23], is similar to the one measured on a free surface ($1.2 \pm 0.2$[9], 0.9[41]) and indicate that the electrons move freely parallel to the surface even under an STM. The first FER on Cu(100) is observed at 4.7 eV at 100 pA[23] and 4.8 eV at 300 pA[31]. The energy of the first FER seems to be only slightly affected by the tip shape[23, 31]. The higher energy FER ($n > 1$) are more affected by the tip shape and, depending on the tip geometry, the number of FER observed between 4 V and 9 V can vary between 4 and 8[31]. This dependence on the tip shape can be explained by the validity of the flat tip model at close distance and low bias voltage and will be discussed in more detail in section 3.4. The independence of the tip shape on the first FER's energy allows it to be used to identify surfaces chemically[16] or to evaluate the local work function[18].

## 6.3. LATERALLY CONFINED FER

FERs on pristine surface propagate parallel to the surface, analogous to free electrons[9, 21, 22], and thus their movement is not hindered in the lateral (in-plane) direction. However, on inhomogeneous surfaces, the morphology and contaminants can cause lateral disruption and confinement of the resonances. This was observed near step edges [23–25], domain walls [26], nanoislands [27, 28], nanowires[29], quantum dots[30], and atomic clusters [31, 32]. In these experiments, the confinement appears near absorbates, or plateaux, and is due to a difference in the work functions. It was theoretically shown that to observe confinement of FERs, a lower work function of the adsorbate than the substrate and a projected bandgap of the substrate are sufficient conditions[42].

To engineer the lateral confinement of the FERs, we used atom manipulations[33] on a chlorine-terminated Cu(100) surface (ClCu/Cu(100)) and created atomically precise rectangular bare Cu(100) areas surrounded by a continuous insulating layer of ClCu. The CuCl/Cu(100) surface allows reliable manipulation of the individual chlorine atoms and vacancies, and as such, offer an excellent platform for large scale atomic assembly[43]. We designate the assembled areas as patches and label them using the nomenclature $N \times M$, where $N$ and $M$ correspond to the number of ClCu unit cells on $x$ and $y$ sides of the rectangular area (0.36nm/unit cell). We focus our work on square patches ($N \times N$). Figure 6.1 shows the patches used in this work. We assembled them so that neighbouring patches are separated by at least 8 unit cells of uninterrupted chlorine, and as such, are considered isolated from each other. When imaged at typical tunnelling conditions (*e.g.* 600 mV, 300 pA in Figure 6.1), the larger patches appear brighter (higher) due to the increased conductivity of the metal compared to the chlorine, despite the Cu surface being physically ~0.23 nm[38] lower than the CuCl surface. The relative apparent height depends on the bias voltage used.

Inside the patches (Figure 6.7), we observe FERs, but their energies are shifted upward compared to Cu(100) FER. Usually, the FERs consist of pronounced peaks in the differential conductance spectra. Here, the main peaks are present, but smaller sub-

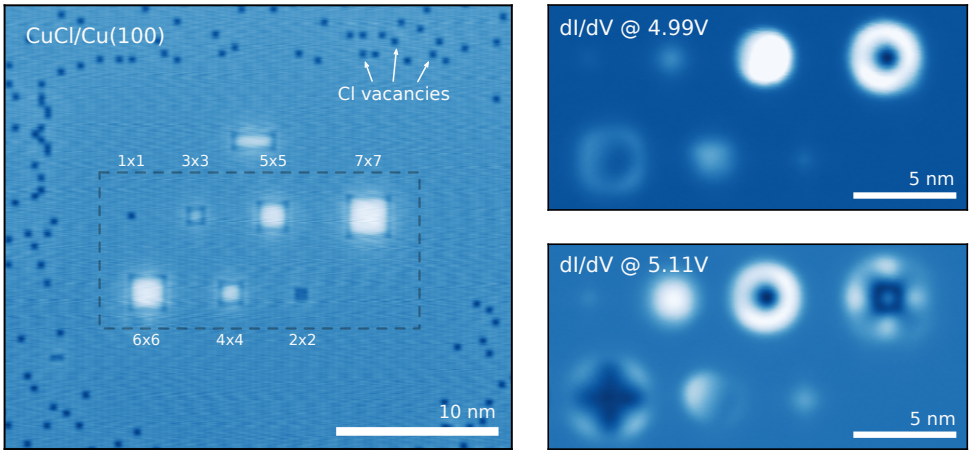


**Figure 6.1: Topography and c.c. $\mathrm{d}I/\mathrm{d}V$ maps of the CuCl/Cu(100) patches.** (left) Topography of the patches taken at a constant current of 300 pA and a bias voltage of 600 mV. Arrows indicate some chlorine vacancies. We formed the larger square area of bare Cu(100) in the centre by moving and assembling multiples of these vacancies. Their size in terms of chlorine vacancies is indicated above or under each of the square patches. (right) The same area as the dashed grey rectangle on the right image, but showing the dI/dV measurement at two different bias voltages, taken at 200 pA.



peaks accompany them (Figure 6.6). The peaks and their subpeaks vary in intensity inside the patches and can be mapped to well-defined wavefunctions of particle-in-a-box states (Figure 6.9). The states are not strictly confined to the limits of the patches but can extend over the chlorine layer, potentially opening the door to engineered coupling between patches.. The ability to engineer such well-defined quantum states is of particular interest in view of recent STM experiments concerning artificial electronic lattices [5, 6, 34–36, 44].

### 6.3.1. LIMIT CASES: FER ON CUCL/CU(100) AND CU(100)

As we are going to be exploring the effect of lateral confinement of the FER on square patches, it is useful to start by looking at the limits: a pristine Cu(100) layer and a continuous CuCl layer. Figure 6.2 shows the c.c. $\mathrm{d}I/\mathrm{d}V$ taken at a constant current of 100 pA between 2 V and 9 V on a continuous CuCl/Cu(100) layer. Two references values for the position of the resonances on Cu(100) are compiled in Table 6.1: from Wahl *et al.*[23] taken at 100 pA and in from Stepanow *et al.*[31] taken at 300 pA. Both authors specified that the number of FER observed in that range and their energies depend on the shape of the tip, especially at higher energy, but that the energy of the first FER (around 4.7 eV) is quite resilient to changes in the tip morphology.

In IPS experiments involving a single surface and a vacuum, like 2PPE, unlike STM, the energies of the IPS are pinned to the vacuum level[9], *i.e.* a difference in work function will be translated into a similar difference in IPS energy. This relation was notably used to establish the nature of observed phenomena as IPS. In an STM, the presence of

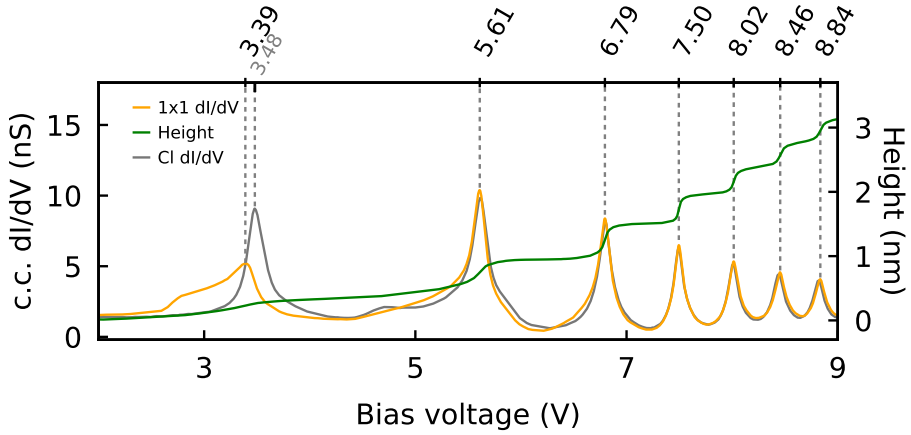


**Figure 6.2: c.c. $\mathrm{d}I/\mathrm{d}V$ spectroscopy on the CuCl/Cu(100) layer and in a single vacancy**. The spectroscopies are taken at a constant current of 100 pA. The green curve shows the tip height recorded simultaniously during the measurement of the c.c. $\mathrm{d}I/\mathrm{d}V$ inside the 1×1 (yellow curve). In grey is the c.c. $\mathrm{d}I/\mathrm{d}V$ on a continuous layer of chlorine on Cu(100). Above the plot are indicated peak positions for the two c.c. $\mathrm{d}I/\mathrm{d}V$ . Except for the first peak at 3.39 V, there is no difference in the peak positions between the single vacancy (1×1) and the continuous layers of chlorine.

| Ref. | Setpoint | Energy ±0.05 (eV) | | | | |
|---|---|---|---|---|---|---|
| Wahl[23] | 100 pA | 4.75 | 6.20 | 7.15 | 8.00 | |
| Stepanow[31] | 300 pA | 4.80 | 6.22 | 7.21 | 7.92 | 8.60 |

**Table 6.1: References values for FER on Cu(100)**.

the tip, its morphology, and its (possibly changing) distance from the surface will affect this relation.

On the CuCl/Cu(100), the first resonance is present at 3.5 V, as seen on Figure 6.2. Its shape is slightly different from the following resonances, and its height does not follow the same trend. We attribute those differences to the energy being below the threshold energy needed for field emission, and as such it is technically not an FER. Additionally, the tunnelling electrons play a significant role in the measured current at this distance from the sample for the first IPS. These two effects are not true for higher energy IPS, as the energy is above the work function and the tip is far away from the surface. We nonetheless attribute this resonance to IPS because of its measurable Stark-shift, discussed below, the effect of the presence of vacancies on the resonance, discussed in subsection 6.3.2, and the numerical calculation, in section 3.4.

The data presented in Figure 6.2 for the Cl layer was taken at a constant setpoint of 100 pA, meaning that the system adjusts the tip-sample distance as the bias voltage changes to keep the current constant. The changing distance between the tip and the

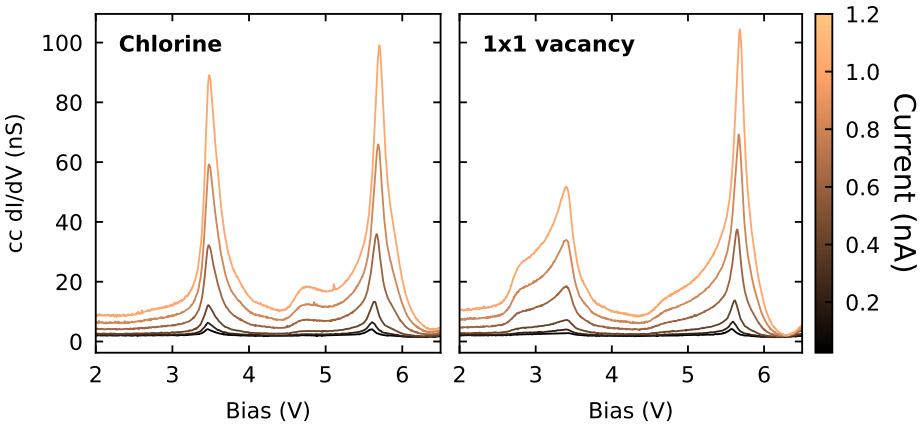


**Figure 6.3: Multiple c.c. $\mathrm{d}I/\mathrm{d}V$ taken on the chlorine layer (left) and in the middle of a single vacancy (right).** All the spectroscopies were taken consecutively with the same tip. The change in the peak positions due to a change in the current setpoint for the different patches can be seen in Figure 6.11.

sample will, in return, change the shape of the electrostatic potential. Figure 6.3 shows spectra taken at setpoints ranging between 1 pA to 1 nA on the Cl layer. The figure shows shift of the resonance position as a function of the setpoint, and thus as a function of the electrostatic potential. Figure 6.11 shows the extracted values of this shift in energy. This phenomenon is known as Stark-shift and indicates that the feature corresponds to IPS rather than the conduction band, which should be insensitive to changes in the tip-sample distance.

The difference in work function between the CuCl/Cu(100) and Cu(100) surfaces is $1.1 \pm 0.2$ eV[9], and so the equivalent of the first resonance on CuCl/Cu(100) should be observed around 2.4 V on Cu(100). This is below the projected bandgap of the Cu(100) surface[9, 37, 45] preventing the IPS from forming. Over the CuCl/Cu(100) the insulating chlorine layer acts as the containing potential preventing the electrons from entering the surface. The difference in energies between the resonances on CuCl/Cu(100) and Cu(100) are shown in Figure 6.4. As the energy rises, the difference between the two surfaces disappear almost completely. We hypothesise that this discrepancy is caused by the CuCl layer becoming transparent to high energy electrons, combined with the distortion of the potential due to the tip shape and its changing distance to the surface. However, the differences have a linear relationship that can be extrapolated to approximate the work function difference at low energy.

### 6.3.2. FIRST FER OF CLCU/CU(100)

In previous works using atomic manipulations on CuCl/Cu(100) to create structures[43] and engineer the electronic landscape of the surface [5, 6, 44, 46], the vacancies were kept isolated and were not in contact with each other during and after the manipula-

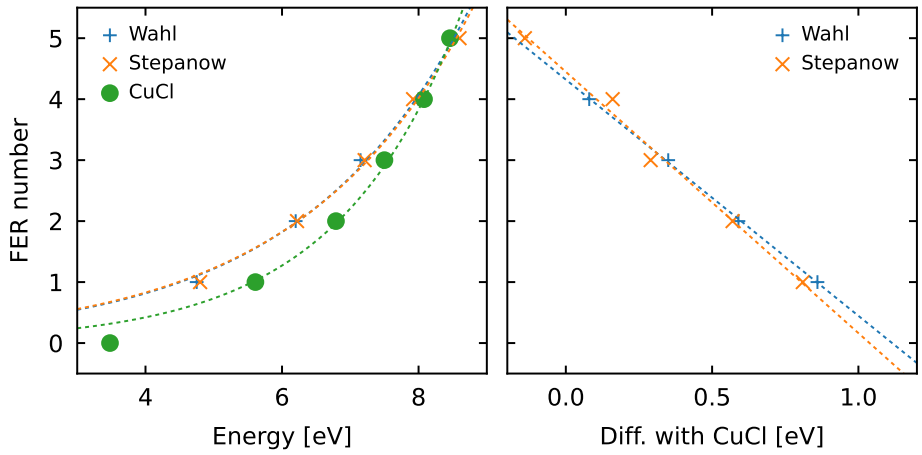


**Figure 6.4: Experimental CuCl/Cu(100) FER vs. references values for Cu(100).** (left) The experimental CuCl/Cu(100) values of the resonance peaks (green circle) are plotted with the references values from Wahl[23] and Stepanow[31]. (right) The difference of the resonances values between the experimental CuCl/Cu(100) and the references Cu(100) values.



tion. This prevents the coalescence of two vacancies as it is laborious and often destructive to separate them. In addition, the states at 3.5 eV used to engineer the electronic landscape disappear when multiple vacancies are bunched together. This is shown in Figure 6.5 where spectra taken along lines crossing the centre of patches of various sizes are displayed. The way that the single vacancy (1×1) affect the resonance at 3.5 eV is fundamentally different compared to larger patches in three ways: the elimination of the resonance on larger patches, the shift in energy and the extent of the resonance.

A single isolated vacancy disturbs the first resonance observed on the chlorine layer. In Figure 6.2 we show a comparison between the c.c. $\mathrm{d}I/\mathrm{d}V$ at 100 pA taken on the chlorine layer and in the centre of a chlorine vacancy (*i.e.* 1×1). On the chlorine layer, the first peak is situated at $3.48 \pm 0.02$ V. When measuring inside a chlorine vacancy, this peak is shifted down by 0.09 V to $3.39 \pm 0.02$ V, and its intensity is reduced. The energy shift is not the only observable effect. The peak shape is also broader and elongated toward lower bias voltage. This resonance is not observable inside bigger patches. It can barely be detected on the 2×2 patches and the detection can be attributed to the imperfect point measurement of the tip, *i.e.* part of the tip is over the chlorine layer.

To further understand the resonance's behaviour, we measure multiple spectra inside the patches and over the chlorine forming a line crossing the patches in the centre. The data in Figure 6.5 show that the single vacancy's effect on the first IPS of the Cl extends outside of the vacancy and into the Cl layer. An energy shift is still distinguishable at more than 1 nm away from the vacancy centre, corresponds to approximately three chlorine lattice constants away. When repeating the same measurement on larger clusters of vacancies, we observe no shift in energy and no spatial extent outside the patch

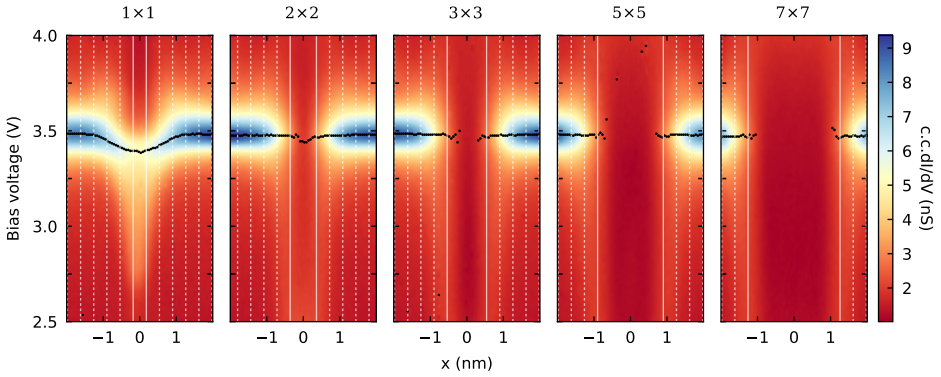


**Figure 6.5: First CuCl/Cu(100) FER on the 1×1 and its suppression on larger patches.**. c.c. $\mathrm{d}I/\mathrm{d}V$ along a line crossing a single vacancy (leftmost) and larger square vacancies patches. The solid vertical line indicates the limits of the patches, and the thin dashed vertical lines indicate the chlorine lattice (0.36 nm). The black dots are detected peaks for each along a vertical line.

limits. The Cl resonance dies out as soon as the tip is over the Cu(100).

The first peak observed on the Cl layer has been previously interpreted as the onset of the conduction band[6], and the shoulder as a localised state split off from the conduction band. In this work, we interpret the former as an IPS and the latter as originating from electrons plane wave scattering on the vacancies, based on the observations discussed above. The resonance occurs at an energy of 3.5 eV, giving the electrons a wavelength of ≈0.66 pm. This is a little more than double the size of a vacancy and approximately the size of a 2×2. This suggests that the vacancy acts as a scattering point for the IPS electrons.

The spatial extent of scattering of the first resonance by the single vacancies is large enough that two separated but close enough vacancies will experience an overlap of their states. This overlap led to the observation of bounding and anti-bounding states with vacancies separated by one and two chlorine atoms[6]. It also allows the engineering of artificial crystal lattices demonstrating the emergence of quasiparticles[5], and topological-states[6].

### 6.3.3. SQUARE PATCH'S FERS

The spectra taken inside the patches show multiple FERs peaks accompanied by new features observable between the major resonances. This is illustrated in Figure 6.6 where the spectra taken in the centre (blue) and off-centre (orange) of a 7x7 patch can be compared to a spectrum on the CuCl/Cu(100) surface. A sharpening of the features is observed; the broad symmetric peaks observed on the extended surface are replaced by sharp asymmetric features and shifted to higher energies when compared to the FER energies on Cu(100). Additionally, several peaks appear in between the major resonances, especially in the off-centre spectrum. These additional resonances belong to a series

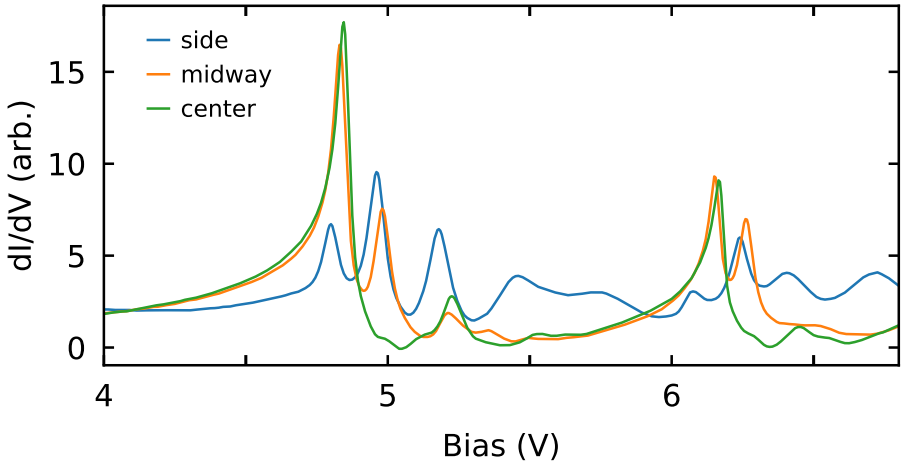


**Figure 6.6: c.c. $\mathrm{d}I/\mathrm{d}V$ of the 7×7 patch showing additional spatial dependent features.** All the spectroscopy curves were taken at 100 pA inside the 7×7 patch but at different positions. The spectroscopies were taken in the middle of the edge between the patches and the chlorine layer (side, in blue), in the centre of the patches (centre, in green) and midway between the centre and the side (midway, in orange). We can see the variation in the observed resonances and the similitude between the ones around 4.8 V and the ones around 6.2 V.



of sub-resonances following each primary FER, but can take complex shapes, especially off-centre.

It is informative to examine the data shows in Figure 6.7. The plots highlight the spatial structure of the resonances, showing symmetric patterns that repeat for each series. The energies at which each features series appear are size-dependent, going from near the energy of the second Cl FER at 5.47(2) V for the 2×2, down to just above the first Cu(100) surface FER at 4.83(3) V for the 7×7. Higher energy series follow a similar pattern, starting at the energy of the corresponding state for the Cl layer and decreasing in energy with increasing patch size. We can also see that the spatial extent of the states is not limited to the patches but leak over the chlorine layer. This is similar to what was observed on the 1×1 patch but, contrary to the 1×1, the progression from the Cl resonance to the patch resonances are discrete and well resolved. These differences point toward a different mechanism for the existence of the states.

The nodal structure of the sub-resonances — which can be resolved for each primary FER, up to and including the fourth primary resonance on 7×7 — begin, at lower energy, by a large central resonance followed by two smaller lobes on each side, followed by two nodes with a small centred node. This pattern hints at the engineered lateral confinement causing it and that the electrons are trapped particle-in-a-box states.

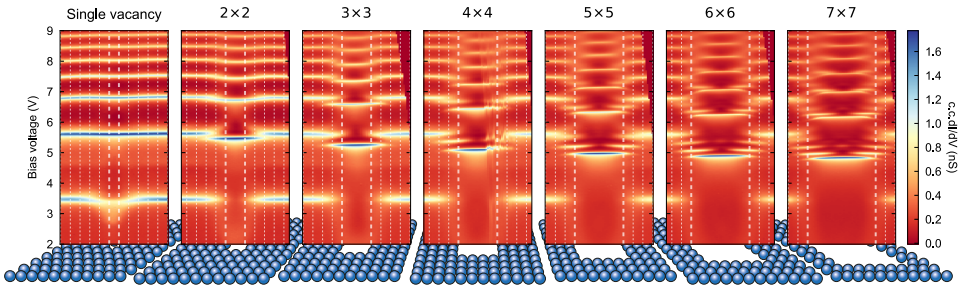


**Figure 6.7: Full (2V-9V) c.c. $\mathrm{d}I/\mathrm{d}V$ along lines crossing the patches.** c.c. $\mathrm{d}I/\mathrm{d}V$ along lines crossing the square patches of chlorine vacancies. The dimensions of the patches are indicated at the top of each plot and the patches are illustrated at the bottom. Each plot is constituted of 75 c.c. $\mathrm{d}I/\mathrm{d}V$ at 100 pA between 2 V and 9 V along a horizontal line crossing the center of the patches. The thick vertical line indicates the limits of the patches, and the thin dashed vertical lines indicate the chlorine lattice (0.36 nm). A correction post-experiment was applied on the data to rectify a tip effect that shifted the data to the right at high voltage biases. This correction is visible as a uniformly red area on the top right of each plot (see section 3.4). *Note on for the* 4×4 *patch*: STM scan on the 4×4 patch after the measurement shown that a chlorine atom moved. This caused the disturbance observes on the 4×4 data. The Cl/Cu(100) substrate is stable at cryogenic temperature, but can be affected by a local defect, high voltage or current.



### 6.3.4. PARTICLE IN A BOX

The structure of the resonances can be understood by considering that the electrons act as a particle in a box, where each series of resonances is associated with a FER mode, denoted as $n = 1, 2, 3, \ldots$, and the sub-resonances of each FER mode are associated with the mode of the particle in a box, denoted as $m = 1, 2, 3, \ldots$. Together we will note $(n, m)$ for the resonance corresponding to the $m-$th particle in a box mode of the $n-$th FER mode.

The modes and energies of the resonances observed in Figure 6.7 are compiled in Table 6.2. To extract that information, we used an algorithm of peak detection to precisely detect the resonances and their energy. The uncertainties are estimated by considering the energy variation for the same resonance, in addition to a correction to take account of the tip height variation. The effect of the tip distance on the measurement is discussed in subsection 6.3.5. Take note that the table does not include values for the mode $m = 3$ because the wavefunction amplitude is zero along the line crossing the patch for this mode. This mode can be observed in the c.c. $\mathrm{d}I/\mathrm{d}V$ map of the patches in Figure 6.9 and will be discussed in subsection 6.3.4.

A simple calculation of an electron in a 7×7 (2.485 nm × 2.485 nm) square potential with infinite potential walls give an energy value of ~0.12 eV for the ground state (see Equation 3.55). If we consider that the energy of the bottom of the well corresponds to the first FER energy of Cu(100), this gives a value of ~4.87 eV for the resonance $(1, 1)$. This approximation is in good agreement with the experimental values measured for the 7×7 patch. The same calculation can be done for the 6×6, 5×5 and 4×4 patches with similar agreements but diverge for the smaller ones and at higher excitations. The results

| Mode | | Patch size | | | | | |
|---|---|---|---|---|---|---|---|
| n | m | 2x2 | 3x3 | 4x4 | 5x5 | 6x6 | 7x7 |
| 1 | 1 | 5.47(2) | 5.25(2) | 5.09(2) | 4.98(2) | 4.89(2) | 4.83(3) |
| | 2 | | | 5.40(2) | 5.23(3) | 5.09(3) | 4.98(2) |
| | 4 | | | | 5.54(2) | 5.36(4) | 5.21(4) |
| | 6 | | | | | | 5.47(3) |
| 2 | 1 | 6.72(2) | 6.58(2) | 6.42(2) | 6.32(3) | 6.23(4) | 6.15(6) |
| | 2 | | | 6.68(2) | 6.49(2) | 6.37(3) | 6.27(3) |
| | 4 | | | | | 6.60(16) | 6.70(5) |
| 3 | 1 | 7.43(2) | 7.34(2) | 7.22(2) | 7.12(4) | 7.04(7) | 6.98(2) |
| | 2 | | | | 7.28(16) | 7.15(2) | 7.04(4) |
| 4 | 1 | 7.97(2) | 7.88(2) | 7.79(2) | 7.71(4) | 7.64(4) | 7.58(2) |
| | 2 | | | | | 7.72(8) | 7.63(3) |
| 5 | 1 | 8.41(2) | 8.35(3) | 8.25(2) | 8.19(4) | 8.12(3) | 8.08(5) |
| 6 | 1 | 8.80(2) | 8.75(4) | 8.66(2) | 8.59(3) | 8.55(2) | 8.49(4) |

**Table 6.2: Measured FER energies**. Energy of the FERs extracted from the data in Figure 6.7 with a peak detection algorithm. The n-mode correspond to the major Cu(100) FERs that are shifted due to the presence of the patches. The m-mode are the additional FER excitations caused by the patches confinement. The value in parenthesis are the uncertainty on the last digits.



of these calculations are shown in Figure 6.8. The figure also shows results from a finite potential models that more closely follows the experimental results, especially at higher energy. In the finite model, we fixed the height of the potential well by considering that an electron reaching the energy of a chlorine FER can travel in the vacuum along the surface and thus is no longer confined, *i.e.* the energy of the measured FER on CuCl/Cu(100) set the top of the potential. This can also be understood as the infinite patch limit case, *i.e.* bare Cu(100). The details of the models and calculations are discussed in section section 3.4.

In order to fully appreciate the spatial distribution of the patch resonances and visualise the structure of the confined modes not only on a line but on the complete area on the patches, we measured multiple constant-current differential conductance maps of the patches. Experimentally, acquiring differential maps proceed differently than c.c. $\mathrm{d}I/\mathrm{d}V$ point spectra. In c.c. $\mathrm{d}I/\mathrm{d}V$ point spectra, the tip is position at a precise position and the bias voltage is swept continuously. This allows a fine granularity of the bias voltage values. For c.c. $\mathrm{d}I/\mathrm{d}V$ maps, it would not be practical to acquire this kind of dense data at each point of a 2D map, and we trade the energy precision for spatial precision. Each map is taken with constant bias voltage, and for the current dataset, we took c.c. $\mathrm{d}I/\mathrm{d}V$ at an interval of 0.025V. A sample of the resulting topography is shown in Figure 6.1. In the figure, we can see the patches size dependency on the observed resonances spatial distribution.

The data from Table 6.2 give us some specific bias voltage values to look at and observe the spatial distribution of the states. As previously mentioned, some states could

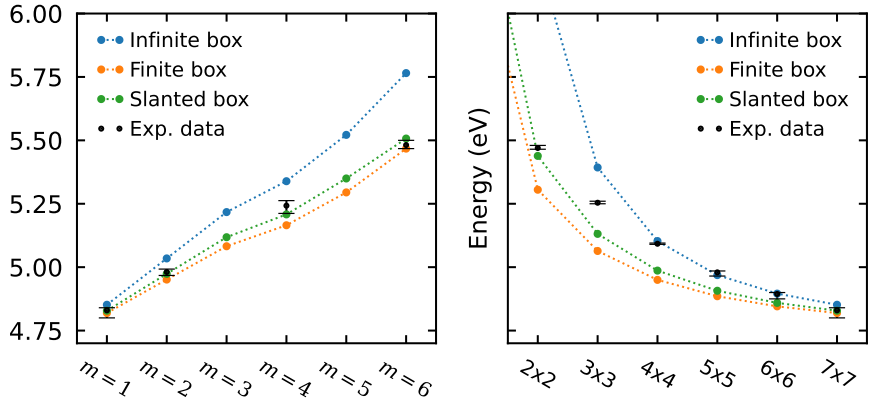


**Figure 6.8: Comparison of the experimental energy values of the resonances with the numerical calculations using different models.** (left) Energies of the main resonance and for the sub-resonances for the first vertical mode ($n = 1$) of the 7×7 patch. (right) Energies of the main resonances for the different patch sizes. The experimental values are extracted from the lines spectroscopies in Figure 6.7.

not be seen on the line spectroscopies, so we relied on the value given by the calculations to find the missing energy values. In addition, to be able to visualise the states at more precise values than the limited granularity of the bias voltage sweep allow, we interpolated the c.c. $\mathrm{d}I/\mathrm{d}V$ maps.

In Figure 6.1 is shown those conductance maps the various sub-resonances of the first FER ($n = 1$) over the 7×7 patch and compared with the corresponding numerical results. The observed states can be clearly recognised as two-dimensional particle-in-a-box modes. They can be characterised by the quantum numbers $m_x$ and $m_y$, which indicate the number of anti-nodes in the horizontal and vertical directions, respectively. The lowest energy state ($m = 1$), coinciding with the primary FER at 4.83 V, corresponds to the $(m_x, m_y) = (1,1)$ mode. This state is followed by the degenerate $(2,1)/(1,2)$ modes at 4.97 V ($m = 2$), the $(2,2)$ mode at 5.11 V ($m = 3$), the degenerate $(3,1)$ and $(1,3)$ modes at 5.20 V ($m = 4$), and so forth. As expected, the $m = 3$ and $m = 5$ modes have nodal planes across the middle of the patch, and thus cannot be detected in point spectroscopy performed along this nodal plane, as is in the case for spectra shown in Figure 6.2 and Figure 6.7.

One important experimental observation that the numerical calculations could not reproduce is the spatial extent of the resonances. In Figure 6.9 the black squares show the physical limits of the patch. In the experimental values, we can see that a significant part of the resonances is measured outside of the patch. The calculation were not able to reproduce this observation. However, further study by R. Rejali *et al.*(to be published) solve this discrepancy using a renormalisation of the data. After renormalisation, the resonances are limited by the patch dimension. The details of that work are beyond the scope of this work.

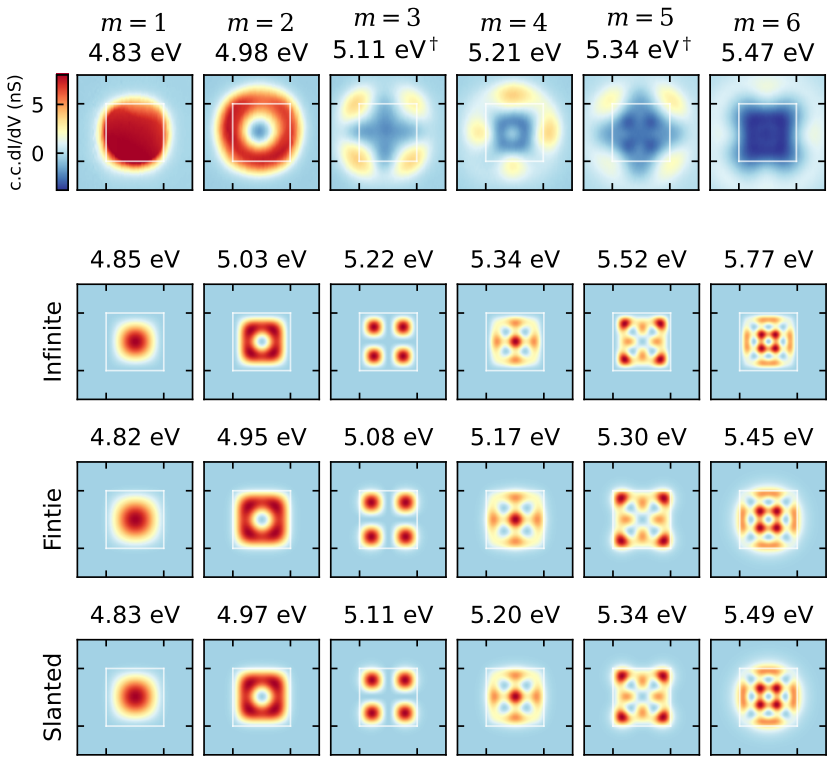


**Figure 6.9: Experimental and numerical c.c. $\mathrm{d}I/\mathrm{d}V$ maps for the $n = 1$ states of the 7×7 patches**. The experimental c.c. $\mathrm{d}I/\mathrm{d}V$ maps (top row) show the spatial distribution of the first 6 states of a 7×7 patch. The following row show the same states calculated with different models. The ticks on the side of each image indicate the limits of the patch. Above each image is the associated state's energy. The experimental energy value for the mode $m = 3$ and $m = 5$ were not detectable on the line spectroscopy (see Figure 6.7) so the value of the slanted model numerical results were used. The experimental c.c. $\mathrm{d}I/\mathrm{d}V$ maps were taken at intervals of 0.025 V and interpolated to find intermediate values.

### 6.3.5. EFFECT OF THE TIP SAMPLE DISTANCE

The feedback loop is active during the c.c. $\mathrm{d}I/\mathrm{d}V$ measurement to keep the current constant and prevent a high current from saturating the lock-in amplifier. The feedback loop keeps the current constant by adjusting the distance from the tip to the sample as the bias voltage change. In our work, to fully observe multiple FER, wide bias voltage windows were used, from 2 V to 9 V. This important difference in voltage combined with the FER creates a considerable current variation during the bias voltage sweep. The use of c.c. $\mathrm{d}I/\mathrm{d}V$ simplify the experimentation but complexify the modelling and analysis of the data.

Figure 6.10 shows the height measured during c.c. $\mathrm{d}I/\mathrm{d}V$ experiment on the chlorine layer and in the middle some patches. At low bias voltage (<3.5 V), except for the single

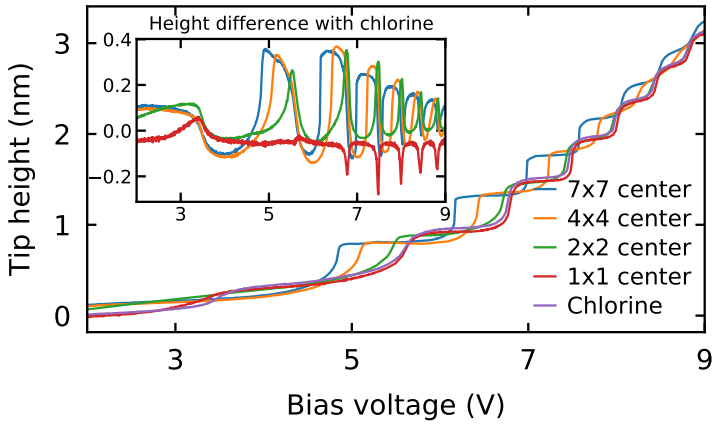


**Figure 6.10: Height variation during c.c. $\mathrm{d}I/\mathrm{d}V$ measurements.** . The c.c. $\mathrm{d}I/\mathrm{d}V$ were taken on the continuous chlorine layer (purple) and in the center of patches (red, green, orange and blue). All c.c. $\mathrm{d}I/\mathrm{d}V$ are regulated at 100pA. The $z = 0$ is the height regulated at 2V and 100pA on chlorine. All data were taken with the same tip, and the vertical drift was corrected between measurements by regulating the chlorine. Inset: The difference in height with the c.c. $\mathrm{d}I/\mathrm{d}V$ on chlorine.



vacancy, the patches have an apparent height higher than the chlorine, even if the chlorine layer is physically higher than the copper substrate. The insulating nature of the chlorine layer limits the conductance and creates this difference in apparent height. At bias voltage higher than 3.5 V, after the first IPS on the chlorine, the patches seem lower than the chlorine, and the height difference is in the order of the physical height of the chlorine layer. We can consider that the tip-sample distance between 3.5 V and 4.5 V, and after each FER, is approximately the same on the chlorine and inside the patches. This led us to conclude that the difference in the tip-sample distance between the chlorine layer and the copper patches does not play a major role in the difference in IPS energies and that this difference is due to the difference in work function between the two surfaces.

Another piece of information that we can extract from Figure 6.10 is that after each of the main FER ($m = 1$) the variation in tip-sample distance is minimal. The surge in current due to the FER force the tip to retract considerably from the surface, and the tunnelling current contribution to the total current is reduced to practically zero. At this distance, the tip is not in tunnelling range, so the current dependence is not exponential. The tip stays mostly at the same distance for all the sub-resonances and their energy mostly not affected by a change in the tip-sample distance. However, the potential will still be affected by the change in the bias voltage.

One impact that a change in the tip-sample distance will have on the modelling is the validity of the flat tip approximation. The electric potential between the tip and the sample can be approximated as two flat and parallel plates at a short distance. This allows a simple formula (Equation 3.46) for the electric potential depending uniquely on the dis-

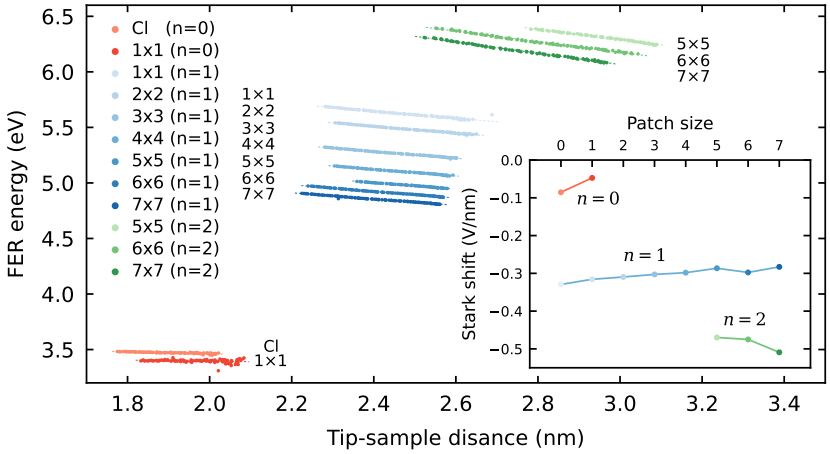


**Figure 6.11: Peak position variations due to a change in the tip sample distance.** . The plots combine multiple c.c. $\mathrm{d}I/\mathrm{d}V$ measurements on the patches done at different regulating setpoints and show the relationship between the peak energy position and the distance between the tip and sample. The zero of the tip-sample distance is set on the chlorine layer at 100 pA and 2 V. All data were taken with the same tip, and the vertical drift was corrected between measurements by regulating the chlorine. Inset: The variation (slope) for each series of values extracted by doing a linear fit. $n = 0$ is used to identify the first resonance on CuCl/Cu(100) for the first one on Cu(100).



tance between the tip and the sample and the applied bias voltage. At a larger distance, the roundness of the tip will have a non-negligible impact on the electric field value below the tip. This brings complexity to the modelisation, notably by adding a degree of freedom in the calculation. The round-tip can be modelled using Equation 3.47.

The enhanced energy resolution of our spectra allows us to accurately measure the Stark shift: the rate by which the FER energies shift as a function of the electric field. Here, the tip-sample distance has a considerable effect on the electric field at the sample surface. The relation between the magnitude of the electric field and the tip-sample distance is linear if the tip and sample can be approximated as two close plates. This approximation is justified for the tip-sample distances at which the first FER is observed[2, 4, 47]. In Figure 6.11, we show the shift in the FER energies as a function of the tip-sample distance, and from this extract the Stark shift for the primary FERs. We observe that the Stark shift is minimal for the first resonance but measurable. The Stark shift increases as the energy of the FER increases, and amounts to 500 mV/nm for the third resonance. This trend can be explained by considering that the lower resonances are located lower in the potential well, where, as depicted in Figure 2.5, the width of the well is less sensitive to changes in the electric field (i.e. the slope of the slanted part of the potential).

## 6.4. FOLLOW-UP RESEARCH

After completing the work presented above, the role of the main investigator was passed to Rasa Rejali. The research was pushed further and led to a publication with Rejali as the first author[48].

In the follow-up research, we made some significant developments that shine new light on the work presented here that are worth mentioning.

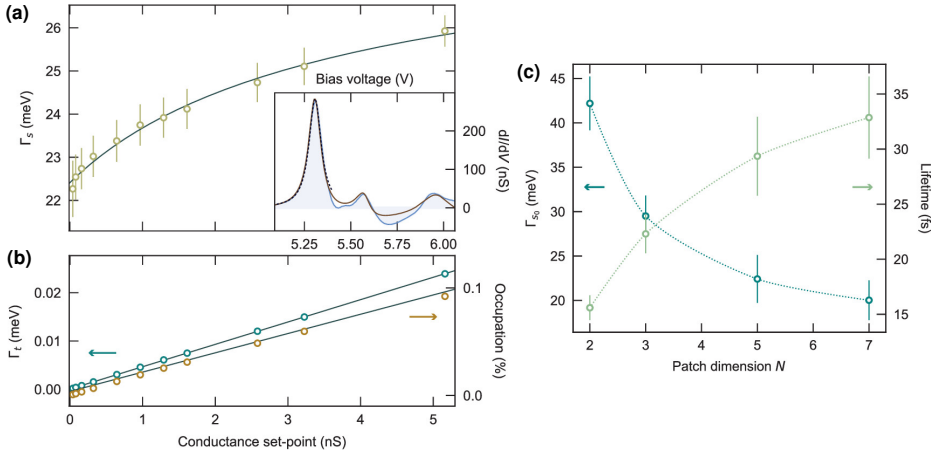


**Figure 6.12: Selected figures from Rejali *et al*[48].** (a) Figure 2(b) from Rejali*et al.* Sample decay rate for the first principal resonance as a function of the conductance. (b) Figure 2(c) from Rejali*et al.* Sample decay rate for the first principal resonance as a function of the conductance evaluated at the energy peak and average occupation of the state. (c) Figure 3(c) from Rejali*et al.* Estimated sample decay rate (blue circles) and lifetime (green circles) at zero setpoint conductance for each patch size.

One information that we wished to obtain was the lifetime of the electron state, but as rightfully mentioned in Rejali *et al.*: "Approximating the lifetime by the linewidth of the resonance is not valid here, as the potential in the out-of-plane direction changes as we carry out spectroscopy, leading to a changing resonance energy as a function of the applied voltage that artificially broadens the peak." This potential change comes from the receding tip and the change in bias voltage during spectroscopy. In Rejali *et al.*, the FER process is modelled using a double barrier potential transport model. Two important parameters of this model are the tip and sample decay rates ($\Gamma_t$ and $\Gamma_s$). The model can reproduce the observed resonance with good accuracy(see inset of Figure 6.12(a)) and allows the estimation of the $\Gamma_t$ and $\Gamma_s$ values (see Figure 6.12(a)-(b)). Those decay rates can be used to estimate the lifetime of the resonances (see Figure 6.12(c)). The results show an increased lifetime that can reach four times the lifetime of the unconstrained FER.

Another point that was explored is the spatial extent of the states. The current work observed that the confined states extend spatially outside of their confining potential.

This effect is now attributed to the changing potential as the tip recedes from the surface. The c.c. $\mathrm{d}I/\mathrm{d}V$ maps can be normalised to remove these artefacts of the experimental method. After normalisation, the states are almost entirely confined by their patches. The normalisation method is quite complex and mathematically involving and was worth is own publication. For more information and how to normalise the observed c.c. $\mathrm{d}I/\mathrm{d}V$ maps, the reader can consult Rejali *et al*[49].

## 6.5. CONCLUSION

The CuCl/Cu(100) surface offers a great platform to manipulate the atoms and vacancies to engineer the electric landscape of the surface. We have shown that the electric landscape can be used to create in-plane confinement of field-emitted electrons in localised states. We engineered those states by grouping together multiple vacancies to form square patches. The field-emitted electrons get trapped in-plane in these squares and out-of-plane by the tip-sample potential. The electrons trapped in the patches exhibit particle-in-a-box like behaviour.

The states inside the patches show quantisation and spatial dependencies. The energies of the resonances and the spatial distribution of these states were successfully modelled using square potentials of finite height. The numerical calculation uses a custom implementation of the variational principle approach, which allows solving the arbitrary potential's time-independent Schrödinger equation.

We demonstrated that the resonances' energy depends on the distance between the tip and the sample. The measurable Stark shift confirmed their nature as image potential states. This includes a resonance observed only on the continuous layer of chlorine and in the single vacancy around 3.5V previously attributed to the onset of the conduction band. The Stark-shift of this state and his total disappearance on larger patches bring us to the conclusion that it is an IPS.

### NOTE ON THE DATA ANALYSIS

The results from this chapter were obtained by processing a large quantity of data. Some of the methods used to process that data are presented here. They are not needed to understand the previous results but are worth mentioning.

#### 6.5.1. CORRECTION OF THE LINES DATA

The raw data acquired on the patches by making multiple c.c. $\mathrm{d}I/\mathrm{d}V$ along lines crossing the patches showed a peculiar feature: as the current increase, the patches limits seem to drift to the right (positive values). This drift happens on all the patches and seems similar for all the patches. We can see an example of this drift in the raw data plotted in the Figure 6.13, illustrating the correction procedure.

The deviation at high voltage is not due to piezo drift. As a precaution against the

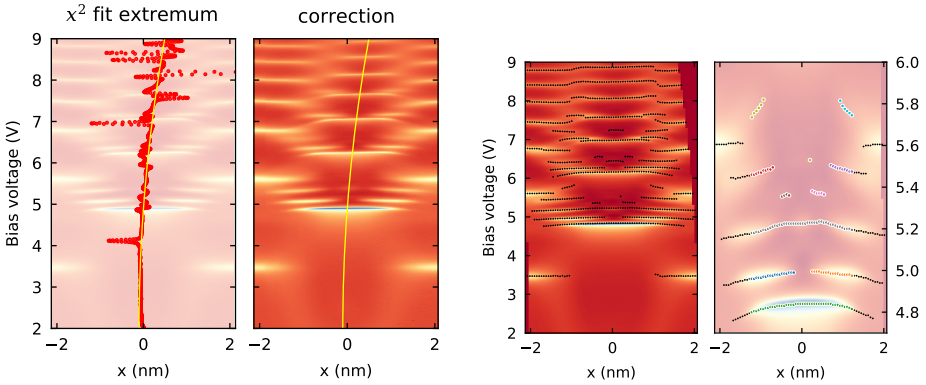


**Figure 6.13:** Correction of the horizontal shift at high bias voltage of the lines data. On the left: the maximum of a $x^2$ fit of each horizontal line (constant bias), and the resulting correction estimation ($y^2$ fit). On the right: the resulting correction of the actual data for the 7x7 and 6x6 patched. The dots correspond to the detected resonances peaks.

drift build-up during the long data acquisition period, we regularly corrected the position of the tip. Every five c.c. $\mathrm{d}I/\mathrm{d}V$, we tracked the position of a nearby vacancy and afterwards, moved the tip to the next five c.c. $\mathrm{d}I/\mathrm{d}V$ positions relative to the position of that vacancy. Consequently, if the cause of the drift in the c.c. $\mathrm{d}I/\mathrm{d}V$ at high bias voltage was the piezo drift, we should see it affect the whole range of bias voltage with a periodicity of five. We see a constant effect depending only on the bias voltage.

In consequence, we attribute the drift to the geometry of the tip. At high bias voltage, the tip is more distant from the surface, and a wider proportion of the tip apex is active in detecting the IPS. Consequently, the asymmetry in the tip geometry can have an enhanced impact on the measured c.c. $\mathrm{d}I/\mathrm{d}V$. The geometry of the tip was also a factor that needed consideration in other studies of IPS with STM[18, 26].

To remove the drift in the data, we assumed that for the same bias voltage (along a horizontal line) the c.c. $\mathrm{d}I/\mathrm{d}V$ should be symmetric and centred on the middle of the patch. We applied a polynomial fit of the second order on each line and used the extremum as the middle point. We applied a Gaussian filter on those extremum points to get smoother lines and remove some of the high variations. The red dots in Figure 6.13 are the resulting position of the extrema. We again applied a polynomial fit of the second-order but on the extrema to get the final correction, shown as the yellow line in Figure 6.13. The effect of the correction is visible as the continuous red parts in the top right of the plots in Figure 6.7.

### PEAK DETECTION

To find the position of the excitations inside the patches, we used a peak detection algorithm on each c.c. $\mathrm{d}I/\mathrm{d}V$ (vertical line). The algorithm allows us to identify the features, evaluate their spatial distribution and energy and estimate the associate incertitudes.

In Figure 6.13 is shown an example of the results of the algorithm for the 7x7 and 6x6 patched.

To prevent the noise from creating false detections, we smoothed the data before the peak detection algorithm by applying a Gaussian filter. We independently applied the peak detection algorithm on each c.c. $\mathrm{d}I/\mathrm{d}V$ using a threshold of 0.1 nS of prominence to identify the peaks. Afterwards, we applied a hierarchical clustering algorithm to group the detected peaks in space and energy. The final step was done manually by comparing the cluster with theoretical calculation and associating the clusters to the calculated states. We evaluated the energy incertitude by taking the maximum value between the difference separating the minimum and maximum peak energy in a cluster or 0.02 V.

## REFERENCES

[1] G. Binnig, K. H. Frank, H. Fuchs, N. Garcia, B. Reihl, H. Rohrer, F. Salvan, and A. R. Williams, *Tunneling Spectroscopy and Inverse Photoemission: Image and Field States,* Phys. Rev. Lett. **55**, 991 (1985).

[2] J. M. Pitarke, F. Flores, and P. M. Echenique, *Tunneling spectroscopy: Surface geometry and interface potential effects,* Surface Science **234**, 1 (1990).

[3] L. Limot, T. Maroutian, P. Johansson, and R. Berndt, *Surface-State Stark Shift in a Scanning Tunneling Microscope,* Phys. Rev. Lett. **91**, 196801 (2003).

[4] D. B. Dougherty, P. Maksymovych, J. Lee, M. Feng, H. Petek, and J. T. Yates, *Tunneling spectroscopy of Stark-shifted image potential states on Cu and Au surfaces,* Phys. Rev. B **76**, 125428 (2007).

[5] J. Girovsky, J. Lado, S. Otte, F. Kalff, E. Fahrenfort, L. Peters, and J. Fernández-Rossier, *Emergence of quasiparticle Bloch states in artificial crystals crafted atom-by-atom,* SciPost Physics **2**, 020 (2017).

[6] R. Drost, T. Ojanen, A. Harju, and P. Liljeroth, *Topological states in engineered atomic lattices,* Nature Phys **13**, 668 (2017).

[7] D. Straub and F. J. Himpsel, *Identification of Image-Potential Surface States on Metals,* Phys. Rev. Lett. **52**, 1922 (1984).

[8] P. D. Johnson and N. V. Smith, *Image-potential states and energy-loss satellites in inverse photoemission spectra,* Phys. Rev. B **27**, 2527 (1983).

[9] V. Dose, W. Altmann, A. Goldmann, U. Kolac, and J. Rogozik, *Image-Potential States Observed by Inverse Photoemission,* Phys. Rev. Lett. **52**, 1919 (1984).

[10] N. V. Smith, *Phase analysis of image states and surface states associated with nearly-free-electron band gaps,* Phys. Rev. B **32**, 3549 (1985).

[11] J. M. Pitarke, P. M. Echenique, and F. Flores, *Apparent barrier height for tunneling electrons in STM,* Surface Science **217**, 267 (1989).

[12] J. G. Simmons, *Potential Barriers and Emission-Limited Current Flow Between Closely Spaced Parallel Metal Electrodes,* Journal of Applied Physics **35**, 2472 (1964).

[13] U. Höfer, I. L. Shumay, C. Reuß, U. Thomann, W. Wallauer, and T. Fauster, *Time-Resolved Coherent Photoelectron Spectroscopy of Quantized Electronic States on Metal Surfaces,* Science **277**, 1480 (1997).

[14] R. Young, J. Ward, and F. Scire, *The Topografiner: An Instrument for Measuring Surface Microtopography,* Review of Scientific Instruments **43**, 999 (1972).

[15] K. Bobrov, A. J. Mayne, and G. Dujardin, *Atomic-scale imaging of insulating diamond through resonant electron injection,* Nature **413**, 616 (2001).

[16] T. Jung, Y. W. Mo, and F. J. Himpsel, *Identification of Metals in Scanning Tunneling Microscopy via Image States,* Phys. Rev. Lett. **74**, 1641 (1995).

[17] S. Baumann, I. G. Rau, S. Loth, C. P. Lutz, and A. J. Heinrich, *Measuring the Three-Dimensional Structure of Ultrathin Insulating Films at the Atomic Scale,* ACS Nano **8**, 1739 (2014).

[18] H.-C. Ploigt, C. Brun, M. Pivetta, F. Patthey, and W.-D. Schneider, *Local work function changes determined by field emission resonances: NaCl/Ag(100),* Phys. Rev. B **76**, 195404 (2007).

[19] B. Borca, S. Barja, M. Garnica, D. Sánchez-Portal, V. M. Silkin, E. V. Chulkov, C. F. Hermanns, J. J. Hinarejos, A. L. Vázquez de Parga, A. Arnau, P. M. Echenique, and R. Miranda, *Potential Energy Landscape for Hot Electrons in Periodically Nanostructured Graphene,* Phys. Rev. Lett. **105**, 036804 (2010).

[20] B. Borca, C. Castenmiller, M. Tsvetanova, K. Sotthewes, A. N. Rudenko, and H. J. W. Zandvliet, *Image potential states of germanene,* 2D Mater. **7**, 035021 (2020).

[21] K. Giesen, F. Hage, F. J. Himpsel, H. J. Riess, W. Steinmann, and N. V. Smith, *Effective mass of image-potential states,* Phys. Rev. B **35**, 975 (1987).

[22] P. M. Echenique and M. E. Uranga, *Image potential states at surfaces,* Surface Science **247**, 125 (1991).

[23] P. Wahl, M. A. Schneider, L. Diekhöner, R. Vogelgesang, and K. Kern, *Quantum Coherence of Image-Potential States,* Phys. Rev. Lett. **91**, 106802 (2003).

[24] L. Bürgi, O. Jeandupeux, H. Brune, and K. Kern, *Probing Hot-Electron Dynamics at Surfaces with a Cold Scanning Tunneling Microscope,* Phys. Rev. Lett. **82**, 4516 (1999).

[25] J.-F. Ge, H. Zhang, Y. He, Z. Zhu, Y. C. Yam, P. Chen, and J. E. Hoffman, *Probing image potential states on the surface of the topological semimetal antimony,* Phys. Rev. B **101**, 035152 (2020).

[26] P. Ruffieux, K. Aït-Mansour, A. Bendounan, R. Fasel, L. Patthey, P. Gröning, and O. Gröning, *Mapping the Electronic Surface Potential of Nanostructured Surfaces,* Phys. Rev. Lett. **102**, 086807 (2009).

[27] J. Li, W.-D. Schneider, R. Berndt, and S. Crampin, *Electron Confinement to Nanoscale Ag Islands on Ag(111): A Quantitative Study,* Phys. Rev. Lett. **80**, 3332 (1998).

[28] K. Schouteden and C. Van Haesendonck, *Quantum Confinement of Hot Image-Potential State Electrons,* Phys. Rev. Lett. **103**, 266805 (2009).

[29] K. Schouteden and C. Van Haesendonck, *Particle-in-a-box confinement of electron gases in and above the surface of self-organized Co nanowires at Au(111) step edges,* Appl. Phys. A **107**, 183 (2012).

[30] H. G. Zhang, H. Hu, Y. Pan, J. H. Mao, M. Gao, H. M. Guo, S. X. Du, T. Greber, and H.-J. Gao, *Graphene based quantum dots,* J. Phys.: Condens. Matter **22**, 302001 (2010).

[31] S. Stepanow, A. Mugarza, G. Ceballos, P. Gambardella, I. Aldazabal, A. G. Borisov, and A. Arnau, *Localization, splitting, and mixing of field emission resonances induced by alkali metal clusters on Cu(100),* Phys. Rev. B **83**, 115101 (2011).

[32] J. I. Pascual, C. Corriol, G. Ceballos, I. Aldazabal, H.-P. Rust, K. Horn, J. M. Pitarke, P. M. Echenique, and A. Arnau, *Role of the electric field in surface electron dynamics above the vacuum level,* Phys. Rev. B **75**, 165326 (2007).

[33] D. M. Eigler and E. K. Schweizer, *Positioning single atoms with a scanning tunnelling microscope,* Nature **344**, 524 (1990).

[34] K. K. Gomes, W. Mar, W. Ko, F. Guinea, and H. C. Manoharan, *Designer Dirac fermions and topological phases in molecular graphene,* Nature **483**, 306 (2012).

[35] M. R. Slot, T. S. Gardenier, P. H. Jacobse, G. C. P. Miert, S. N. Kempkes, S. J. M. Zevenhuizen, C. M. Smith, D. Vanmaekelbergh, and I. Swart, *Experimental realization and characterization of an electronic Lieb lattice,* Nature Physics **13**, 672 (2017).

[36] A. A. Khajetoorians, D. Wegner, A. F. Otte, and I. Swart, *Creating designer quantum states of matter atom-by-atom,* Nature Reviews Physics **1**, 703 (2019).

[37] N. V. Smith, C. T. Chen, and M. Weinert, *Distance of the image plane from metal surfaces,* Phys. Rev. B **40**, 7565 (1989).

[38] s. Westphal and A. Goldmann, *Chlorine adsorption on copper: II. Photoemission from Cu(001)c(2x2)-C1 and Cu(111)($\sqrt{3}\times\sqrt{3}$)R30$\̂circ$-Cl,* Surface Science **131**, 113 (1983).

[39] V. Dose, *Image potential surface states,* Phys. Scr. **36**, 669 (1987).

[40] M. Ortuo and P. M. Echenique, *Phase shifts, image planes, and surface states at metal surfaces,* Phys. Rev. B **34**, 5199 (1986).

[41] T. Vo-Dinh and P. Halevi, *Photonic probes of surfaces,* Elsevier, Amsterdam **1**, 67 (1995).

[42] A. G. Borisov, T. Hakala, M. J. Puska, V. M. Silkin, N. Zabala, E. V. Chulkov, and P. M. Echenique, *Image potential states of supported metallic nanoislands,* Phys. Rev. B **76**, 121402 (2007).

[43] F. E. Kalff, M. P. Rebergen, E. Fahrenfort, J. Girovsky, R. Toskovic, J. L. Lado, J. Fernández-Rossier, and A. F. Otte, *A kilobyte rewritable atomic memory,* Nat Nano **11**, 926 (2016).

[44] M. N. Huda, S. Kezilebieke, T. Ojanen, R. Drost, and P. Liljeroth, *Tuneable topological domain wall states in engineered atomic chains,* npj Quantum Mater. **5**, 1 (2020).

[45] G. A. Burdick, *Energy Band Structure of Copper,* Phys. Rev. **129**, 138 (1963).

[46] M. N. Huda, S. Kezilebieke, and P. Liljeroth, *Designer flat bands in quasi-one-dimensional atomic lattices,* Phys. Rev. Research **2**, 043426 (2020).

[47] J. M. Blanco, F. Flores, and R. Pérez, *STM-theory: Image potential, chemistry and surface relaxation,* Progress in Surface Science **81**, 403 (2006).

[48] R. Rejali, L. Farinacci, D. Coffey, R. Broekhoven, J. Gobeil, Y. M. Blanter, and S. Otte, *Confined Vacuum Resonances as Artificial Atoms with Tunable Lifetime,* ACS Nano **16**, 11251 (2022).

[49] R. Rejali, L. Farinacci, and S. Otte, *Normalization procedure for obtaining the local density of states from high-bias scanning tunneling spectroscopy,* Phys. Rev. B **107**, 035406 (2023).

# 7

# CONCLUSION AND OUTLOOK

This thesis mainly focuses on exploring how the presence of the tip in STM experiments can be harnessed to bring new insights into the observed phenomena or new experimental methods. This tip functionalisation is accomplished via three different axes: the manipulation of the atom via interaction with the tip, the use of the tip to locally bias the magnetic field, and the change of the vertical confining potential of field-emission potential.

The first use of the tip is, nowadays, quite common. Atom manipulation is often used in STM experiments to create specific structures and configurations to study. In this thesis, two different atom manipulation techniques were used – the vertical manipulation allowed the creation of frustrated spin loops on $Cu_2N$ islands growth on $Cu_3Au(100)$ substrate, and horizontal manipulation was used to create multiple confining potentials for field-emission resonances with a sub-saturated monolayer of chlorine on Cu(100). The assembling of the spin loop was made possible, or at least easier, by the novel sample preparation presented in this thesis. The $Cu_2N$ islands' growth on $Cu_3Au(100)$ opens the door to the creation of large structures of coupled spin by not only increasing the absolute space available but also this increased space makes the whole process easier. In the future, the size of the islands could become larger as no limitation was observed experimentally.

The second functional use of the tip is as a tool to change the conditions of the experimental setup. After building the magnetically frustrated spin loop, the tip was used to change the effective magnetic field locally near specific spin. This brings experimental information that would not be available by changing the global magnetic field. By using the magnetised tip near the atoms, it was possible to change the distribution of the states in the whole loop and adjust the frequency and balance of the states switching. This revealed the sensitivity of the state-switching process due to the magnetic frustration in the loop. The experiment also shows that the effect only depends on the distance between the tip and the sample and that the whole loop switches states together.

When examining the particle-in-a-box states produced by chlorine-enveloped copper patches, utilising the tip as an experimental tool proved crucial. To accurately model the potential confining the vertical field-emission resonance, it's necessary to take into account the second surface - the tip. The shape of the potential is affected by changes in the distance between the sample and the tip, which in turn directly affects the observed energies of the field-emission resonances.

In this thesis, the functionalization of the tip played a crucial role in the presented experiments. By taking its presence into account, new insights into the experimental phenomena were gained.

# CURRICULUM VITÆ

## Jeremie GOBEIL

07-08-1983 Born in Chicoutimi, Canada.

## EDUCATION

2007 – 2011 B.Sc. Physics
Université du Québec à Trois-Rivières, Canada

2007 – 2011 B.Sc. Computer Science
Université du Québec à Trois-Rivières, Canada

2011 – 2015 M.Sc. Computational Physics
Université du Québec à Trois-Rivières, Canada
*Thesis:* Numerical Calculation of the Diffusion Coefficient of Hydrogen in Palladium-Copper Alloys Using Ab Initio Calculations and Dynamics Monte Carlo Simulations.
*Supervisor:* Prof. dr. Pierre Bénard

2023 Ph.D. Physics
Delft University of Technology
*Thesis:* Functional tip-sample interaction in STM
*Promotors:* Prof. dr. A.F. Otte and Prof. dr. ir. H.S.J. van der Zant

# LIST OF PUBLICATIONS

6. Rejali R., Farinacci L., Coffey D., Broekhoven R., **Gobeil J.**, Blanter Y.M., Otte A.F. *Confined Vacuum Resonances as Artificial Atoms with Tunable Lifetime.* ACS Nano. 2022 Jul 26;16(7):11251–8.

5. Veldman L.M., Farinacci L., Rejali R., Broekhoven R., **Gobeil J.**, Coffey D., Ternes M., Otte A.F. et al. *Free coherent evolution of a coupled atomic spin system initialized by electron scattering.* Science. 2021 May 28;372(6545):964–8.

4. Rejali R., Coffey D., **Gobeil J.**, González J.W., Delgado F., Otte A.F. *Complete reversal of the atomic unquenched orbital moment by a single electron.* npj Quantum Materials. 2020 Aug 27;5(1):1–7.

3. Elbertse R.J.G., Coffey D., **Gobeil J.**, Otte AF. *Remote detection and recording of atomic-scale spin dynamics.* Communications Physics. 2020 May 25;3(1):1–5.

2. **Gobeil J.**, Coffey D., Wang S.J., Otte A.F. *Large insulating nitride islands on Cu3Au as a template for atomic spin structures.* Surface Science. 2019 Jan 1;679:202–6.

1. **Gobeil J.** *Étude de la diffusion de l'hydrogène dans des alliages Pd1-xCux par des méthodes Monte-Carlo et des simulations ab initio.* UQTR; 2016. Available from: http://depot-e.uqtr.ca/id/eprint/7843/